



POLITECNICO
MILANO 1863

SCUOLA DI INGEGNERIA INDUSTRIALE
E DELL'INFORMAZIONE

Coupling intra-cellular and multi-cellular dynamics in spatially-extended models of root-hair initiation

TESI DI LAUREA MAGISTRALE IN
MATHEMATICAL ENGINEERING - INGEGNERIA MATEMATICA

Author: **Teresa Babini**

Student ID: 945590

Advisor: Prof. Simona Perotto

Co-advisors: Prof. Daniele Avitabile, Dr. Nicola Ferro

Academic Year: 2020-21

Abstract

This thesis deals with novel models and numerical approximations of spatially-extended multi-cellular models of Rho Of Plants (ROPs), that is, a family of proteins responsible for root-hair initiation in the plant cell *Arabidopsis thaliana*. The study of this dynamical system is of great relevance in the so-called agriculture 4.0, since it is instrumental to optimise plant uptake. In particular, ascertaining how intra-cellular protein distributions and extra-cellular coupling influence root-hair initiation is a challenging but pressing problem.

Current studies have focussed on two separate model types: on the one hand, ROPs dynamics is studied in single-cell models, which resolve patterns at sub cellular level; on the other, multi-cellular models with realistic geometries neglect intra-cellular patterning. In this thesis we make progress on coupling these two model descriptions.

We initially focus on a well-established single-cell, nonlinear reaction-diffusion model, here approximated for the first time with a finite-element scheme. In addition, we present a new model which couples multiple cells through ROP flux at the interface. We present numerical evidence that such coupling has a bearing on the patterns supported by the model. It is shown that, under variations of auxin gradients, the model robustly forms ROP hotspots from ROP stripes, and that spots are later advected downstream.

Finally, we consider a novel model in which the auxin dynamics are not prescribed, but derive from the interaction between this hormone and other membranous proteins (PIN). We show that self-sustained auxin oscillations influence ROP intracellular patterning.

Keywords: root-hair initiation, nonlinear reaction-diffusion problem, multi-cellular model, auxin-PIN, Robin-Robin, Finite Element method

Abstract in lingua italiana

Questa tesi tratta di nuovi modelli e approssimazioni numeriche per modelli multi-cellulari estesi in spazio, riguardanti le proteine delle piante Rho (ROPs), una famiglia di proteine responsabili per l'avvio dei peli radicali root-hairs nella cellula vegetale *Arabidopsis thaliana*. Lo studio del relativo sistema dinamico è di grande importanza in quella che viene chiamata agricoltura 4.0, poichè diventa determinante ottimizzare l'assorbimento dei nutrienti da parte delle piante. In particolare, sfidante è verificare come la distribuzione intra-cellulare delle proteine e l'accoppiamento extra-cellulare influenzano l'avvio dei root-hairs.

Gli studi attuali si sono focalizzati su due modelli separati: da una parte, la dinamica ROPs è stata studiata con modelli mono-cellulari, che risolvono i pattern a livello subcellulare; dall'altro lato, modelli multi-cellulari con geometrie realistiche escludono l'andamento intra-cellulare. In questa tesi si è avanzato un modello, accoppiando queste due descrizioni modellistiche.

Inizialmente ci focalizziamo su un modello ben definito mono-cellulare, di reazione-diffusione non lineare, approssimandolo qui per la prima volta tramite uno schema agli elementi finiti. In aggiunta, presentiamo un nuovo modello che accoppia più cellule tramite flussi di ROPs all'interfaccia. Presentiamo evidenze numeriche che questo accoppiamento ha rilevanza nel determinare i pattern sostenuti dal modello. Per variazioni del gradiente auxina, il modello forma stabilmente zone circolari ad alta concentrazione di ROP attive da strisce e questi spot sono poi trasportati a valle.

Infine, si è considerato un nuovo modello in cui la dinamica dell'auxina non è prescritta, bensì derivata dall'interazione tra questo ormone e la sua proteina di trasporto di membrana (PIN). Abbiamo mostrato che oscillazioni autosostenute di auxina influenzano il patterning delle proteine ROP.

Parole chiave: proteine ROP, auxina-PIN, problema nonlineare di reazione-diffusione, Robin-Robin, modello multi-cellulare, elementi finiti

Contents

Abstract	i
Abstract in lingua italiana	ii
Contents	iii
1 Introduction	1
1.1 Biological background	1
1.1.1 Root hairs initiation	2
1.1.2 Pattern formation	3
1.2 A ROPs physical model	4
1.2.1 The ROPs Reaction-Diffusion model system	4
1.3 Auxin	6
1.3.1 Auxin transport model	7
1.4 Mathematical background	8
1.5 New model motivations	9
1.6 Thesis outline	9
2 Spot formation in a singular cell	11
2.1 Physical model	11
2.2 Numerical treatment	15
2.2.1 Stationary system	15
2.2.2 Time-dependent scheme	20
2.3 Numerical results	23
2.3.1 Validation of steady state under homogeneous regime	24
2.3.2 Validation of semi-implicit method with a steady state under not homogeneous regime	26
2.3.3 Single cell solver convergence analysis	28
2.3.4 Simulation of a single cells system	30

3 Pattern formation in a pluricellular system	33
3.1 Physical model	33
3.2 Numerical treatment	35
3.2.1 The domain decomposition method	37
3.2.2 Classic Robin-Robin algorithm	38
3.2.3 A new iterative modeling algorithm	42
3.3 Numerical assessment	47
3.3.1 Stagnant cells reference solution	47
3.3.2 Tuning channels parameters	48
3.3.3 Parallelizable versus not-parallelizable mode	55
3.3.4 Overall auxin level k20	56
3.3.5 Time-dependent auxin distribution	61
3.3.6 Four cell system	66
4 Auxin-PIN dynamic system contribution to pattern formation	76
4.1 Physical model	76
4.2 Numerical discretization	79
4.3 Numerical Results	82
4.3.1 ROPs system in a strand of two cells	83
4.3.2 Coupled ROPs model with auxin-PIN dynamics	84
5 Codes instructions	99
5.1 Running codes instructions - 1cell system	99
5.2 Running codes instructions - 2 and 4 cells systems	101
6 Conclusions and future developments	103
Bibliography	105
List of Figures	110
List of Tables	113
Acknowledgements	114

1 | Introduction

This thesis develops a model and some numerical methods for biological systems. The specific target of the study is a system describing initiation of hair-like protrusions in the epidermal cells of the roots of the model plant *Arabidopsis thaliana*, studied at sub-cellular level. *Arabidopsis* is a model genetic organism topic of an internationally coordinated project, providing large collections of mutants available for analysis [19]. The study of root-hairs (RH) is agriculturally important for understanding nutrient anchorage and uptake of plants, in order optimize absorption.

In the following chapter we provide a description of the biological field of interests for this thesis. Firstly we address the attention to the root-hair initiation process and to the proteins involved in location of sources for this protuberance. Hair formation is related to the activation and deactivation of some proteins involved. We summarize the mechanism of activation and deactivation through a Reaction-Diffusion (RD) model, detailing all parameters and coefficients involved. In particular, we focus on hormone auxin role in this process and on its transport model through cells. We present previous analysis made over the RD system and motivate the objective of this thesis.

1.1. Biological background

We provide a brief overview on the biological background our model and studies are inserted in. During the development of multicellular organisms, it is of big interest and importance how boundaries are formed between neighboring groups of cells, divided according to their distinct functions, in order to control organ and body growth and functions [22]. At the organ level, three distinct morphological zones can be identified in the *Arabidopsis* primary root: the merismatic zone, where new cells are formed in the meristem, located close to the root tip; the elongation zone, where cells after a number of divisions move through and rapidly increase in size, mainly in length; and the mature zone, where cells stop growing and the RHs are produced [5, 10]. In Figure 1.1 a schematic representation of the described different morphological zones is given.

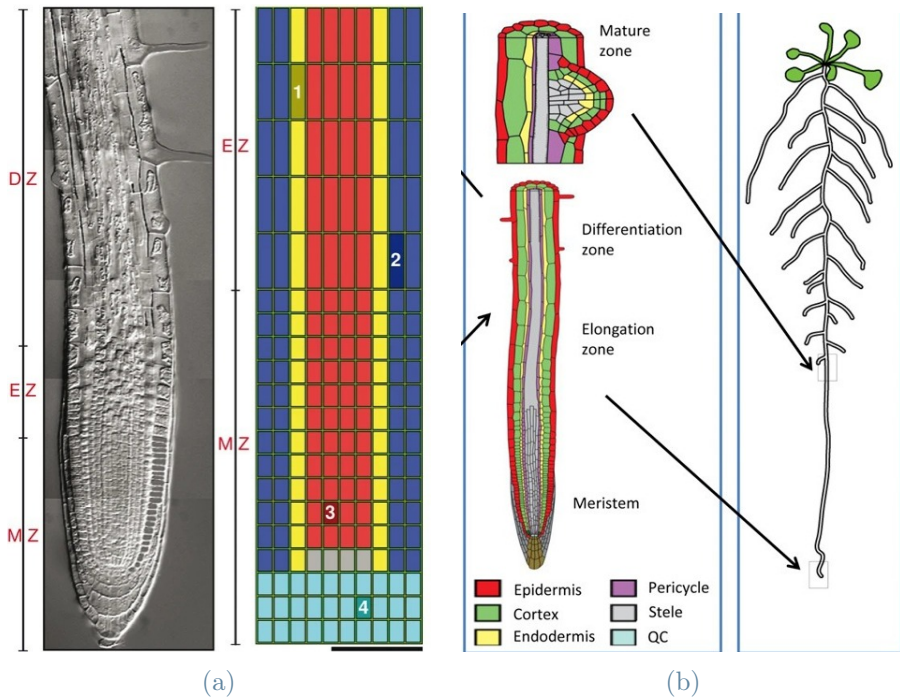


Figure 1.1: Synthetic rappresentation of the *Arabidopsis* root: differentiation zone (DZ); elongation zone (EZ); meristematic zone (MZ). Figure reproduced from [4, 18].

All the different steps of growth are initiated, influenced, activated or deactivated by different hormones, regulating both cell division in the root meristem and cell elongation in the elongation zone. In particular, hormones' distributions within plants tissues affect plants growth [22, 25]. For example, in regions where cells undergo a rapid expansion, such as the meristem or the elongation zone, hormone gradients can arise due to the interplay between dilution, diffusion, production, decay, and receptors binding [9]. Therefore, characterizing growth regulation is a key point in order to understand deeply the dynamics of particular kind of specialized proteins and hormones, together with their mutual regulation both within and between cells. Regarding this, type differentiation and position strongly suggest the presence of cell-to-cell communications, which are important for formation and separation of cells.

1.1.1. Root hairs initiation

Root hairs are protuberances that outgrow from root epidermal surfaces; example of mutants with multiple RH sites are shown in Figure 1.2, togetehr with a scetch of tissue organisation. In *Arabidopsis*, these protuberances can grow up to more than 1mm in length and approximately $10\text{--}20\mu\text{m}$ in diameter [19].

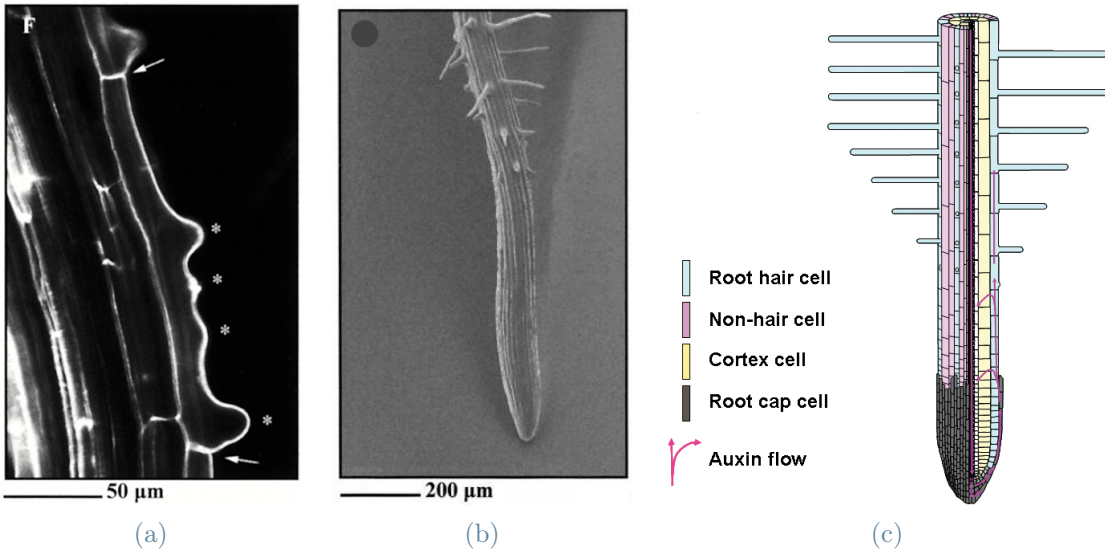


Figure 1.2: (1.2a) A mutant RH cell; asterisks show multiple sites of RH initiation in a single root hair cell. Figure reproduced from [41] - (1.2b) hair-forming cell with three RH initiation locations. Figure taken from [41] - (1.2c) schematic representation of a plant root with tissue organisation. Figure reproduced from [24].

A single hair is formed in each root hair cell, at a set distance equal to 20% the way along the cell from its basal end (i.e., the end closest to root tip) [40].

The precursor for a strong symmetry-breaking is the formation of a single localized patch of activated small guanine nucleotide-binding proteins (small G-proteins). These type of proteins are known collectively as Ras homologous (Rho) of plants, synthetically called ROPs [8, 14]. Their role is transmission of chemical signals in and out a cell, in order to effect a number of changes inside the cell [23]. ROPs represent indeed an example of the receptors, controlling a wide variety of cellular processes and contributing strongly to crucial cellular level tasks such as morphogenesis, movement, wound healing, division and, of particular interest here, cell polarity generation [34]. Working as molecular “connectors”, these proteins shift between active and inactive states, regulating both the initiations process of root-hairs and the direction of the tip growth.

1.1.2. Pattern formation

A big range of examples of pattern structures formation in open systems belongs to completely different fields of applications [30]. As a result, the factors regulating and influencing pattern formation have been observed on several physical scales and theoretically explained. Nonetheless, biology brings up a yet larger variety of interesting models

and morphogenesis processes that have been explained using pattern formation theory. In our specific system, we refer to spots or stripes, collectively called patches, a collection of structures where the active ROP is found at elevated concentration inside the cell. The formation of a patch of small G-proteins ROPs is the first visible sign that a root hair cell has initialized its formation process on the cell membrane [12]. Their spatial location and change in time is the main output of interest of our model [7, 25, 35].

Still not completely understood, the spatio-temporal dynamics of those spots and stripes can be recovered through RD models. From a biological context, cells appear to be influenced by long-range gradients that indicate morphogens where to be placed, where to concentrate the most and therefore where to locate patches [29]. In addition, the high concentration zones are pre-determined also by positional information coming from boundaries ([24]). All these considerations over factors influencing ROPs pattern formation have been studied at sub-cellular level and summarized in a partial differential model (2.1).

1.2. A ROPs physical model

We focus on the root-hair initiation stage mechanism. ROPs localization starts to produce a protuberance, which leads to the softening of the cell wall and therefore to hair formation. There are three main forms ROPs can be found: active, when it is bound to GTP regulator protein, inactive when it is bound to GDP regulator protein and free, when it does not appear in the growth path region. ROPs can switch between these states, cycling from the GTP-bound active form, attached to the cell membrane, to the GDP-bound therefore inactive form, which lie in the cytoplasm [23, 25].

The Figure 1.3 illustrates the biochemical process whereby active ROPs and free ROPs classes are able to become either inactive or get unbound, together with other processes necessary for the cell membrane softening and sequent RH formation [33].

1.2.1. The ROPs Reaction-Diffusion model system

The mathematical form chosen to model this biological process is a Reaction-Diffusion system of equations. Indeed, diffusion and reaction when acting together, show symmetry breaking of systems and are typically used for describing the process of interaction in which an active agent is inhibited by another one, diffusing more slowly [33]; A. Turing proposed an interaction between two chemical agents, having time and space dependent concentrations [47]. This kind of systems has been widely studied; in particular, Schnaken-

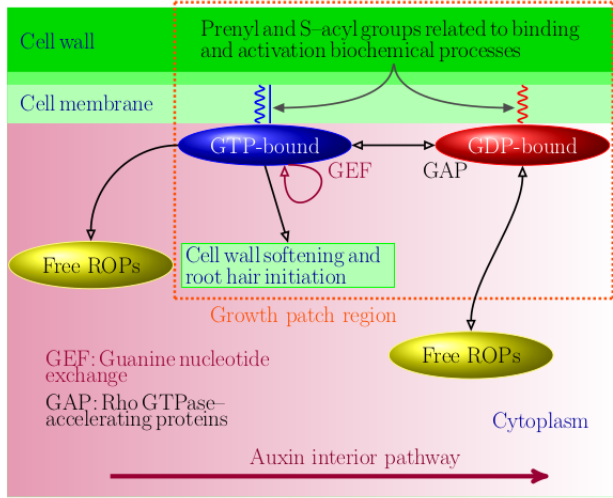


Figure 1.3: Scheme taken from [13] of the binding process and cycling between active- and inactive- state of ROPs

berg model [45], one of the most widely studied models undergoing Turing-like pattern formation schemes, can display features considered biologically relevant. The initiation process model, discussed in Section 1.1.1, was proposed by Payne & Grierson [35] in the form of a reaction-diffusion system for inactive (free) and active (membrane bound) ROPs [27].

Guanine nucleotide Exchange Factors (GEFs) and GTPase-Activating Proteins (GAPs) regulate the activity of ROPs to control cellular functions. GEFs turn on signaling by catalyzing the exchange from G-protein-bound GDP(inactive-state) to GTP (active-state), whereas GAPs terminate signaling by inducing GTP hydrolysis. Therefore the rate at which ROPs are activated and deactivated depends on GEF and GAPs proteins.

The rate of activation of inactive ROPs induced by GEF of each Rho species is modelled by a Hill function [23]:

$$k_{GEF} = k_1 + \frac{k_2 U^q}{1 + k_3 U^q} \quad (1.1)$$

where k_1 is the activation rate, k_2 represents autocatalytic acceleration, k_3 is a saturation coefficient and the power q is typically chosen equal to 2 to preserve the nonlinearity of the model. Payne & Grierson [35] took a simplified version of (1.1) by taking $k_3 = 0$ and allowing only one species of ROP to be modelled [23]. In plants, although there are several different kinds of ROPs, their activation is not thought to involve cross talk, therefore this simplification is justified. Inactive ROP is activated at rate k_{GEF} , therefore the activation step is assumed to be proportional to $k_{GEF}v = k_1v + k_2u^2v$.

Experimental evidence suggests a longitudinal spatially decaying gradient of auxin which Payne & Grierson postulate modulates the autocatalytic step. According to this assumption, we suppose that parameter k_2 is spatially dependent in the following way:

$$k_2 = k_{20}\alpha(x, y), \quad (1.2)$$

where k_{20} measures the overall auxin level within the cell and α is a smooth function that represents the spatial distribution of auxin, normalized, meaning that:

$$\alpha(0, y) = 1, \frac{\partial\alpha}{\partial x} < 0. \quad (1.3)$$

The RD model suppose that ROPs do not diffuse through the cell wall. We will deal with more complex boundary conditions in Chapter 3. The system modelled so far is for a ROP bounding on-and-off switching fluctuation. This process is assumed to take place on the cell membrane and RH cells are flanked by non-RH cells. As far as we know, no ROP exchanges have been reported, [19], thus homogeneous Neumann boundary conditions are assumed everywhere.

1.3. Auxin

The key feature of the previously described mechanism is that the activation step is postulated to be dependent on the concentration of the plant hormone auxin. Auxin is a plant hormone involved in a large number of physiological processes and its spatial distribution is critical for plant morphogenesis [18, 28, 32]; for example, it stimulates growth and regulates fruit setting, budding, side branching and the formation of flower parts [18, 42]. Root-hairs outgrowth is one of the processes stimulated by auxin. Measurements of auxin through sensors are impossible to obtain; still a difference between the location of auxin in- and out-pumps in RH cell and non-RH cells has been observed. Thus it is supposed in [24] that there is a decreasing gradient of auxin from the apical end of each RH cell, as stated in (1.3).

A simple transport process is assumed to govern the auxin flux through a RH cell, which postulates that auxin diffuses within cells with rate $D_\alpha = 10^2 \mu m^2/s$, much faster than ROPs. This implies that ROPs and auxin speeds belong to different time-scales [1]. In many studies of ROPs model auxin dynamics have been neglected, considering its spatial distribution to be at steady state and therefore time independent [2, 14, 29].

There are various proofs that this simplification can be considered qualitatively reason-

able. For example, in [13] it was shown that qualitative results are insensitive to different piecewise smooth non-increasing functional forms of α such as (1.3), for the same difference $\alpha(0) - \alpha(1)$. At the beginning of our simulations we have followed similar assumptions, considering auxin distribution at steady-state and only space dependent.

1.3.1. Auxin transport model

Actually, auxin distribution in tissues is complex and little is known about specific details of its flow within a cell. Various works underline the role of auxin gradient in developmental biology and how it is influenced by active transport between neighboring cells [6, 39]. There are different genes responsible for polar transport of auxin, known as carriers proteins: PIN-FORMED(PIN) in efflux, AUX/LAX in influx and MDR/PG in both [13]. One of the most studied are the integral membrane PIN transporters [1, 32]; their distribution along the cell membrane has a not fully-known mechanism, but it has been intensively observed that PINs location is correlated with local differences in auxin concentration [28]. Therefore in previous works and here, we focus the attention on PIN influence on auxin dynamics, neglecting the other possible influential proteins.

As peculiarity of auxin model it has also been observed a feedback of auxin in controlling its PIN carriers expression, both influx and efflux [32]. The reflected flow mechanism relies on the presence of positive and negative regulations between auxin and its carriers. In this way it provides for self-organization of the observed auxin distribution in the root and explains much of the positional information in root patterning [44].

Moreover, concerning the mutual influence between auxin and its carriers, there are two types of models describing the influence of auxin on PIN distribution on cell membrane:

- Concentration-based models: the rate of accumulation of PIN depends on the local differences of auxin concentration or on the relative level of auxin between neighboring cells [43].
- Flux-based models: the accumulation of PIN on cell membranes is function of the flux of auxin through these [46].

The model employed in [15] is of the second type and according to it auxin can enter the cells by free diffusion, whereas the intermediate active efflux PIN transporters distributed on cell membrane is necessary to leave the cells. Similarly as ROPs system, a patterns may emerge from a nonpatterned situation and certain parameters setting leads to unsteady not-homogeneous auxin distribution. Analysis and studies regarding this topic were developed in [15].

We have chosen as model for auxin-PIN dynamics the one developed in [15]. More details and parameters characterizing the model chosen for auxin dynamics are given in Chapter 4.

1.4. Mathematical background

Some studies regarding the dynamics and stability of ROPs localized structures have been carried on through Turing bifurcations analysis, asymptotic analysis and some full time simulations [26].

A lot of biological systems, similar to the one we focused on, have few insight on the precise parameters and factors characterizing the model and their precise quantification is not so easy achievable. The benefit of mathematical analysis such as Turing bifurcation analysis is helping to overcome the difficulties in analysing those systems, not being bound to a particular set of parameters. On the other hand, asymptotic analysis helps giving full parametrisation of only qualitative, experimentally observed features.

Regarding ROPS pattern formation previous studies, there have been different points of interest. Payne & Grierson, who derived the 1d mathematical model of ROPs kinetics, through simulations show that the active ROP variable tends to form patch-like states towards the apical end [35]. Their results highlight the influence of a gradient on the activation of ROPs, feature known as spots-pinning phenomena, and various patches show similarities with observed distribution of hair cells. In [13] the formation and dynamics of patches of activator have been explored both numerically and analytically, to give more insights of ROPs dynamics. Multiple results are given sustaining the validity of Payne & Grierson model, particularly in capturing the process by which a patch of active ROP migrates from the apical cell boundary towards its wild-type position, where a RH actually forms. Evidence of instability of some states has been given, more precisely how a boundary patch of active ROP becomes unstable, replaced by an interior patch, in case cell length changes or auxin activation rate increases [13, 36].

From previous results, gradient seems to have the role of controlling the location of the localized pattern, through a slow-time scale patch-drift equation. Moreover it was demonstrated that it indirectly plays a role on transverse instability via the location points, specifying also the number of transverse unstable modes.

The 1D analysis of auxin gradient influence on pattern formation was extended into 2 dimensions and in [14] it was inspected the stability of patterns to transverse perturbations or what other factors causing instabilities could be. In [2] this analysis was

extended, giving more evidences on how these 2D patterns are influenced by the spatially inhomogeneous auxin distribution; the asymptotic-numerical methodology developed for RD systems with spatially homogeneous coefficients was applied in this dimensionally extended setting.

In general, reaction-diffusion equations with spatially dependent coefficients in nonlinear contributes are not easy to study analytically, therefore pattern formation in presence of spatial inhomogeneity is less well understood.

1.5. New model motivations

As we are interested in the biochemical processes and geometrical features that participate in RH initiation, the ROP model is derived via a reaction-diffusion approach in a non-homogeneous environment. Various previous studies have underlined the importance of considering this system in a 2D environment [2, 13, 14]. To recover precise information on location of patches and gradient influence at sub-cellular level, we decided to keep on solving fields representing active and inactive ROPs inside the cell, using Payne & Grierson model [35].

On the other side, some studies regarding morphogenetic processes and proteins and hormones within cells developed model for communication between cells. As stated in Section 1.3.1, the concentration- and flux-based models cited in 1.3.1 follow a different approach compared with the one for RD system inside root-hair cell. In this kind of models, the unknown variable does not consider spatial dependance inside the singular cell and the resulting problems are simple ODEs.

This approach is the only one studied until now for dealing with communication between cells and moreover it has not been studied yet a model for ROPs intercellular transport.

The goal of our thesis is to find a detailed model for root-hair initiation, taking into consideration a pluricellular system in order to couple ROPs pattern formation system with a transport model for hormone auxin. The idea behind this thesis is to join together intracellular dynamics, preserving the detailed information on the patch locations, and multicellular coupling, to deal with influence from communicating cells.

1.6. Thesis outline

We started our analysis from the previous cited considerations on parametrization and stability of systems, such as the full set of parameters chosen in [13] and the model assumed

for a single cell and for the auxin steady state distribution. We simulate the model using the Finite Element method and a semi-implicit method for time discretization, to tackle the nonlinearity of the system. We extended the model, taking into account more than 1 cell and developing a completely new model for communication between root-hair cells. Finally, we used our pluricellular model to test ROPs and auxin dynamics together. This thesis is structured as follows. In Chapter 2 we develop a full mathematical formulation for the RD system describing ROPs activation model in one single cell. In Chapter 3 we model the interactions between two or more cells, present the new mathematical method to treat a pluricellular system and respective results. In Chapter 4 we describe the biological details for auxin dynamics coupled with PIN-FORMED(PIN) proteins dynamics, join it with ROPs pluricellular model and show numerical results. Some conclusions are finally drawn in the last chapter.

2 | Spot formation in a singular cell

In this chapter we present the overall modeling of pattern formation in a system composed by one singular cell, starting from the stationary system and then considering the dynamical system. We define precisely the parameters used and the physical settings. We then give details regarding the mathematical model considered, the treatment of the nonlinear stationary system through Newton's method and the Finite Element method used to discretize the RD time-dependent system. Finally some relevant results over the singular cell simulations are given.

2.1. Physical model

The three-dimensional root-hair cell and its cell-membrane are idealized in the model considered, neglecting axial dimension and taking into account only the projection onto a 2D rectangular domain. In order to illustrate the framework, we refer to Figure 2.1 where the domain and some quantites are highlighted. The domain $\Omega = [0, L_x] \times [0, L_y] \subset \mathbb{R}^2$ presents one dominant dimension, the longitudinal one L_x , against the transversal length L_y , such that $L_x \gg L_y$. The gradient of auxin is marked in light gray shade and its flow goes from the basal end to the apical end of the plant root. Cell wall and membrane are presented by heavily dashed gray lines, the first lighter than the second. The level curves plotted in gray specify the possibility in this 2D model of dependence on y direction of auxin distribution.

The aspect ratio characterizing the rectangular domain is $s = (L_x/L_y)^2 = 5.5$ and all spatial derivatives are scaled with respect to this aspect ratio, by definition therefore:

$$\begin{aligned}\nabla_s &= [\partial_x, \sqrt{s}\partial_y], \\ \Delta_s &= \partial_x^2 + s\partial_y^2.\end{aligned}$$

In the RD model the unknowns $u(\mathbf{X}, t) : \Omega \times \mathbb{R}^+ \rightarrow \mathbb{R}$ and $v(\mathbf{X}, t) : \Omega \times \mathbb{R}^+ \rightarrow \mathbb{R}$

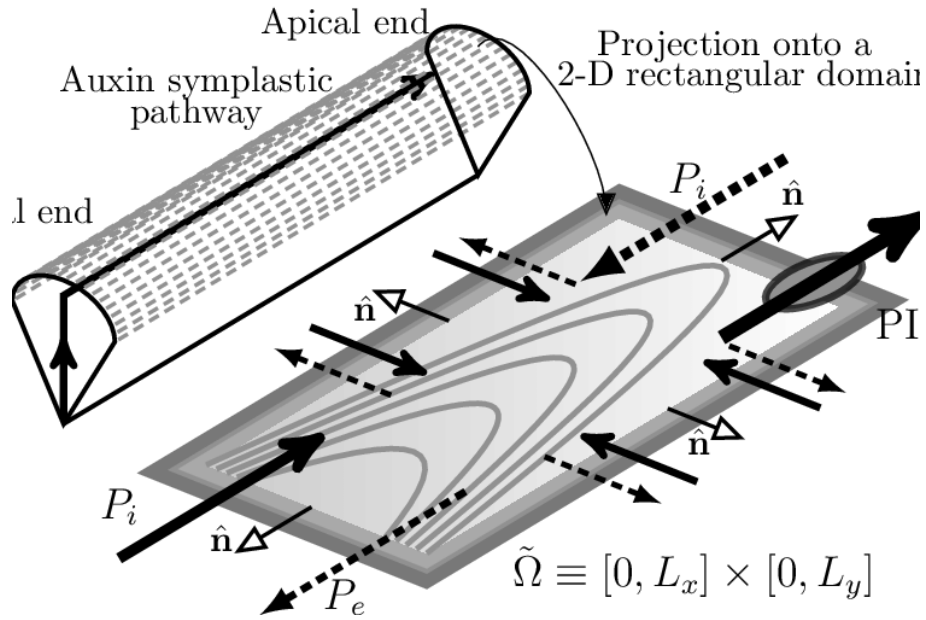


Figure 2.1: Sketch of an idealized 3D RH cell with longitudinal and transversal spatially dependent auxin flow. Figure reproduced from [2].

are the active and inactive concentration of ROPs inside the cell respectively, evaluated at generic time $t \in [0, T_{max}]$ and in the position $\mathbf{X} = (x, y) \in \Omega$.

The dimensional reaction-diffusion model summarizing binding process, autocatalytic activation and catalysis of ROPs proteins described in Section 1.2.1 is formulated as follows:

$$\begin{cases} \partial_t u = D_1 \Delta_s u + k_{20} \alpha(x, y) u^2 v - (c + r) u + k_1 v & \text{in } \Omega \\ \partial_t v = D_2 \Delta_s v - k_{20} \alpha(x, y) u^2 v - k_1 v + c u + b & \text{in } \Omega. \end{cases} \quad (2.1)$$

The model can be summarized in the following fundamental contributes:

- the source term, composed by the rate of production of inactive ROP b ;
- the linear reaction terms, composed by the constant rate for deactivation of active ROPs $k_{GAP} = c$, by the rate of usage of ROP for cell softening and subsequent hair formation r and by the activation rate k_1 (derived from (1.1) function);
- the nonlinear reaction term, coming from the rate of activation of inactive ROPs k_{GEF} assumed in (1.1);
- the diffusive part, represented by the diffusion coefficients D_1 and D_2 .

The diffusion coefficients are associated to active and inactive ROPs respectively, with $D_1 \ll D_2$. This model does not describe the binding mechanism but distinguish only between the active form, which can diffuse within the confines of the cell membrane, and

Sets of parameters

Variable	Measure Unit	Value		
		Set A	Set B	Set C
L_x	μm	50	50	70
L_y	μm	20	20	$\frac{L_x}{\sqrt{s}}$
D_1	$\mu m^2/s$	0.1	0.1	0.075
D_2	$\mu m^2/s$	10	10	20
k_1	1/s	0.01	0.01	0.008
b	1/s	0.01	0.01	0.008
c	1/s	0.1	0.1	0.1
r	1/s	0.01	0.01	0.05
k_{20}	1/s	0.1	0.1	0.5
s	-	6.25	6.27	5.5
ν	-	1.5	0	1.5

Table 2.1: Table containing the three sets of parameters used in our model.

the inactive form, the majority of which is free to diffuse in the cytoplasm. Therefore, the difference of diffusion coefficients is used to distinguish the membrane from the cytoplasm one.

The rate of activation of inactive ROP is represented by a function of the auxin distribution, as described in Section 1.2.1, depending on rate of activation k_1 , overall auxin level k_{20} and the normalized spatial distribution of auxins $\alpha(x, y)$. Usually an exponential distribution is chosen for auxin depending to coefficient ν ; in a singular cell system we assume that:

$$\alpha(x, y) = \alpha(x) = e^{-\nu \frac{x}{L_x}}. \quad (2.2)$$

The function representing auxin distribution is assumed monotone decreasing, at steady state with maximum located in correspondance to the left boundary of the cell and to vary only in x -direction.

In table 2.1 different possible values of parameters are collected with their respective unit of measure; those sets of parameters were taken from previous analysis of ROPs model system, such as from bifurcations analysis in [14].

Analytical studies of the system (2.1) and numerical simulations have been made on the

model rewritten in dimensionless form as follows:

$$\begin{cases} \partial_t u = \epsilon^2 \Delta_s u + \alpha(x) u^2 v - u + (\tau\gamma)^{-1} v & \text{in } \tilde{\Omega} \\ \partial_t v = \frac{D}{\tau} \Delta_s v - \frac{1}{\tau} v + \frac{1}{\tau} - \gamma (\alpha(x) u^2 v - u) - \frac{\beta\gamma}{\tau} u & \text{in } \tilde{\Omega}. \end{cases} \quad (2.3)$$

The dimensionless model is solved on the squared domain $\tilde{\Omega} = (0, 1) \times (0, 1)$. The parameters used in the system of equations (2.3) are obtained rescaling the ones in (2.1) and therefore defined in terms of the original parameters through:

$$\epsilon^2 \equiv \frac{D_1}{L_x^2(c+r)}, \quad D \equiv \frac{D_2}{L_x^2 k_1}, \quad \tau \equiv \frac{c+r}{k_1}, \quad \beta \equiv \frac{r}{k_1}. \quad (2.4)$$

Under homogeneous auxin distribution $\alpha(x) \equiv 1$, there is an equilibrium solution of the rescaled problem (2.3), found in [14]:

$$u = u_0 \equiv \frac{1}{\gamma\beta}, \quad v = v_0 \equiv \frac{\tau\beta\gamma}{\tau + \beta^2\gamma}. \quad (2.5)$$

The RD system is rewritten to explicit its mathematical formulation and methods in order to solve it in the most general way, including both the case of the RD system with the original parameters and the RD system with the rescaled ones.

As a consequence, we define a unified system of equations comprehensive of both (2.1) and (2.3) systems:

$$\begin{cases} \partial_t u = \tilde{D}_1 \Delta_s u + \tilde{a}_1 u + \tilde{b}_1 v + \tilde{c}_1 u^2 v & \text{in } \Omega \\ \partial_t v = \tilde{D}_2 \Delta_s v + \tilde{a}_2 v + \tilde{b}_2 u + \tilde{c}_2 u^2 v + f_2 & \text{in } \Omega, \end{cases} \quad (2.6)$$

with tilde parameters defined differently in the two cases under study; in particular, in case we are referring to the original system we have:

$$\begin{aligned} \tilde{D}_1 &= D_1, & \tilde{D}_2 &= D_2, \\ \tilde{a}_1 &= -(c+r), & \tilde{a}_2 &= -k_1, \\ \tilde{b}_1 &= k_1, & \tilde{b}_2 &= c, \\ \tilde{c}_1 &= k_{20}\alpha(x), & \tilde{c}_2 &= -k_{20}\alpha(x), \\ f_2 &= b, \end{aligned} \quad (2.7)$$

whereas in case we are referring to the rescaled system we have:

$$\begin{aligned} \tilde{D}_1 &= \epsilon^2, & \tilde{D}_2 &= \frac{D}{\tau}, \\ \tilde{a}_1 &= -1, & \tilde{a}_2 &= -\frac{1}{\tau}, \\ \tilde{b}_1 &= \frac{1}{\tau\gamma}, & \tilde{b}_2 &= \gamma - \frac{\beta\gamma}{\tau} = \gamma \left(1 - \frac{\beta}{\tau}\right), \\ \tilde{c}_1 &= \alpha(x), & \tilde{c}_2 &= -\gamma\alpha(x), \\ f_2 &= \frac{1}{\tau}. \end{aligned} \tag{2.8}$$

We complete system of spot formation model regarding 1 cell with homogeneus Neumann boundary conditions, in order to consider no-flux of ROPs outside the cell:

$$D_1 \nabla_s u \cdot \mathbf{n} = 0, \quad D_2 \nabla_s v \cdot \mathbf{n} = 0 \quad \text{on } \partial\Omega.$$

2.2. Numerical treatment

Regarding the numerical approximation of the RD system, we choose to solve the two partial differential equations using the Finite Element method for the space discretization and a semi-implicit scheme for time discretization. Before applying the time-discretization scheme, we test whether the system is stable under homogeneous distribution of auxin and a chosen set of parameters. Indeed, in previous works the instability of this kind of RD system and sensitivity with respect to the parameters and general setting used has been investigated [2, 13].

In the following sections we detail the discretization of the stationary system, used to find steady states of the set of parameters, as well as the full formulation of the semi-implicit method for the time-dependent problem.

2.2.1. Stationary system

Model system in (2.6) can be synthetically rewritten as:

$$\dot{U} = G(U) = LU + N(U) \quad \text{in } \Omega, \tag{2.9}$$

being $U = [u, v] : \Omega \times \mathbb{R}^+ \rightarrow \mathbb{R}^2$ and G defined from (2.6) as:

$$G(U) = \begin{bmatrix} \tilde{D}_1\Delta_s + \tilde{a}_1 & \tilde{b}_1 \\ \tilde{b}_2 & \tilde{D}_2\Delta_s + \tilde{a}_2 \end{bmatrix} \begin{bmatrix} u \\ v \end{bmatrix} + \begin{bmatrix} \tilde{c}_1 u^2 v \\ \tilde{c}_2 u^2 v \end{bmatrix} + \begin{bmatrix} 0 \\ f_2 \end{bmatrix}. \quad (2.10)$$

The linear part contribute of the operator is defined as

$$LU = \begin{bmatrix} \tilde{D}_1\Delta_s + \tilde{a}_1 & \tilde{b}_1 \\ \tilde{b}_2 & \tilde{D}_2\Delta_s + \tilde{a}_2 \end{bmatrix} \begin{bmatrix} u \\ v \end{bmatrix}, \quad (2.11)$$

and the nonlinear one as

$$N(U) = \begin{bmatrix} \tilde{c}_1 u^2 v \\ \tilde{c}_2 u^2 v \end{bmatrix}. \quad (2.12)$$

We can find stationary solutions of the system solving the nonlinear problem:

$$G(U) = LU + N(U) = 0 \text{ in } \Omega. \quad (2.13)$$

Consider the following functional Hilbert space for the concentrations of active and inactive ROPs:

$$V = H^1(\Omega) = \{w \in L^2(\Omega) : \nabla w \in L^2(\Omega; \mathbb{R}^2)\}. \quad (2.14)$$

By applying Newton's method, we solve the iterative method:

Given $U^0 \in [H^1(\Omega)]^2$, find $U^{k+1} \in [H^1(\Omega)]^2$ such that:

$$\begin{cases} D_U G(U)|_{U^k}(\delta U) = -G(U^k) \\ U^{k+1} = U^k + \delta U \\ \Updownarrow \\ \begin{cases} D_{(u,v)} G((u,v))|_{(u^k, v^k)}((\delta u, \delta v)) = -G((u^k, v^k)) \\ (u^{k+1}, v^{k+1}) = (u^k, v^k) + (\delta u, \delta v), \end{cases} \end{cases} \quad (2.15)$$

$\forall k = 0, 1, \dots$ up to convergence. Here $D_U G(U)|_{U^k}(\delta U)$ denotes the directional derivative of operator G along the direction $\delta U = (\delta u, \delta v)$ evaluated at (u^k, v^k) . The Gateaux

derivative is obtained as follows:

$$\begin{aligned}
 D_U G(U) &= L + D_U N(U), \\
 D_U N(U)|_U(\delta U) &= D_{(u,v)}N((u,v))|_{(u^k,v^k)}((\delta u, \delta v)) \\
 &= \lim_{\epsilon \rightarrow 0} \frac{1}{\epsilon} \begin{bmatrix} \tilde{c}_1(u + \epsilon \delta u)^2(v + \epsilon \delta v) - \tilde{c}_1 u^2 v \\ \tilde{c}_2(u + \epsilon \delta u)^2(v + \epsilon \delta v) - \tilde{c}_2 u^2 v \end{bmatrix} = \begin{bmatrix} \tilde{c}_1 2uv \delta u + \tilde{c}_1 u^2 \delta v \\ \tilde{c}_2 2uv \delta u + \tilde{c}_2 u^2 \delta v \end{bmatrix}.
 \end{aligned} \tag{2.16}$$

The formulation of the Newton's tangent problem therefore reads as:

Given $(u^0, v^0) \in [H^1(\Omega)]^2$, find $(u^{k+1}, v^{k+1}) \in [H^1(\Omega)]^2$ such that:

$$\begin{aligned}
 \begin{bmatrix} \tilde{D}_1 \Delta_s + \tilde{a}_1 + \tilde{c}_1 2u^k v^k & \tilde{b}_1 + \tilde{c}_1 u^{k^2} \\ \tilde{b}_2 + \tilde{c}_2 2u^k v^k & \tilde{D}_2 \Delta_s + \tilde{a}_2 + \tilde{c}_2 u^{k^2} \end{bmatrix} \begin{bmatrix} \delta u \\ \delta v \end{bmatrix} = \\
 - \begin{bmatrix} \tilde{D}_1 \Delta_s + \tilde{a}_1 & \tilde{b}_1 \\ \tilde{b}_2 & \tilde{D}_2 \Delta_s + \tilde{a}_2 \end{bmatrix} \begin{bmatrix} u^k \\ v^k \end{bmatrix} - \begin{bmatrix} \tilde{c}_1 u^{k^2} v^k \\ \tilde{c}_2 u^{k^2} v^k \end{bmatrix} - \begin{bmatrix} 0 \\ f_2 \end{bmatrix} \\
 \begin{bmatrix} u^{k+1} \\ v^{k+1} \end{bmatrix} = \begin{bmatrix} u^k \\ v^k \end{bmatrix} + \begin{bmatrix} \delta u \\ \delta v \end{bmatrix}
 \end{aligned} \tag{2.17}$$

$\forall k = 0, 1, \dots$ up to convergence.

In order to explicit the weak formulation of the tangent problem, we take a test function $w \in V$ and we obtain:

$$\begin{cases} a_u(\delta u, w) + b_u(\delta v, w) + c_{uu}(\delta u, w) + c_{uv}(\delta v, w) = -g_u(w) \quad \forall w \in V \\ a_v(\delta v, w) + b_v(\delta u, w) + c_{vu}(\delta u, w) + c_{vv}(\delta v, w) = -g_v(w) \quad \forall w \in V \end{cases} \tag{2.18}$$

where

- $a_u(\delta u, w) = \int_{\Omega} -\tilde{D}_1 \nabla_s \delta u \cdot w + \tilde{a}_1 \delta u w$
- $b_u(\delta v, w) = \int_{\Omega} \tilde{b}_1 \delta v w$
- $c_{uu}(\delta u, w) = \int_{\Omega} 2\tilde{c}_1 u^k v^k \delta u w$
- $c_{uv}(\delta v, w) = \int_{\Omega} \tilde{c}_1 u^{k^2} \delta v w$
- $a_v(\delta v, w) = \int_{\Omega} -\tilde{D}_2 \nabla_s \delta v \cdot w + \tilde{a}_2 \delta v w$
- $b_v(\delta u, w) = \int_{\Omega} \tilde{b}_2 \delta u w$
- $c_{vu}(\delta u, w) = \int_{\Omega} 2\tilde{c}_2 u^k v^k \delta u w$
- $c_{vv}(\delta v, w) = \int_{\Omega} \tilde{c}_2 u^{k^2} \delta v w$

- $g_u(w) = a_u(u^k, w) + b_u(v^k, w) + \int_{\Omega} \tilde{c}_1 u^{k^2} v^k w$
- $g_v(w) = a_v(v^k, w) + b_v(u^k, w) + \int_{\Omega} \tilde{c}_2 u^{k^2} v^k w + \int_{\Omega} f_2 w$

In particular, there is no contribution from border values after the integration by part of the diffusive component of the equations since we have assumed Neumann homogeneous boundary conditions.

Let us introduce a computational grid τ_h on the given rectangular domain and a finite dimensional functional space $V_h \subset V$; precisely, V_h is the space of linear polynomials defined over τ_h , thus:

$$V_h = \{w_h \in C^0(\bar{\Omega}), w_h|_K \in \mathbb{P}^1(K), \forall K \in \tau_h\}, \quad (2.19)$$

whose dimension is N_h and with basis $\{\phi_j\}_{j=1}^{N_h}$. The Galerkin approximation of the stationary problem then reads:

Given (u_h^0, v_h^0) , find $(u_h^{k+1}, v_h^{k+1}) \in V_h \times V_h$ such that:

$$\begin{cases} a_u(\delta u_h, w_h) + b_u(\delta v_h, w_h) + c_{uu}(\delta u_h, w_h) \\ \quad + c_{uv}(\delta v_h, w_h) = -g_u(w_h) & \forall w_h \in V_h \\ a_v(\delta v_h, w_h) + b_v(\delta u_h, w_h) + c_{vu}(\delta u_h, w_h) \\ \quad + c_{vv}(\delta v_h, w_h) = -g_v(w_h) & \forall w_h \in V_h \\ (u_h^{k+1}, v_h^{k+1}) = (u_h^{k+1}, v_h^{k+1}) + (\delta u_h, \delta v_h), \end{cases} \quad (2.20)$$

$\forall k = 0, 1, 2, \dots$ up to convergence.

We can pass to the algebraic formulation of (2.20). The two solutions of the problem can be written as linear combination of the basis functions as follows:

$$\delta u_h(x, y) = \sum_{j=i}^{N_h} du_j \phi_j(x, y), \quad \delta v_h(x, y) = \sum_{j=i}^{N_h} dv_j \phi_j(x, y). \quad (2.21)$$

Inside the Galerkin formulation, we replace the test function w_h with the generic element of the basis $\phi_i \forall i = 1, \dots, N_h$ thanks to linearity of the variational functional defined in (2.18), we obtain the algebraic formulation of the Newton's tangent problem:

$$\begin{bmatrix} A_u + C_{uu} & B_u + C_{uv} \\ B_v + C_{vu} & A_v + C_{vv} \end{bmatrix} \begin{bmatrix} dU \\ dV \end{bmatrix} = - \begin{bmatrix} G_u \\ G_v \end{bmatrix}, \quad (2.22)$$

being:

$$\begin{aligned}
[A_u]_{i,j} &= \int_{\Omega} \left(-\tilde{D}_1 \nabla_s \phi_j \cdot \nabla_s \phi_i + \tilde{a}_1 \phi_j \phi_i \right) \\
[A_v]_{i,j} &= \int_{\Omega} \left(-\tilde{D}_2 \nabla_s \phi_j \cdot \nabla_s \phi_i + \tilde{a}_2 \phi_j \phi_i \right) \\
[B_u]_{i,j} &= \int_{\Omega} \left(\tilde{b}_1 \phi_j \phi_i \right) \\
[B_v]_{i,j} &= \int_{\Omega} \left(\tilde{b}_2 \phi_j \phi_i \right) \\
[C_{uu}]_{i,j} &= \int_{\Omega} \left(2\tilde{c}_1 u^0 v^0 \phi_j \phi_i \right) \\
[C_{uv}]_{i,j} &= \int_{\Omega} \left(\tilde{c}_1 u^0 u^0 \phi_j \phi_i \right) \\
[C_{vu}]_{i,j} &= \int_{\Omega} \left(2\tilde{c}_2 u^0 v^0 \phi_j \phi_i \right) \\
[C_{vv}]_{i,j} &= \int_{\Omega} \left(\tilde{c}_2 u^0 u^0 \phi_j \phi_i \right) \\
[G_u]_i &= \int_{\Omega} \left(2\tilde{c}_1 u^0 u^0 v^0 \phi_i \right) \\
[G_v]_i &= \int_{\Omega} \left(2\tilde{c}_2 u^0 u^0 v^0 \phi_i \right) \\
[dU]_j &= du_j \\
[dV]_j &= dv_j
\end{aligned} \tag{2.23}$$

with $i, j = 1, \dots, N_h$.

Synthetically, the system to solve can be rewritten as:

given $\mathbf{U}^0 \in \mathbb{R}^{2N_h}$, find $\mathbf{U}^{k+1} \in \mathbb{R}^{2N_h}$ such that:

$$\begin{cases} \mathbf{J} \mathbf{dU} = -\mathbf{G}(\mathbf{U}^k) \\ \mathbf{U}^{k+1} = \mathbf{U}^k + \mathbf{dU} \end{cases} \tag{2.24}$$

$\forall k = 0, 1, 2, \dots$ up to convergence.

This represents the algebraic form of (2.15) obtained using the Finite Element method, with \mathbf{J} the Jacobian matrix of the problem defined in the finite dimensional space V_h :

$$\mathbf{J} = \begin{bmatrix} A_u + C_{uu} & B_u + C_{uv} \\ B_v + C_{vu} & A_v + C_{vv} \end{bmatrix}. \tag{2.25}$$

At each iteration k of the iterative method the new solution $\mathbf{U}^{k+1} = (U^{k+1}, V^{k+1})$ is updated up to convergence. We have used two convergence criteria: we check whether

the normalized residual, measured using the L^2 norm in space, is smaller than a desired tolerance `tol` or if a maximum number of iterations `MAXiter` has been performed. In particular, the residual is computed as follows:

$$\text{res}_u = \frac{\|u^{k+1} - u^k\|_{L^2(\Omega)}}{\|u^k\|_{L^2(\Omega)}}, \quad \text{res}_v = \frac{\|v^{k+1} - v^k\|_{L^2(\Omega)}}{\|v^k\|_{L^2(\Omega)}}. \quad (2.26)$$

2.2.2. Time-dependent scheme

Similarly as done in the previous section, we briefly recall the Finite Element method applied on the time-dependent system in (2.6). Considering the Hilbert space V defined in (2.14), the two partial differential equations can be rewritten in weak form:

Given an initial state $(u(t=0), v(t=0)) = (u^0, v^0)$, find $(u(t), v(t)) \in [H^1(\Omega)]^2$ such that

$$\begin{cases} \tilde{a}_u(u(t), w) + \tilde{b}_u(v(t), w) + \tilde{c}_u(u(t), v(t), w) = \tilde{f}_u(w) \quad \forall w \in V \\ \tilde{a}_v(v(t), w) + \tilde{b}_v(u(t), w) + \tilde{c}_v(u(t), v(t), w) = \tilde{f}_v(w) \quad \forall w \in V. \end{cases} \quad (2.27)$$

where the variational forms are here defined as:

- $\tilde{a}_u(u, w) = \int_{\Omega} \frac{\partial u_h}{\partial t} w + \tilde{D}_1 \nabla_s u \cdot w - \tilde{a}_1 uw$
- $\tilde{b}_u(v, w) = \int_{\Omega} -\tilde{b}_1 vw$
- $\tilde{c}_u(u, v, w) = \int_{\Omega} -\tilde{c}_1 u^2 vw$
- $\tilde{a}_v(v, w) = \int_{\Omega} \frac{\partial v_h}{\partial t} w + \tilde{D}_2 \nabla_s v \cdot w - \tilde{a}_2 vw$
- $\tilde{b}_v(u, w) = \int_{\Omega} -\tilde{b}_2 uw$
- $\tilde{c}_v(u, v, w) = \int_{\Omega} -\tilde{c}_2 u^2 vw$
- $\tilde{f}_u = 0$
- $\tilde{f}_v = \int_{\Omega} f_2 w$

For the space discretization we introduce the computational grid τ_h of the rectangular domain Ω and derive the Galerkin formulation taking as functional space $V_h \subset V$, the finite element space of piecewise linear polynomials defined over τ_h , defined as in (2.19). Taking as test function the generic function $w_h \in V_h$, the Galerkin formulation reads as:

find $(u_h, v_h) \in V_h \times V_h$ such that

$$\begin{cases} \tilde{a}_u(u_h(t), w_h) + \tilde{b}_u(v_h(t), w_h) + \tilde{c}_u(u_h(t), v_h(t), w_h) = \tilde{f}_u(w_h) \quad \forall w_h \in V_h \\ \tilde{a}_v(v_h(t), w_h) + \tilde{b}_v(u_h(t), w_h) + \tilde{c}_v(u_h(t), v_h(t), w_h) = \tilde{f}_v(w_h) \quad \forall w_h \in V_h. \end{cases} \quad (2.28)$$

The problem is still time-dependent and thus this is only a semi-discrete formulation. We need to define a method for time-discretization. The system in (2.28) is characterized by the nonlinear relationship between the two variables $u(x, y)$ and $v(x, y)$ inside the variational forms $\tilde{c}_u(u, v, w)$ and $\tilde{c}_v(u, v, w)$; moreover the time range in which patches and ROPs dynamics are fomed is big. As a consequence, in order to handle the complexity and computational cost associated with the system, we use a semi-implicit time discretization scheme.

In particular, we discretize the time derivative using the implicit Euler method; we divide the time interval $[0, T_{max}]$ into uniform sub-intervals of Δt amplitude and define $U^n := (u^n, v^n) \simeq (u(t^n), v(t^n))$. Taking as starting equation (2.9), implicit Euler method schematically reads:

$$\frac{U^{n+1} - U^n}{\Delta t} = G(U^{n+1}) = LU^{n+1} + N(U^{n+1}) \text{ in } \Omega. \quad (2.29)$$

Problem in (2.29) is fully implicit and it require a nonlinear model to solve at each time step. For the semi-implicit scheme, we decide to treat implicitly the linear part only, while discretizing explicitly the component of the nonlinear part responsible for the nonlinearity, in the following way:

$$\frac{U^{n+1} - U^n}{\Delta t} = LU^{n+1} + \tilde{N}(U^n, U^{n+1}) \text{ in } \Omega, \quad (2.30)$$

$$\text{where } \tilde{N}(U^n, U^{n+1}) = \begin{bmatrix} \tilde{c}_1(u^n)^2 v^{n+1} \\ \tilde{c}_2(u^n)^2 v^{n+1} \end{bmatrix}.$$

In this way our system has been linearized and the full Galerkin formulation after time discretization is:

given the initial state (u_h^0, v_h^0) , find $(u_h^{n+1}, v_h^{n+1}) \in V_h \times V_h$ such that

$$\begin{cases} a_u(u_h^{n+1}, w_h) + b_u(v_h^{n+1}, w_h) + c_u(v_h^{n+1}, w_h) = f_u(w_h) \quad \forall w_h \in V_h \\ a_v(v_h^{n+1}, w_h) + b_v(u_h^{n+1}, w_h) + c_v(v_h^{n+1}, w_h) = f_v(w_h) \quad \forall w_h \in V_h, \end{cases} \quad (2.31)$$

where we have redefined the bilinear forms as:

- $a_u(u, w) = \int_{\Omega} \frac{1}{\Delta t} uw + \tilde{D}_1 \nabla_s u \cdot w - \tilde{a}_1 u w$
- $b_u(v, w) = \int_{\Omega} -\tilde{b}_1 v w$
- $c_u(v, w) = \int_{\Omega} -\tilde{c}_1 (u^n)^2 v w$
- $a_u(u, w) = \int_{\Omega} \frac{1}{\Delta t} v w + \tilde{D}_2 \nabla_s v \cdot w - \tilde{a}_2 v w$
- $b_u(v, w) = \int_{\Omega} -\tilde{b}_2 u w$
- $c_u(v, w) = \int_{\Omega} -\tilde{c}_2 (u^n)^2 v w$
- $f_u = \int_{\Omega} \frac{1}{\Delta t} u^n w$
- $f_v = \int_{\Omega} \frac{1}{\Delta t} v^n w + f_2 w$

We then write the solutions as linear combinations of the finite dimensional space scalar basis function $\{\phi\}_{j=1}^{N_h}$:

$$u_h^n(x, y) = \sum_{j=i}^{N_h} u_j^n \phi_j(x, y), \quad v_h^n(x, y) = \sum_{j=i}^{N_h} v_j^n \phi_j(x, y), \quad (2.32)$$

we take as test function $w = \phi_i \forall i = 1, \dots, N_h$. The algebraic problem to solve at each time step is therefore:

Given $\begin{bmatrix} \mathbf{U}^0 \\ \mathbf{V}^0 \end{bmatrix} \in \mathbb{R}^{2N_h}$, for $t^n = 0, \dots, T_{max}$ find $\begin{bmatrix} \mathbf{U}^{n+1} \\ \mathbf{V}^{n+1} \end{bmatrix} \in \mathbb{R}^{2N_h}$ such that:

$$\begin{bmatrix} A_u & B_u + C_u(\mathbf{U}^n) \\ B_v & A_v + C_v(\mathbf{U}^n) \end{bmatrix} \begin{bmatrix} \mathbf{U}^{n+1} \\ \mathbf{V}^{n+1} \end{bmatrix} = \begin{bmatrix} F_u \\ F_v \end{bmatrix}, \quad (2.33)$$

where the involved matrices and vectors are defined in the following way:

$$\begin{aligned}
[A_u]_{i,j} &= \int_{\Omega} \left(\frac{1}{\Delta t} - \tilde{a}_1 \right) \phi_j \phi_i + \int_{\Omega} \tilde{D}_1 \nabla_s \phi_j \cdot \nabla_s \phi_i \\
[A_v]_{i,j} &= \int_{\Omega} \left(\frac{1}{\Delta t} - \tilde{a}_2 \right) \phi_j \phi_i + \int_{\Omega} \tilde{D}_2 \nabla_s \phi_j \cdot \nabla_s \phi_i \\
[B_u]_{i,j} &= \int_{\Omega} -\tilde{b}_1 \phi_j \phi_i \\
[B_v]_{i,j} &= \int_{\Omega} -\tilde{b}_2 \phi_j \phi_i \\
[C_u(u^n)]_{i,j} &= \int_{\Omega} -\tilde{c}_1 (u^n)^2 \phi_j \phi_i \\
[C_v(v^n)]_{i,j} &= \int_{\Omega} -\tilde{c}_2 (v^n)^2 \phi_j \phi_i \\
[F_u]_i &= \int_{\Omega} \frac{u^n}{\Delta t} \phi_i \\
[F_v]_i &= \int_{\Omega} \frac{v^n}{\Delta t} \phi_i + f_2 \phi_i \\
[\mathbf{U}^n]_i &= u_i^n \\
[\mathbf{V}^n]_i &= v_i^n.
\end{aligned} \tag{2.34}$$

The system obtained is linear and therefore we overcome the computational cost of solving a nonlinear method at each time-step of the scheme.

2.3. Numerical results

We report here some results obtained using the 1 cell solver implemented using methods detailed in the previous section. In the first subsection we validate the implementation of Newton's method, solving the stationary system under set B of parameters (Table 2.1). The second section provides the result of the dynamics obtained perturbing the steady state solution of the stationary problem found under set C of parameters (Section 2.2.1), in order to verify if the semi-implicit method (2.33) converges back to the stable steady solution. This validation has been performed because of the numerous analysis found in other works on ROPs systems stressing the instability and sensitivity to parameters settings of this kind of systems [11, 26]. In Section 2.3.3 the order of convergence of our semi-implicit method to the exact solution with respect to time is empirically computed. Then, one particular spot formation is shown, obtained solving the ROPs system using set C of parameters in Table 2.1, corresponding therefore to the original set of the physical model.

All the tests were implemented through **FreeFEM**, an open-source partial differential equations solver written in C++ [20]. The linear system defined in (2.33) is not symmetric, therefore we choose UMFPACK solver, predefined inside **FreeFem++** library and recommended for non symmetric systems.

2.3.1. Validation of steady state under homogeneous regime

The problem under investigation is characterized by a homogeneous auxin distribution, having $\nu = 0$, and the equilibrium of this particular system has been recovered analytically, specified in parameters u_0 and v_0 (2.5) and visualized in Figure 2.2.

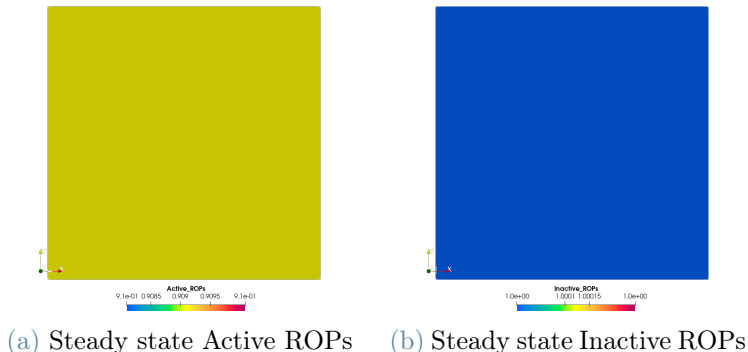


Figure 2.2: Equilibrium of the adimensional ROPs system under homogeneous auxin distribution.

We validate Newton's method by initializing the stationary system with periodic perturbation of the equilibrium with amplitude proportional to $\tilde{\epsilon}$ variable, corresponding to `eps` parameter in the code; thus the perturbation applied to equilibrium is defined in this way:

```
24 Xh pert; //custom perturbation of initial state
25 pert = eps * cos(2*pi*x)* cos(2*pi*y); // "Set A", "Set B"
26 // pert = eps * cos(2*pi*x/Lx)* cos(2*pi*y/Ly); // "Set C"
```

Listing 2.1: 1cell_stationaryTest.edp: perturbation of the equilibrium

Newton's method is configured with `MAXiter = 200` and `tol = 1e-12` for all the results here shown.

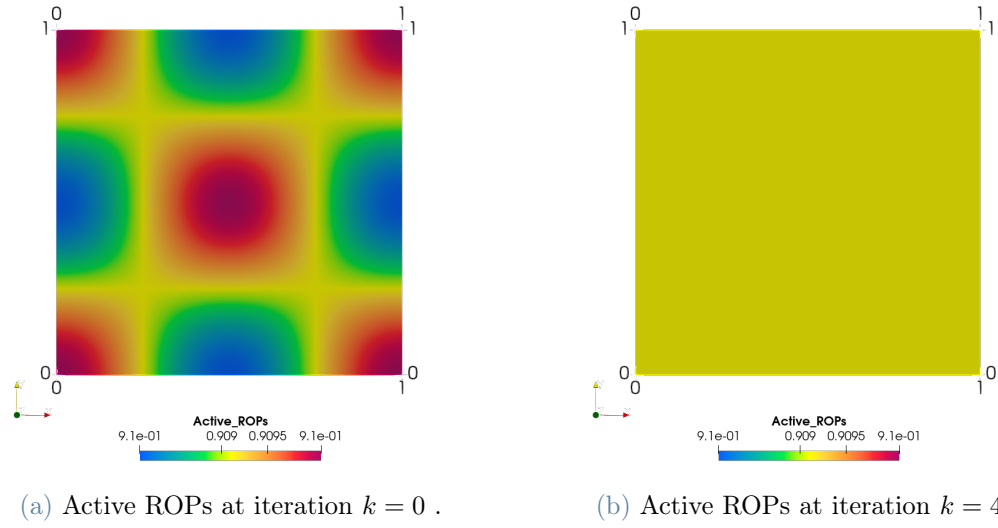


Figure 2.3: Newton’s method solution for constant homogeneous auxin distribution $\alpha = 1$, with parameter Set B and $\tilde{\epsilon} = 10^{-3}$.

In Figure 2.3 initial state and converged solution for a perturbed equilibrium characterized by $\tilde{\epsilon} = 10^{-3}$ at iteration $k = 4$ are shown. Increasing the perturbation to $\tilde{\epsilon} = 10^{-2}$, 5 iterations are necessary to reach the desired tolerance, as shown in Figure 2.4. The

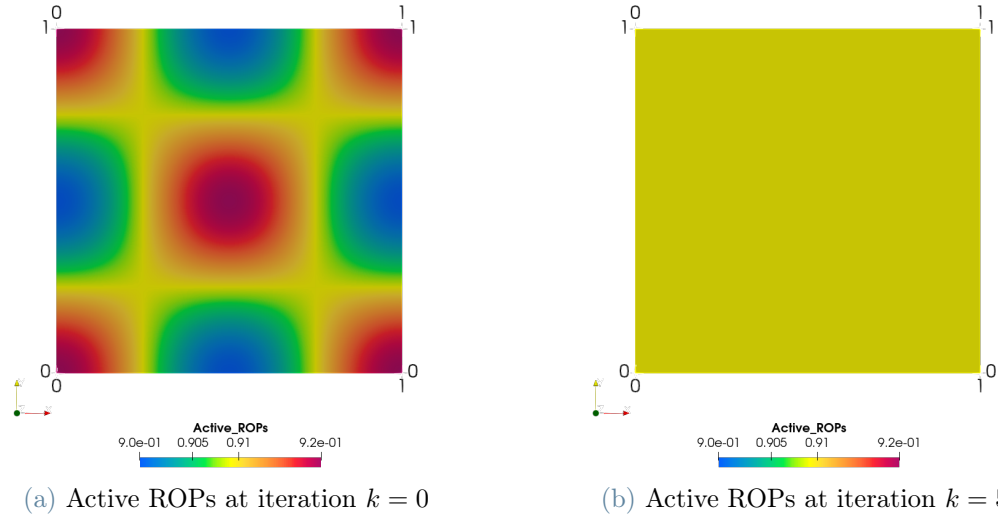


Figure 2.4: Newton’s method solution for constant homogeneous auxin distribution $\alpha = 1$, with parameter Set B and $\tilde{\epsilon} = 10^{-2}$.

bigger the perturbation, the higher number of iterations are necessary to go back to the homogeneous equilibrium of the system. This results sufficiently validate our stationary system and the system we expect it converges to.

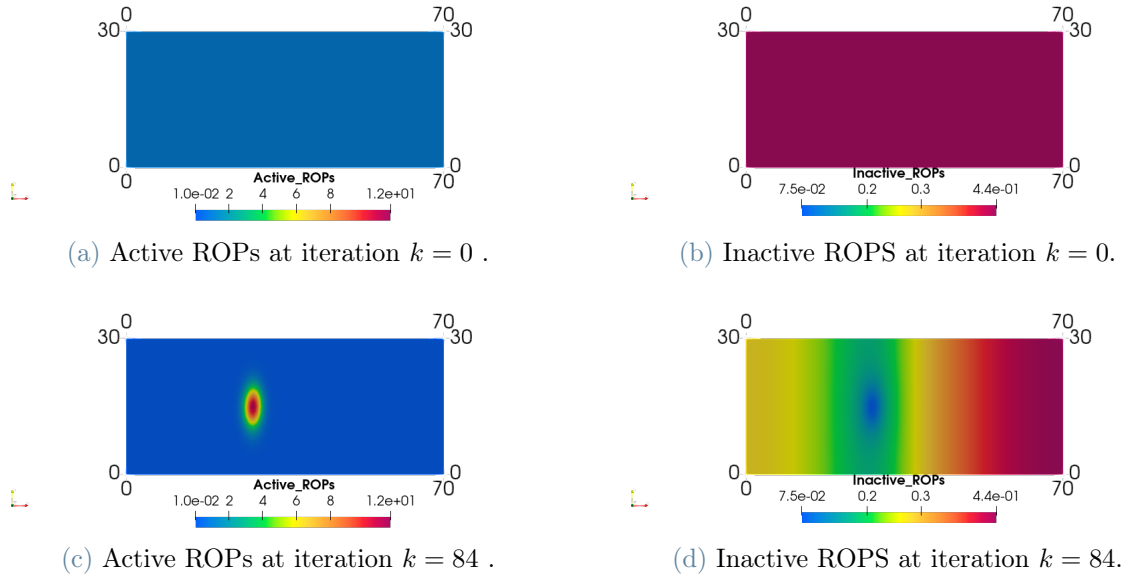


Figure 2.5: Solutions of the non homogeneous stationary problem system obtained at convergence.

2.3.2. Validation of semi-implicit method with a steady state under not homogeneous regime

We set the parameters as in Table 2.1 - Set C. The auxin distribution is chosen not homogeneous as in (2.2). The system was initialized using as starting guess for Newton's method, namely the homogeneous constant solution:

$$u^0 = 0.9, \quad v^0 = 1.0$$

Under different distribution of auxin, the system converges to another equilibrium, different from the cited one in [14] and validated in Section 2.3.1; in order to obtain the new steady state, it has been used as convergence criterion for Newton's method a tolerance `tol = 1e-12` and `MAXiter = 200`. The stationary system converges to a one spot solution for the active ROP as shown in Figure 2.5c-2.5d, stopping at iteration $k = 84$ and reaching a residual of $4.76187e-13$. The obtained solution is the equilibrium of the ROPs system under the whole settings.

We want to validate the semi-implicit method: we start from the perturbed equilibrium in Figures 2.5c-2.5d and we verify that the system converges back to it. The initial state of concentrations $[\mathbf{U}^0, \mathbf{V}^0]$ was obtained perturbing the equilibrium with a periodic function

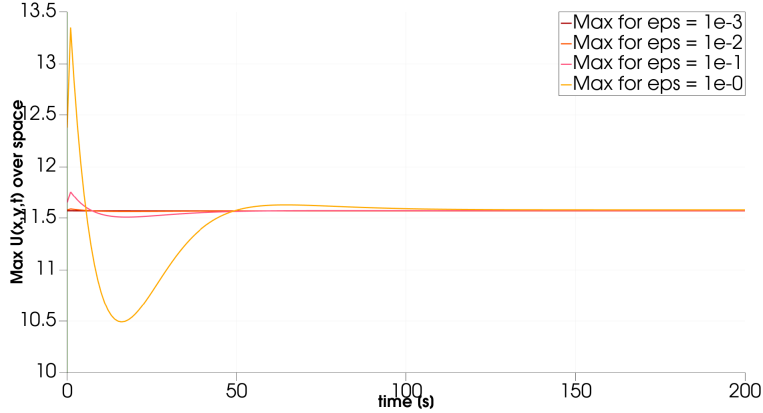


Figure 2.6: Maximum of active concentration ROPs over time

	$\bar{\epsilon} = 10^{-3}$	$\bar{\epsilon} = 10^{-2}$	$\bar{\epsilon} = 10^{-1}$	$\bar{\epsilon} = 10^{-0}$
$\ \bar{\mathbf{U}} - \mathbf{U}_h\ _{L^\infty(\Omega)} / \ \bar{\mathbf{U}}\ _{L^\infty(\Omega)}$	4.59967e-07	1.9993e-04	1.99633e-03	2.05963e-02
$\ \bar{\mathbf{V}} - \mathbf{V}_h\ _{L^\infty(\Omega)} / \ \bar{\mathbf{V}}\ _{L^\infty(\Omega)}$	8.23218e-08	3.57118e-05	3.56417e-4	3.65996e-3

Table 2.2: Errors computed with normalized $L^\infty(\Omega)$ norm of the difference between equilibrium of the system and the converged solution at $t = 200s$.

of space, modulated with a coefficient $\bar{\epsilon}$ as follows:

$$\begin{aligned} U &= u^0 + \bar{\epsilon} \cos(2\pi \frac{x}{L_x}) \cos(2\pi \frac{y}{L_y}) \\ V &= v^0 + \bar{\epsilon} \cos(2\pi \frac{x}{L_x}) \cos(2\pi \frac{y}{L_y}) \end{aligned} \quad (2.35)$$

We report then the solution of the 1 cell solver with final time $T_{max} = 200s$, obtained with the same set C of parameters. We plot over time the maximum value of the active concentration of ROPs obtained varying initialization characterized by $\bar{\epsilon} = 10^{-p}$ with p going from 3 to 0. For each of this initial states, the semi-implicit solver implemented converges back to the equilibrium as can be recovered from Figure 2.6.

We compare the four solutions obtained at $t = 200s$ with the equilibrium found in the stationary problem. We give as estimate of the error the $L^\infty(\Omega)$ norm of the difference between each final solutions obtained and the stationary one, normalized with the $L^\infty(\Omega)$ norm of the equilibrium solution. The computed errors are reported in Table 2.2.

2.3.3. Single cell solver convergence analysis

In this section we present the procedure we used to recover the order of convergence of our method with respect to time interval refinement Δt . Since the semi-implicit method we applied to solve the RD system under spatial dependent coefficients, we tried to find out empirically the order of convergence of our method.

The system is sensitive to parameters settings and initialization, therefore we decided to take as exact solution of our system the equilibrium under perturbation obtained as in Section 2.3.2, increasing the mesh refinement. More precisely, we solve the stationary system under non-homogeneous auxin distribution $k_{20}\alpha(x) = k_{20}e^{-\nu \frac{x}{L_x}}$ with set C of parameters (Table 2.1) and refining mesh using $N_x = 800$ intervals on x side and $N_y = 240$ intervals on y side. Newton's method reaches convergence in 80 iterations; we then solve the time dependent problem using as initial state the stationary solution obtained at iteration 80 perturbed with the periodic function in (2.35), with $\tilde{\epsilon} = 1$. We solve the system reducing the time-step length up to $\Delta t = 0.001$ and save results for every instant solved up to time $T_{max} = 5.0s$. The finite element solution obtained with high mesh refinement and small time discretization is taken as reference solution for our analysis:

$$(u_{ex}, v_{ex}) = (U_{h,ex}(t), V_{h,ex}(t))$$

In order to inspect the order of convergence with respect to time we run the code for semi-implicit solver for many different values of Δt . We introduce a loop over possible values of $\Delta t \in DT = [\Delta t_0, \Delta t_1 \dots]$ and we compute the errors of the obtained solution at each time step with respect to the exact solution using different norms. We detail each norm and corresponding formula of approximation:

L^∞ norm over time of the L^2 norm in space

$$\begin{aligned} \|U - u_{ex}\|_{L^\infty(0,T;L^2(\Omega))} &= \sup_{t \in (0,T)} \|U_h(t) - U_{h,ex}(t)\|_{L^2(\Omega)} \\ &\simeq \max_{n=0,\dots,M} \|U_h^n - U_{h,ex}^n\|_{L^2(\Omega)} \\ \|V - v_{ex}\|_{L^\infty(0,T;L^2(\Omega))} &= \sup_{t \in (0,T)} \|V_h(t) - V_{h,ex}(t)\|_{L^2(\Omega)} \\ &\simeq \max_{n=0,\dots,M} \|V_h^n - V_{h,ex}^n\|_{L^2(\Omega)} \end{aligned} \tag{2.36}$$

L^2 norm over time of the L^1 norm in space

$$\begin{aligned}
\|U - u_{ex}\|_{L^2(0,T;L^1(\Omega))} &= \sqrt{\int_0^T (\|U_h(t) - U_{h,ex}(t)\|_{L^1(\Omega)})^2 dt} \\
&\simeq \sqrt{\frac{\Delta t}{2} \|U_h^M - U_{h,ex}^M\|_{L^1(\Omega)}^2 + \Delta t \sum_{n=1}^{M-1} \|U_h^n - U_{h,ex}^n\|_{L^1(\Omega)}^2} \\
\|V - v_{ex}\|_{L^2(0,T;L^1(\Omega))} &= \sqrt{\int_0^T (\|V_h(t) - V_{h,ex}(t)\|_{L^1(\Omega)})^2 dt} \\
&\simeq \sqrt{\frac{\Delta t}{2} (\|V_h^M - V_{h,ex}^M\|_{L^1(\Omega)}^2) + \Delta t \sum_{n=1}^{M-1} \|V_h^n - V_{h,ex}^n\|_{L^1(\Omega)}^2}
\end{aligned} \tag{2.37}$$

 L^2 norm over time of the H^1 norm in space

$$\begin{aligned}
\|U - u_{ex}\|_{L^2(0,T;H^1(\Omega))} &= \sqrt{\int_0^T (\|U_h(t) - U_{h,ex}(t)\|_{H^1(\Omega)})^2 dt} \\
&\simeq \sqrt{\frac{\Delta t}{2} \|U_h^M - U_{h,ex}^M\|_{H^1(\Omega)}^2 + \Delta t \sum_{n=1}^{M-1} \|U_h^n - U_{h,ex}^n\|_{H^1(\Omega)}^2} \\
\|V - v_{ex}\|_{L^2(0,T;H^1(\Omega))} &= \sqrt{\int_0^T (\|V_h(t) - V_{h,ex}(t)\|_{H^1(\Omega)})^2 dt} \\
&\simeq \sqrt{\frac{\Delta t}{2} (\|V_h^M - V_{h,ex}^M\|_{H^1(\Omega)}^2) + \Delta t \sum_{n=1}^{M-1} \|V_h^n - V_{h,ex}^n\|_{H^1(\Omega)}^2}
\end{aligned} \tag{2.38}$$

Norms in (2.37) - (2.38) are approximated with composite trapezoidal formula [38].

The order of convergence is then estimated by the following formula:

$$\alpha \simeq \frac{\log(\text{err}(\Delta t_i)/\text{err}(\Delta t_{i+1}))}{\log(\Delta t_i/\Delta t_{i+1})} =: \alpha_{i,i+1} \tag{2.39}$$

where $\text{err}(\Delta t_i)$ has to be replaced with the different kind of errors computed with $\Delta t = \Delta t_i$. This estimation gets more exact for decreasing values of time-step length, i.e., for $\Delta t \rightarrow 0$.

Defining the order estimation $\alpha_{i,i+1}$ as in formula (2.39), Table 2.3 reports the results that we obtain with $\Delta t \in [0.2, 0.125, 0.1, 0.05, 0.025, 0.01, 0.005]$:

The order computed with error in the $L^2(0, T, H^1(\Omega))$ norm is bigger than the other.

	$\alpha_{0,1}$	$\alpha_{1,2}$	$\alpha_{2,3}$	$\alpha_{3,4}$	$\alpha_{4,5}$	$\alpha_{5,6}$
$\ \mathbf{U} - \mathbf{U}_{h,\text{ex}}\ _{L^\infty(0, T_{\max}; \mathbf{L}^2(\Omega))}$	0.3182	0.4998	0.7059	0.8312	0.9596	1.1123
$\ \mathbf{V} - \mathbf{V}_{h,\text{ex}}\ _{L^\infty(0, T_{\max}; \mathbf{L}^2(\Omega))}$	0.7238	0.9478	0.8810	0.9632	1.0410	1.1565
$\ \mathbf{U} - \mathbf{U}_{h,\text{ex}}\ _{L^2(0, T_{\max}; \mathbf{L}^1(\Omega))}$	0.8701	0.8892	0.9626	1.0009	1.0447	1.1586
$\ \mathbf{V} - \mathbf{V}_{h,\text{ex}}\ _{L^2(0, T_{\max}; \mathbf{L}^1(\Omega))}$	0.8569	0.89552	0.93304	0.98439	1.0483	1.1598
$\ \mathbf{U} - \mathbf{U}_{h,\text{ex}}\ _{L^2(0, T_{\max}; \mathbf{H}^1(\Omega))}$	1.2061	1.3733	1.5646	1.7873	1.9971	2.2678
$\ \mathbf{V} - \mathbf{V}_{h,\text{ex}}\ _{L^2(0, T_{\max}; \mathbf{H}^1(\Omega))}$	1.7200	1.7851	1.8585	1.9582	2.0884	2.3142

Table 2.3: Results of estimated order of convergence with respect to time refinement.

From the results obtained we can infer that our semi-implicit method has an order of convergence to the exact solution with respect to Δt of at least 1 for all norms considered. We then can assume that we have a order of convergence comparable to explicit Euler method. On the other hand, we can expect improved numerical stability properties due to the semi-implicit treatment. A fully implicit method is expected to have a second order of convergence, but it would require to solve a nonlinear problem at every time-step, resulting in a large computational cost. Overall, we can deem our semi-implicit method a good compromise between the robustness of a fully implicit scheme and the efficiency of an explicit one.

2.3.4. Simulation of a single cells system

In this section we present one result obtained applying the one cell solver method to solve (2.33), imposing Set C of parameters of Table 2.1, therefore solving the original RD system (2.1) through the semi-implicit method described in Section 2.2.2. The initial active and inactive ROPs distribution was settled constant homogeneous:

$$\mathbf{U}^0 = 0.9, \quad \mathbf{V}^0 = 1.0$$

as shown in Figure 2.7.

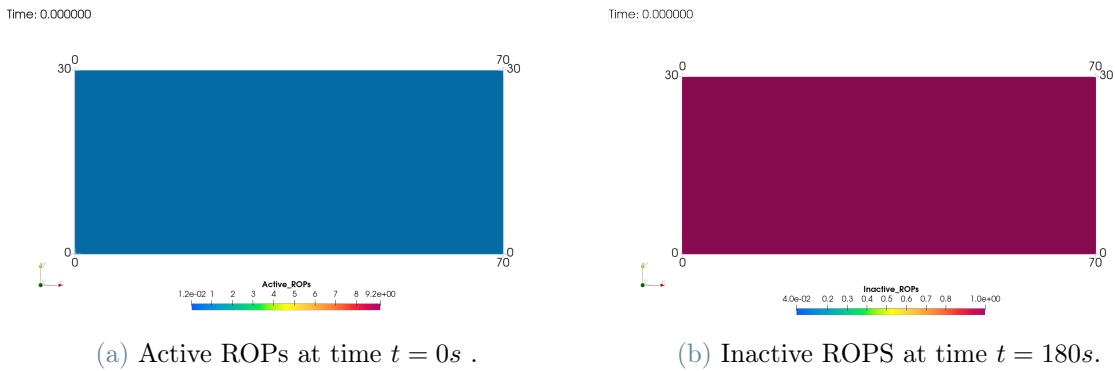
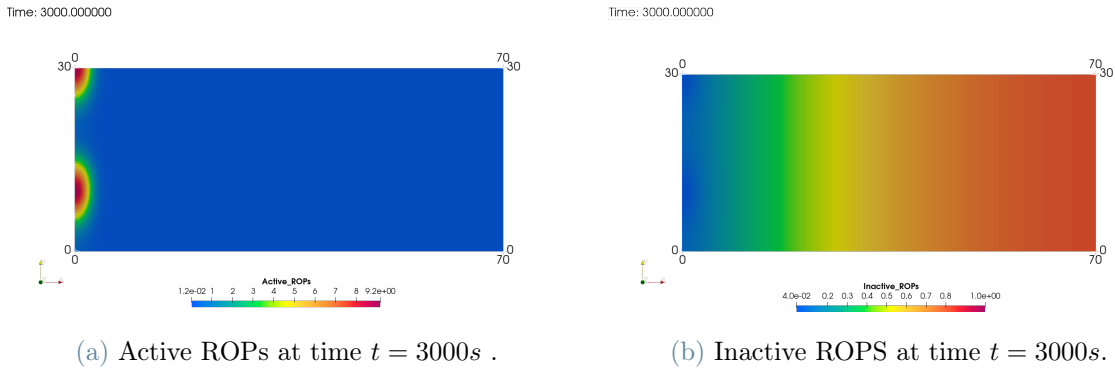
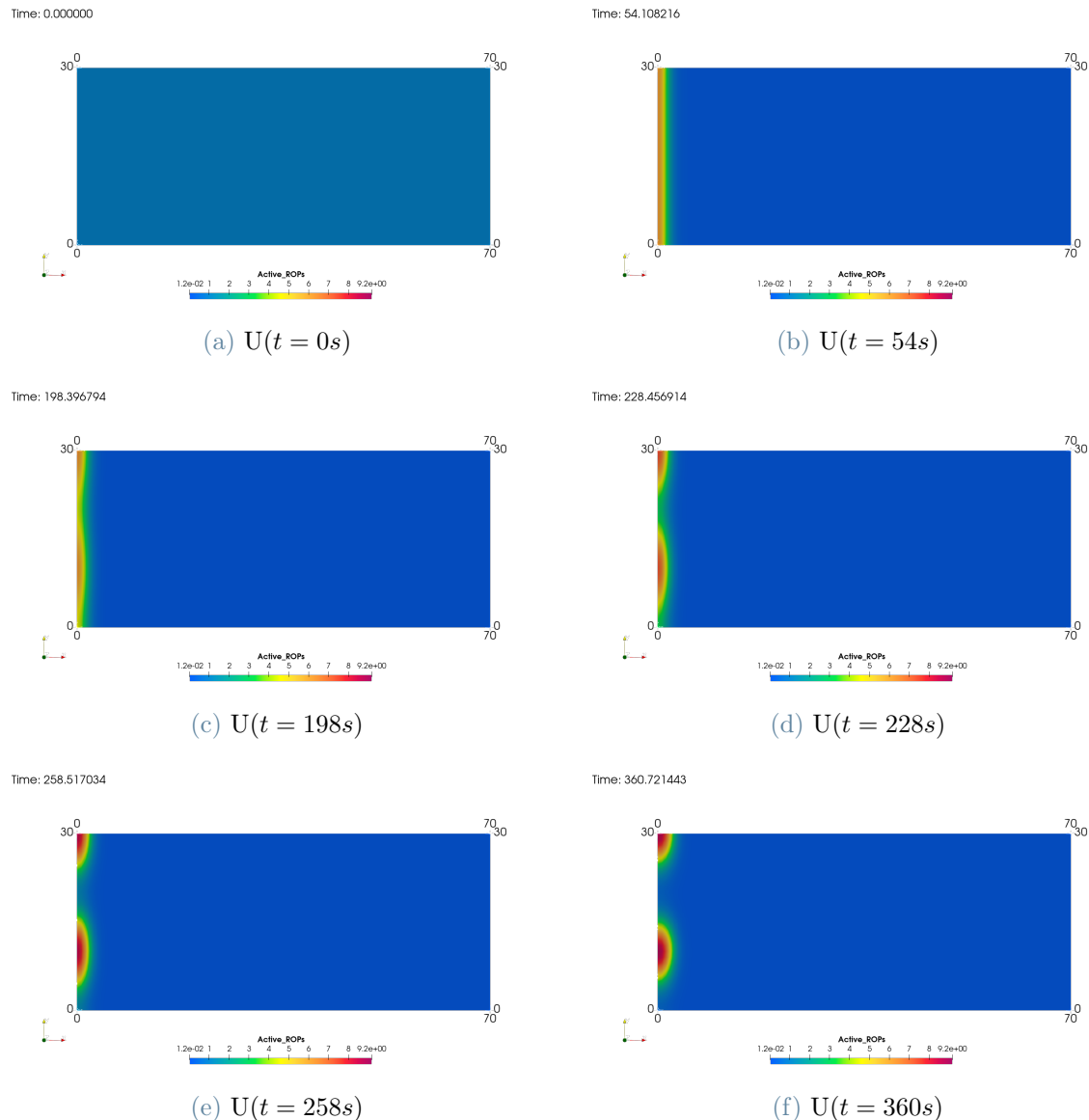


Figure 2.7: Constant homogeneous initialization for 1cell solver.

Figure 2.8: Solutions of the 1cell solver at final time $t = 3000s$.

The dynamical system for the spots was simulated up to final time $T_{max} = 3000s$, and in Figure 2.8 we show the solutions \mathbf{U} and \mathbf{V} obtained. Focusing the attention on the concentration of active ROPs in Figure 2.9, its evolution in time and space shows a typical patch formation. From the relevant snapshots, we see the formation of a homoclinic stripe along the left boundary, than it rapidly divides into spots and the system evolves to a steady-state composed by two spots.

Figure 2.9: Active ROPs u evolution for 1cell solver.

3 | Pattern formation in a pluricellular system

Previous studies on ROPs system focused the attention on one single cell only. Arabidopsis root is actually composed by a large number of cells and understanding how groups of cells communicate with one another during the development of multi-cellular organism acquires great importance. Moreover, one of the main factors influencing pattern formation is the hormone auxin, whose dynamics inside the cell is driven by communication between neighbouring cells and some of their (different) physical characteristics. For these reasons, extending the singular cell model into a pluricellular model is believed to lead to a more robust model, in order to better understand how the self-organized process of hair formation in the root epidermis happens. This work represents one of the first attempt on the topic, based on physical considerations and on other works on similar physical quantities as well as on modeling assumptions on the system.

In the first section we give a physical interpretation of the model under consideration, paying particular attention to the communication between neighboring cells and providing a physical meaning to the new parameters added to the ROPs system. We detail the numerical methods applied to the pluricellular model, developing an iterative algorithm inspired by a Robin-Robin Domain Decomposition (DD) method. To justify our implementation strategy, we also present a Robin-Robin DD method applied to a two cells system. Finally, we provide an extensive numerical assessment by applying the proposed model to different contexts in the result section. The first simulations serve as benchmark to tune all the new parameters added to the system, characterizing the communication channels between cells. Then, after the selection of a proper set of parameters, we validate the new method changing parameteres the ROPs activation and deactivation processes.

3.1. Physical model

We consider the root-hair cell projection onto a 2D rectangular domain as in Chapter 2. A system of four cells is schematically presented in Figure 3.1. We can see that each

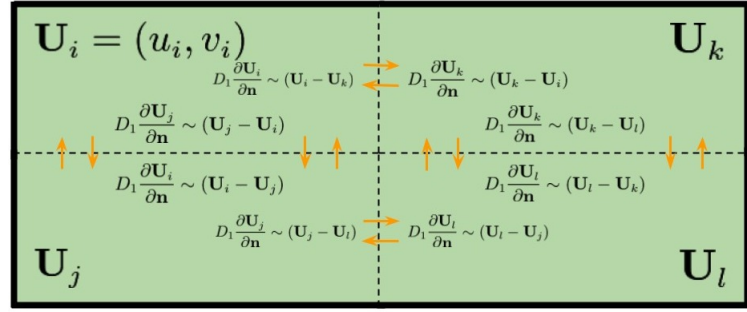


Figure 3.1: Sktetch of a four cells scheme with communicating flows.

cell has longitudinal and transverse boundaries in common with close cells. We recall the single cellular model, namely:

$$\begin{cases} \partial_t u = \tilde{D}_1 \Delta_s u + \tilde{a}_1 u + \tilde{b}_1 v + \tilde{c}_1 u^2 v & \text{in } \Omega \\ \partial_t v = \tilde{D}_2 \Delta_s v + \tilde{a}_2 v + \tilde{b}_2 u + \tilde{c}_2 u^2 v + f_2 & \text{in } \Omega \\ \tilde{D}_1 \nabla_s u \cdot \mathbf{n} = 0 & \text{on } \partial\Omega \\ \tilde{D}_2 \nabla_s v \cdot \mathbf{n} = 0 & \text{on } \partial\Omega. \end{cases} \quad (3.1)$$

No-flux on $\partial\Omega$, namely Neumann homogeneous boundary conditions, characterizes the system behaviour along the cell boundary. In the multi-cellular model, communication between cells is represented by allowed flux of ROPs, active and inactive, through localized channels along boundaries between neighboring cells.

We define as neighbor of cell Ω_i the set of cells with index in $\mathcal{N}_i = \{j : \partial\Omega_j \cap \partial\Omega_i \neq \emptyset\}$. The flux of concentration of active and inactive ROPs (u_i, v_i) is proportional to the difference of concentration (u_j, v_j) in neighbouring cells for $j \in \mathcal{N}_i$.

We formulate the new model still focusing on one single cell domain Ω_i , taking into account the new flux generated from the discrepancy of concentrations with the neighboring cells. The new flux results in adding a non-homogeneous Neumann boundary condition on the common interfaces, as follows:

$$\begin{cases} \partial_t u_i = \tilde{D}_1 \Delta_s u_i + \tilde{a}_1 u_i + \tilde{b}_1 v_i + \tilde{c}_1 (u_i)^2 v_i & \text{in } \Omega_i \\ \partial_t v_i = \tilde{D}_2 \Delta_s v_i + \tilde{a}_2 v_i + \tilde{b}_2 u_i + \tilde{c}_2 (u_i)^2 v_i + f_2 & \text{in } \Omega_i \\ \tilde{D}_1 \nabla_s u_i \cdot \mathbf{n} = 0 & \text{on } \partial\Omega_i \setminus \cup_{j \in \mathcal{N}_i} \Gamma_{j,i} \\ \tilde{D}_2 \nabla_s v_i \cdot \mathbf{n} = 0 & \text{on } \partial\Omega_i \setminus \cup_{j \in \mathcal{N}_i} \Gamma_{j,i} \\ \tilde{D}_1 \nabla_s u_i \cdot \mathbf{n} = \beta_{uRR} \alpha_{uRR} (u_j - u_i) & \text{on } \Gamma_{j,i} \forall j \in \mathcal{N}_i \\ \tilde{D}_2 \nabla_s v_i \cdot \mathbf{n} = \beta_{vRR} \alpha_{vRR} (v_j - v_i) & \text{on } \Gamma_{j,i} \forall j \in \mathcal{N}_i, \end{cases} \quad (3.2)$$

where we define as (u_i, v_i) the concentrations of active and inactive ROPs restricted to cell Ω_i : $(u_i, v_i) : \Omega_i \times (0, T_{max}) \rightarrow \mathbb{R}^2$ and $\Gamma_{j,i}$ represents the common side between cell Ω_i and cell $\Omega_j \in \mathcal{N}_i$, therefore defined as: $\Gamma_{j,i} = \partial\Omega_i \cap \partial\Omega_j$.

Each of the neighboring cells follows the same model for hair formation, meaning that system in (3.2) holds $\forall i$ cells composing the pluricellular system. As a consequence, the newly defined boundary conditions is coupled with the solutions (u_j, v_j) with $j \in \mathcal{N}_i$. Therefore, the pluricellular system requires a proper iterative method for setting correctly boundary conditions depending on solutions in the neighboring cells.

Not communicating with other RH cells boundaries have as before no-flux. The new boundary conditions are characterized by a function and a coefficient for both active active ROPs u and inactive ROPs v , having the same meaning:

- $\beta_{u/vRR}$ [$\frac{1}{\mu m^2}$] are indicator functions defined on boundaries of cells, equal to 1 where the communicating channels are open and 0 where no-flux is assumed;
- $\alpha_{u/vRR}$ [$\frac{1}{\mu m}$] are transport efficiency coefficients, representing a sort of flux quantity allowed through channels.

These channel parameters aim at representing the average active transport along the sides of confining cells, set equal to the flux of proteins from one cell to the neighbouring ones.

We have no physical insight on previously cited functions modeling open channels for ROPs. A whole set of simulations for the proper tuning of parameters is required, in order to find a sufficiently plausible setting of the system.

3.2. Numerical treatment

The communication between cells requires a proper iterative algorithm in order to deal with the mutual interplay between confining cells.

Every subdomain Ω_i of the pluricellular system Ω represents the single cell and the original system of equations in (2.6) is solved in Ω_i for all $i = 1, \dots, N$. We solve such systems by means of the semi-implicit method described in Section 2.2.2. Let us consider the weak formulation restricted to Ω_i , defining the functional space $V_i = \{w_i \in H^1(\Omega_i)\}$, the finite element subspace $V_{i,h} \subset V_i$ and the time interval discretization used in Section 2.2.2. In particular, we divide the time interval $[0, T_{max}]$ in N_{max} time steps such that $t^n = n\Delta t$ with $\Delta t = T_{max}/N_{max}$. We rewrite the full discretized formulation, identifying $u_{i,h}$ with $u_h|_{\Omega_i}$, as:

given the initial state $(u_{i,h}^0, v_{i,h}^0)$, find $(u_{i,h}^{n+1}, v_{i,h}^{n+1}) \in V_{i,h} \times V_{i,h}$ such that

$$\begin{cases} a_{i,u}(u_{i,h}^{n+1}, w_{i,h}) + b_{i,u}(v_{i,h}^{n+1}, w_{i,h}) + c_{i,u}(v_{i,h}^{n+1}, w_{i,h}) = f_{i,u}(w_{i,h}) \quad \forall w_{i,h} \in V_{i,h} \\ a_{i,v}(v_{i,h}^{n+1}, w_{i,h}) + b_{i,v}(u_{i,h}^{n+1}, w_{i,h}) + c_{i,v}(v_{i,h}^{n+1}, w_{i,h}) = f_{i,v}(w_{i,h}) \quad \forall w_{i,h} \in V_{i,h}, \end{cases} \quad (3.3)$$

$\forall n = 0, \dots, N_{max}$, where

$$\begin{aligned} a_{i,u}(u_{i,h}^{n+1}, w_{i,h}) &= \int_{\Omega_i} \left(\frac{1}{\Delta t} u_{i,h}^{n+1} w_{i,h} + \tilde{D}_1 \nabla_s u_{i,h}^{n+1} \cdot w_{i,h} - \tilde{a}_1 u_i^{n+1} w_{i,h} \right) \\ &\quad - \int_{\partial\Omega_i} \left(\tilde{D}_1 \nabla_s u_{i,h}^{n+1} \cdot \mathbf{n} w_{i,h} \right) \end{aligned} \quad (3.4a)$$

$$b_{i,u}(v_{i,h}^{n+1}, w_{i,h}) = \int_{\Omega_i} \left(-\tilde{b}_1 v_{i,h} w_{i,h} \right) \quad (3.4b)$$

$$c_{i,u}(v_{i,h}^{n+1}, w_{i,h}) = \int_{\Omega_i} \left(-\tilde{c}_1 (u_{i,h}^n)^2 v_{i,h}^{n+1} w_{i,h} \right) \quad (3.4c)$$

$$\begin{aligned} a_{i,v}(v_{i,h}^{n+1}, w_{i,h}) &= \int_{\Omega_i} \left(\frac{1}{\Delta t} v_{i,h}^{n+1} w_{i,h} + \tilde{D}_2 \nabla_s v_{i,h}^{n+1} \cdot w_{i,h} - \tilde{a}_2 v_i^{n+1} w_{i,h} \right) \\ &\quad - \int_{\partial\Omega_i} \left(\tilde{D}_2 \nabla_s v_{i,h}^{n+1} \cdot \mathbf{n} w_{i,h} \right) \end{aligned} \quad (3.4d)$$

$$b_{i,v}(v_{i,h}^{n+1}, w_{i,h}) = \int_{\Omega_i} \left(-\tilde{b}_2 u_{i,h} w_{i,h} \right) \quad (3.4e)$$

$$c_{i,v}(v_{i,h}^{n+1}, w_{i,h}) = \int_{\Omega_i} \left(-\tilde{c}_2 (u_{i,h}^n)^2 v_{i,h}^{n+1} w_{i,h} \right) \quad (3.4f)$$

$$f_{i,u}(w_{i,h}) = \int_{\Omega_i} \left(\frac{1}{\Delta t} u_{i,h}^n w_{i,h} \right) \quad (3.4g)$$

$$f_{i,v}(w_{i,h}) = \int_{\Omega} \left(\frac{1}{\Delta t} v_{i,h}^n w_{i,h} + f_2 w_{i,h} \right). \quad (3.4h)$$

The introduction of different boundary conditions will require to modify the bilinear forms (3.4a) and (3.4d) and to add contributions in the right hand sides (3.4g) and (3.4h).

To this aim, we synthetically rewrite the model problem (3.3), assuming generic boundary conditions, through a linear operator \mathcal{L} in the following way:

Given the initial state (u_i^0, v_i^0) , find $(u_i^{n+1}, v_i^{n+1}) \in \Omega_i$ such that:

$$\mathcal{L}^n(u_i^{n+1}, v_i^{n+1}) = \mathbf{f}^n \text{ in } \Omega_i \quad (3.5)$$

$\forall n = 0, \dots, N_{max}$.

3.2.1. The domain decomposition method

We briefly recall the domain decompostion method [37], one of the main mathematical tools used to solve boundary value problems into different subdomains, belonging or not to different physics. The domain decomposition method is based on partitioning the computational domain into subdomains, with or without overlapping parts, and introducing transmission conditions at common interfaces. The division of the domain can be driven by physical reason, e.g., one part of the domain is characterized by a different physical model than the other, such as in fluid-structure interaction problems [3, 16]; or it can be driven by optimization reasons, e.g, it could be easier to solve the same problem in more geometrically regular subdomains with respect in the original one, characterized instead by a non-standard shape.

To understand the general procedure of the domain decompostion method, we consider a general differential problem of the form:

$$\mathcal{L}u = f \text{ in } \Omega, \quad (3.6)$$

where \mathcal{L} is a partial differential operator, f is a given datum and u is the unknown function. We partition the domain Ω into two disjoint domains Ω_1 and Ω_2 and we denote as Γ the common boundary. Denoting by u_i the restriction of u to Ω_i for $i = 1, 2$, it follows that:

$$\begin{aligned} \mathcal{L}u_1 &= f \text{ in } \Omega_1 \\ \mathcal{L}u_2 &= f \text{ in } \Omega_2. \end{aligned} \quad (3.7)$$

In order to guarantee the exact equivalence with (3.6), we need to enforce transmission conditions between u_1 and u_2 across Γ . Depending on the physical problem under analysis, the usual conditions to impose are the continuity of the solutions and the continuity of normal fluxes (normal stress) at the boundaries [37]:

$$u_1 = u_2 \text{ on } \Gamma \quad (3.8)$$

$$\frac{\partial u_1}{\partial n_L} = \frac{\partial u_2}{\partial n_L} \text{ on } \Gamma, \quad (3.9)$$

with normal derivative in (3.9) defined by the differential problem under analysis.

Then, one may solve the multi-domain problem by iterative procedures. To this aim, we introduce a sequence of subproblems in Ω_1 and Ω_2 so that the two transmission conditions provide a Dirichlet (3.8) or a Neumann (3.9) boundary condition to impose on the internal boundary Γ . The assignment of the coupling conditions at the common interface

is the key part of the domain decomposition method used. Indeed, for example, we distinguish Dirichlet-Neumann (DN) method, where continuity of solutions (3.8) is imposed in the subproblem on Ω_1 and continuity of fluxes (3.9) on Ω_2 , while Neumann-Dirichlet (ND) method consists in the opposite impositions. In general, two sequence of functions $\{u_1^k\}, \{u_2^k\}$ are generated starting from a initial guess $\{u_1^0\}, \{u_2^0\}$ which will converge to u_1 and u_2 , respectively. At convergence the solution is equivalent to the one obtained solving the monolithic system, with guaranteed continuity of solutions and normal stress at the common interface.

One class of iterative procedures among domain decompostion methods which is of big interest for the model we are interested in is the Robin-Robin (RR) method. It is based on the Robin transmission conditions and generalizes the Dirichlet-Neumann approach. Robin boundary conditon is a linear combination of interface conditions (3.8) and (3.9), with positive coefficients α_1, α_2 characterizing the RR scheme as follows:

$$\begin{aligned} \frac{\partial u_1}{\partial n_L} + \alpha_1 u_1 &= \frac{\partial u_2}{\partial n_L} + \alpha_1 u_2 \text{ on } \Gamma \\ \frac{\partial u_2}{\partial n_L} + \alpha_2 u_2 &= \frac{\partial u_1}{\partial n_L} + \alpha_2 u_1 \text{ on } \Gamma. \end{aligned} \quad (3.10)$$

At convergence of sequence $\{u_1^k\}, \{u_2^k\}$, a solution is found, equivalent to u_1 and u_2 respectively, continuous at the interface and with same fluxes on Γ .

The RR family of partitioned procedure has been introduced with the aim of getting better convergence properties than with the DN or ND classical schemes. The velocity of convergence of RR method depends on the choice of coefficients α_1, α_2 . Setting α_1 and α_2 properly one can recover DN and ND (for example, setting $\alpha_1 = 0$ and $\alpha_2 = \infty$ leads to Neumann-Dirichlet method). One main issue is thus the identification of suitable combinations of parameters α_1, α_2 to improve the convergence properties of the classical DN scheme [17, 21]. We decided not to focus on the choice of this parameters, since classic Robin-Robin method was chosen only as a reference method for the implementation of a new model and we are not interested in optimizing its implementation. In the next subsection we present the RR algorithm for the boundary value problem (3.5).

3.2.2. Classic Robin-Robin algorithm

We take as reference method a classic domain decomposition algorithm with Robin boundary conditions. Focusing on a pluricellular system composed by two cells, the whole domain Ω is naturally partitioned into the two non-overlapping subdomains, corresponding to the two cells Ω_1 and Ω_2 , with a common interface Γ ; inside each sub-domain the model

problem (3.5) is solved with no-flux boundary condition on the external boundaries and, differently from the multi-cellular model in (3.2), free-flux and continuity of the solutions in the two domains is assumed on the common side. The two interface conditions are identified by two Robin type boundary conditions on Γ , one for each sub-domain. We refer to $\alpha_{u/vRR}$ as coefficient characterizing Robin boundary data. The n notation implies the solution is evaluated at time step $t^n = n\Delta t$, whereas k notation indicates the iteration of the iterative method. Robin-Robin domain decomposition algorithm is solved at every time-step and is formulated as follows:

given the initial concentrations (u_1^0, v_1^0) and (u_2^0, v_2^0) , at the n -th time step, find $(u_i^{n+1}, v_i^{n+1}) \in V_{i,h} \forall i = 1, 2$ such that solve the iterative method:

$$\begin{cases} \mathcal{L}^n(u_1^{k+1}, v_1^{k+1}) = \mathbf{f}^n \text{ in } \Omega_1 \\ \tilde{D}_1 \nabla_s u_1^{k+1} \cdot \mathbf{n} = 0 \text{ on } \partial\Omega_1 \setminus \Gamma \\ \alpha_{uRR} u_1^{k+1} + \tilde{D}_1 \frac{\partial u_1^{k+1}}{\partial \mathbf{n}} = \alpha_{uRR} u_2^k + \tilde{D}_1 \frac{\partial u_2^k}{\partial \mathbf{n}} \text{ on } \Gamma \\ \tilde{D}_2 \nabla_s v_1^{k+1} \cdot \mathbf{n} = 0 \text{ on } \partial\Omega_1 \setminus \Gamma \\ \alpha_{vRR} v_1^{k+1} + \tilde{D}_2 \frac{\partial v_1^{k+1}}{\partial \mathbf{n}} = \alpha_{vRR} v_2^k + \tilde{D}_2 \frac{\partial v_2^k}{\partial \mathbf{n}} \text{ on } \Gamma \end{cases} \quad (3.11)$$

$$\begin{cases} \mathcal{L}^n(u_2^{k+1}, v_2^{k+1}) = \mathbf{f}^n \text{ in } \Omega_2 \\ \tilde{D}_1 \nabla_s u_2^{k+1} \cdot \mathbf{n} = 0 \text{ on } \partial\Omega_2 \setminus \Gamma \\ \alpha_{uRR} u_2^{k+1} + \tilde{D}_1 \frac{\partial u_2^{k+1}}{\partial \mathbf{n}} = \alpha_{uRR} u_1^{k+1} + \tilde{D}_1 \frac{\partial u_1^{k+1}}{\partial \mathbf{n}} \text{ on } \Gamma \\ \tilde{D}_2 \nabla_s v_2^{k+1} \cdot \mathbf{n} = 0 \text{ on } \partial\Omega_2 \setminus \Gamma \\ \alpha_{vRR} v_2^{k+1} + \tilde{D}_2 \frac{\partial v_2^{k+1}}{\partial \mathbf{n}} = \alpha_{vRR} v_1^{k+1} + \tilde{D}_2 \frac{\partial v_1^{k+1}}{\partial \mathbf{n}} \text{ on } \Gamma \end{cases}$$

starting from $(u_2^{k=0}, v_2^{k=0}) = (u_1^n, v_1^n)$ for $k \geq 0$ until convergence and update $(u_i^{n+1}, v_i^{n+1}) = (u_i^{k+1}, v_i^{k+1})$.

The solution (u_i^{n+1}, v_i^{n+1}) is updated with the solution found at the end of the iterations. From now on, in order to simplify the notation, we refer to (u_i, v_i) as the unknowns (u_i^{k+1}, v_i^{k+1}) at each iteration and we omit the reference to the finite element space V_h .

Robin boundary conditions in the system modify the bilinear form characterizing the

Galerkin formulation. In particular, (3.4a) and (3.4d) become:

$$\begin{aligned}
a_{i,u}(u_i, w) &= \int_{\Omega_i} \left(\frac{1}{\Delta t} u_i w + \tilde{D}_1 \nabla_s u_i \cdot w - \tilde{a}_1 u_i w \right) - \int_{\partial\Omega_i} \left(\tilde{D}_1 \nabla_s u_i \cdot \mathbf{n} w \right) \\
&= \int_{\Omega_i} \left(\frac{1}{\Delta t} u_i w + \tilde{D}_1 \nabla_s u_i \cdot w - \tilde{a}_1 u_i w \right) - \int_{\Gamma} \left(\alpha_{uRR} u_j^k + \tilde{D}_1 \frac{\partial u_j^k}{\partial \mathbf{n}} - \alpha_{uRR} u_i \right) w \\
&= \int_{\Omega_i} \left(\frac{1}{\Delta t} u_i w + \tilde{D}_1 \nabla_s u_i \cdot w - \tilde{a}_1 u_i w \right) + \int_{\Gamma} (\alpha_{uRR} u_i w) - \int_{\Gamma} \left(\alpha_{uRR} u_j^k w + \tilde{D}_1 \frac{\partial u_j^k}{\partial \mathbf{n}} w \right) \\
&= \int_{\Omega_i} \left(\frac{1}{\Delta t} u_i w + \tilde{D}_1 \nabla_s u_i \cdot w - \tilde{a}_1 u_i w \right) + \int_{\Gamma} (\alpha_{uRR} u_i w) - \int_{\Gamma} (\alpha_{uRR} u_j^k w) \\
&\quad + (a_u(u_j, w) + b_u(v_j, w) + c_u(v_j, w) - f_u(w)), \\
a_{i,v}(v_i, w) &= \int_{\Omega_i} \left(\frac{1}{\Delta t} v_i w + \tilde{D}_2 \nabla_s v_i \cdot w - \tilde{a}_2 v_i w \right) - \int_{\partial\Omega_i} \left(\tilde{D}_2 \nabla_s v_i \cdot \mathbf{n} w \right) \\
&= \int_{\Omega_i} \left(\frac{1}{\Delta t} v_i w + \tilde{D}_2 \nabla_s v_i \cdot w - \tilde{a}_2 v_i w \right) - \int_{\Gamma} \left(\alpha_{vRR} v_j^k w + \tilde{D}_2 \frac{\partial v_j^k}{\partial \mathbf{n}} w - \alpha_{vRR} v_i w \right) \\
&= \int_{\Omega_i} \left(\frac{1}{\Delta t} v_i w + \tilde{D}_2 \nabla_s v_i \cdot w - \tilde{a}_2 v_i w \right) + \int_{\Gamma} (\alpha_{vRR} v_i w) - \int_{\Gamma} \left(\alpha_{vRR} v_j^k w + \tilde{D}_2 \frac{\partial v_j^k}{\partial \mathbf{n}} w \right) \\
&= \int_{\Omega_i} \left(\frac{1}{\Delta t} v_i w + \tilde{D}_2 \nabla_s v_i \cdot w - \tilde{a}_2 v_i w \right) + \int_{\Gamma} (\alpha_{vRR} v_i w) - \int_{\Gamma} (\alpha_{vRR} v_j^k w) \\
&\quad + (a_v(v_j, w) + b_v(u_j, w) + c_v(v_j, w) - f_v(w)).
\end{aligned}$$

In the last lines, the weak normal derivative of u_j and v_j are substituted with the residual from the proper combination of the bilinear forms on domain Ω_j [37]. As a consequence, we define new bilinear forms from (3.4a), (3.4d), (3.4g) and (3.4h) , adding Robin-Robin algorithm contribute as follows:

$$\begin{aligned}
a_{i,u}^{RR}(u_{i,h}^{k+1}, w_{i,h}) &= \int_{\Omega_i} \left(\frac{1}{\Delta t} u_{i,h}^{k+1} w_{i,h} + \tilde{D}_1 \nabla_s u_{i,h}^{k+1} \cdot w_{i,h} - \tilde{a}_1 u_{i,h}^{k+1} w_{i,h} \right) \\
&\quad + \int_{\Gamma} (\alpha_{uRR} u_{i,h}^{k+1} w_{i,h}) \\
&= a_{i,u}(u_{i,h}^{k+1}, w_{i,h}) + \int_{\Gamma} (\alpha_{uRR} u_{i,h}^{k+1} w_{i,h}), \\
a_{i,v}^{RR}(v_{i,h}^{k+1}, w_{i,h}) &= \int_{\Omega_i} \left(\frac{1}{\Delta t} v_{i,h}^{k+1} w_{i,h} + \tilde{D}_2 \nabla_s v_{i,h}^{k+1} \cdot w_{i,h} - \tilde{a}_2 v_{i,h}^{k+1} w_{i,h} \right) \\
&\quad + \int_{\Gamma} (\alpha_{vRR} v_{i,h}^{k+1} w_{i,h}) \\
&= a_{i,v}(v_{i,h}^{k+1}, w_{i,h}) + \int_{\Gamma} (\alpha_{vRR} v_{i,h}^{k+1} w_{i,h}),
\end{aligned} \tag{3.12}$$

$$\begin{aligned}
f_{i,u}^{RRc}(w_{i,h}) &= \int_{\Omega_i} \left(\frac{1}{\Delta t} u_{i,h}^n w_{i,h} \right) + \int_{\Gamma} (\alpha_{uRR} u_{j,h}^k w_{i,h}) + \int_{\Gamma} \tilde{D}_1 \frac{\partial u_j^k}{\partial n} w_{i,h} \\
&= f_{i,u}(w_{i,h}) + \int_{\Gamma} (\alpha_{uRR} u_{j,h}^k w_{i,h}) + \int_{\Gamma} \tilde{D}_1 \frac{\partial u_j^k}{\partial n} w_{i,h}, \\
f_{i,v}^{RRc}(w_{i,h}) &= \int_{\Omega} \left(\frac{1}{\Delta t} v_{i,h}^n w_{i,h} + f_2 w_{i,h} \right) + \int_{\Gamma} (\alpha_{vRR} v_{j,h}^k w_{i,h}) + \int_{\Gamma} \tilde{D}_2 \frac{\partial v_j^k}{\partial n} w_{i,h} \\
&= f_{i,v}(w_{i,h}) + \int_{\Gamma} (\alpha_{vRR} v_{j,h}^k w_{i,h}) + \int_{\Gamma} \tilde{D}_2 \frac{\partial v_j^k}{\partial n} w_{i,h},
\end{aligned} \tag{3.13}$$

implying that each weak normal derivative is computed in the residual form:

$$\begin{aligned}
\int_{\Gamma} \tilde{D}_1 \frac{\partial u_j^k}{\partial n} w_{j,h} &= (a_u(u_j^k, w_{j,h}) + b_u(v_j^k, w_{j,h}) + c_u(v_j^k, w_{j,h}) - f_u(w_{j,h})) , \\
\int_{\Gamma} \tilde{D}_2 \frac{\partial v_j^k}{\partial n} w_{j,h} &= (a_v(v_j^k, w_{j,h}) + b_v(u_j^k, w_{j,h}) + c_v(v_j^k, w_{j,h}) - f_v(w_{j,h})) .
\end{aligned} \tag{3.14}$$

We remark that in (3.14) test functions $w_{j,h}$ and variables contributing to the integral $u_{j,h}, v_{j,h}$ are defined in the finite element space $V_{j,h}$, whereas $f_{u,i}, f_{v,i}$ in (3.13) are linear functional of functions $w_{i,h} \in V_{i,h}$. The difficulty in dealing with variables from different functional spaces is solved through the use of a linear extension operator. We define $\mathcal{I}_{i,j}$ as the extension operator from finite element space $V_{i,h}$ to $V_{j,h}$: it extends by zero function from one space to the other. Formally then (3.13) is:

$$\begin{aligned}
f_{i,u}^{RRc}(w_{i,h}) &= f_{i,u}(w_{i,h}) + \int_{\Gamma} (\alpha_{uRR} \mathcal{I}_{i,j} u_{j,h}^k \mathcal{I}_{i,j} w_{j,h}) + (a_u(\mathcal{I}_{i,j} u_j^k, \mathcal{I}_{i,j} w_{j,h}) \\
&\quad + b_u(\mathcal{I}_{i,j} v_j^k, \mathcal{I}_{i,j} w_{j,h}) + c_u(\mathcal{I}_{i,j} v_j^k, \mathcal{I}_{i,j} w_{j,h}) - f_u(\mathcal{I}_{i,j} w_{j,h})) ,
\end{aligned} \tag{3.15}$$

$$\begin{aligned}
f_{i,v}^{RRc}(w_{i,h}) &= f_{i,v}(w_{i,h}) + \int_{\Gamma} (\alpha_{vRR} \mathcal{I}_{i,j} v_{j,h}^k \mathcal{I}_{i,j} w_{j,h}) + (a_v(v_j^k, \mathcal{I}_{i,j} w_{j,h}) \\
&\quad + b_v(u_j^k, \mathcal{I}_{i,j} w_{j,h}) + c_v(v_j^k, \mathcal{I}_{i,j} w_{j,h}) - f_v(\mathcal{I}_{i,j} w_{j,h})) .
\end{aligned} \tag{3.16}$$

We recover the algebraic formulation analogously as done in Section 2.2, being:

$$u_{i,h}^{k+1}(x, y) = \sum_{l=i}^{N_h} u_{i,l}^{k+1} \phi_l(x, y) , \quad v_{i,h}^{k+1}(x, y) = \sum_{l=i}^{N_h} v_{i,l}^{k+1} \phi_l(x, y), \tag{3.17}$$

We denote the corresponding vector of the finite element unknowns by $[\mathbf{U}_i^k, \mathbf{V}_i^k]$, being:

$$[\mathbf{U}_i^k]_l = u_{i,l}^k, \quad [\mathbf{V}_i^k]_l = v_{i,l}^k$$

. The RR iterative method in algebraic form for a 2 cells system is then:

given $\begin{bmatrix} \mathbf{U}_2^0 \\ \mathbf{V}_2^0 \end{bmatrix} = \begin{bmatrix} \mathbf{U}_2^n \\ \mathbf{V}_2^n \end{bmatrix}$, find $\begin{bmatrix} \mathbf{U}_1^{k+1} \\ \mathbf{V}_1^{k+1} \end{bmatrix}$ and $\begin{bmatrix} \mathbf{U}_2^{k+1} \\ \mathbf{V}_2^{k+1} \end{bmatrix}$ such that:

$$\begin{bmatrix} A_u^1 & B_u^1 + C_u^1(\mathbf{U}_1^n) \\ B_v^1 & A_v^1 + C_v^1(\mathbf{U}_1^n) \end{bmatrix} \begin{bmatrix} \mathbf{U}_1^{k+1} \\ \mathbf{V}_1^{k+1} \end{bmatrix} = \begin{bmatrix} F_u^1 \\ F_v^1 \end{bmatrix}, \quad \begin{bmatrix} A_u^2 & B_u^2 + C_u^2(\mathbf{U}_2^n) \\ B_v^2 & A_v^2 + C_v^2(\mathbf{U}_2^n) \end{bmatrix} \begin{bmatrix} \mathbf{U}_2^{k+1} \\ \mathbf{V}_2^{k+1} \end{bmatrix} = \begin{bmatrix} F_u^2 \\ F_v^2 \end{bmatrix} \quad (3.18)$$

for $k \geq 0$ up to convergence. Update

$$\begin{bmatrix} \mathbf{U}_1^{n+1} \\ \mathbf{V}_1^{n+1} \end{bmatrix} = \begin{bmatrix} \mathbf{U}_1^{k+1} \\ \mathbf{V}_1^{k+1} \end{bmatrix}, \quad \begin{bmatrix} \mathbf{U}_2^{n+1} \\ \mathbf{V}_2^{n+1} \end{bmatrix} = \begin{bmatrix} \mathbf{U}_2^{k+1} \\ \mathbf{V}_2^{k+1} \end{bmatrix}$$

Each sub-domain block matrix depends on the previous time-step solution, therefore it has to be reassembled at each time-step. The right-hand sides depend on the previous iteration because of the interface boundary condition and have to be reassembled at every iteration of the domain decomposition method. Matrices and vectors are defined using the previous bilinear forms in (3.12), (3.15) and (3.4).

Some contributions at the right-hand side come from solution variables and test functions not belonging to the same functional space of the correlated solution. Therefore we properly interpolate such terms from one space to the other.

3.2.3. A new iterative modeling algorithm

The model that we propose to make cells communicate can be regarded as a simplification of the classical domain decomposition scheme with Robin boundary conditions. We start for simplicity from a two cells problem and rewrite the common interface boundary conditions in (3.11) to recover the modelled open channels in (3.2). In the spirit of a

block-Gauss-Seidel algorithm, we solve in sequence:

$$\begin{cases} \mathcal{L}^n(u_1^{k+1}, v_1^{k+1}) = \mathbf{f}^n \text{ in } \Omega_1 \\ \tilde{D}_1 \nabla_s u_1^{k+1} \cdot \mathbf{n} = 0 \text{ on } \partial\Omega_1 \setminus \Gamma \\ \tilde{D}_1 \frac{\partial u_1^{k+1}}{\partial \mathbf{n}} = \alpha_{uRR} u_2^k - \alpha_{uRR} u_1^{k+1} \text{ on } \Gamma \\ \tilde{D}_2 \nabla_s v_1^{k+1} \cdot \mathbf{n} = 0 \text{ on } \partial\Omega_1 \setminus \Gamma \\ \tilde{D}_2 \frac{\partial v_1^{k+1}}{\partial \mathbf{n}} = \alpha_{vRR} v_2^k - \alpha_{vRR} v_1^{k+1} \text{ on } \Gamma \end{cases} \quad (3.19)$$

$$\begin{cases} \mathcal{L}^n(u_2^{k+1}, v_2^{k+1}) = \mathbf{f}^n \text{ in } \Omega_2 \\ \tilde{D}_1 \nabla_s u_2^{k+1} \cdot \mathbf{n} = 0 \text{ on } \partial\Omega_2 \setminus \Gamma \\ \tilde{D}_1 \frac{\partial u_2^{k+1}}{\partial \mathbf{n}} = \alpha_{uRR} u_1^{k+1} - \alpha_{uRR} u_2^{k+1} \text{ on } \Gamma \\ \tilde{D}_2 \nabla_s v_2^{k+1} \cdot \mathbf{n} = 0 \text{ on } \partial\Omega_2 \setminus \Gamma \\ \tilde{D}_2 \frac{\partial v_2^{k+1}}{\partial \mathbf{n}} = \alpha_{vRR} v_1^{k+1} - \alpha_{vRR} v_2^{k+1} \text{ on } \Gamma. \end{cases}$$

The flux imposed depends on the difference of the neighbouring solutions. As a consequence, we are imposing a not necessarily null Neumann boundary condition. Equation (3.19) defines a RR iterative method applied to two cells using proper parameters $\beta_{u/vRR}$ and $\alpha_{u/vRR}$ from the model formulated in Section 3.1:

starting from $(u_2^{k=0}, v_2^{k=0}) = (u_2^n, v_2^n)$, find $(u_1^{k+1}, v_1^{k+1}) \in V_1$ and $(u_2^{k+1}, v_2^{k+1}) \in V_2$:

$$\begin{cases} \mathcal{L}^n(u_1^{k+1}, v_1^{k+1}) = \mathbf{f}^n \text{ in } \Omega_1 \\ \tilde{D}_1 \nabla_s u_1^{k+1} \cdot \mathbf{n} = 0 \text{ on } \partial\Omega_1 \setminus \Gamma \\ \tilde{D}_1 \frac{\partial u_1^{k+1}}{\partial \mathbf{n}} = \beta_{uRR} \alpha_{uRR} (u_2^k - u_1^{k+1}) \text{ on } \Gamma \\ \tilde{D}_2 \nabla_s v_1^{k+1} \cdot \mathbf{n} = 0 \text{ on } \partial\Omega_1 \setminus \Gamma \\ \tilde{D}_2 \frac{\partial v_1^{k+1}}{\partial \mathbf{n}} = \beta_{vRR} \alpha_{vRR} (v_2^k - v_1^{k+1}) \text{ on } \Gamma \end{cases} \quad (3.20)$$

$$\begin{cases} \mathcal{L}^n(u_2^{k+1}, v_2^{k+1}) = \mathbf{f}^n \text{ in } \Omega_2 \\ \tilde{D}_1 \nabla_s u_2^{k+1} \cdot \mathbf{n} = 0 \text{ on } \partial\Omega_2 \setminus \Gamma \\ \tilde{D}_1 \frac{\partial u_2^{k+1}}{\partial \mathbf{n}} = \beta_{uRR} \alpha_{uRR} (u_1^{k+1} - u_2^{k+1}) \text{ on } \Gamma \\ \tilde{D}_2 \nabla_s v_2^{k+1} \cdot \mathbf{n} = 0 \text{ on } \partial\Omega_2 \setminus \Gamma \\ \tilde{D}_2 \frac{\partial v_2^{k+1}}{\partial \mathbf{n}} = \beta_{vRR} \alpha_{vRR} (v_1^{k+1} - v_2^{k+1}) \text{ on } \Gamma. \end{cases}$$

for $k \geq 0$ up to convergence.

We remark that in (3.20) the coefficients $\beta_{u/vRR}$ and $\alpha_{u/vRR}$ have physical meaning since they come from the model (3.2). This is in contrast with the model and method presented in Section 3.2.2, where the Robin coefficients are arbitrary.

Let $V_{i,h}$ denote the finite dimensional subspace of $H^1(\Omega_i)$, with Ω_i being the sub-domain of the pluricellular system Ω corresponding to cell. We find solutions $(u_h^{n+1}, v_h^{n+1})|_{\Omega_i}$ identified with $(u_{i,h}, v_{i,h}) \in V_{i,h}$ for each time step t^{n+1} , solving up to convergence the iteration step, whose Galerkin formulation is:

$$\begin{aligned} a_{i,u}^{RR}(u_{i,h}^{k+1}, w_{i,h}) + b_{i,u}(v_{i,h}^{k+1}, w_{i,h}) + c_{i,u}^n(v_{i,h}^{k+1}, w_{i,h}) &= f_{i,u}^{RR}(w_{i,h}) \quad \forall w_{i,h} \in V_{i,h} \\ a_{i,v}^{RR}(v_{i,h}^{k+1}, w_{i,h}) + b_{i,v}(u_{i,h}^{k+1}, w_{i,h}) + c_{i,v}^n(v_{i,h}^{k+1}, w_{i,h}) &= f_{i,v}^{RR}(w_{i,h}) \quad \forall w_{i,h} \in V_{i,h}. \end{aligned} \quad (3.21)$$

The bilinear forms used are equal to (3.4) - (3.12) for classic Robin-Robin algorithm. The only difference is in the right hand side (3.13) in which has been neglected the weak normal derivative of the neighbour solutions, as follows:

$$f_{i,u}^{RR}(w_{i,h}) = f_{i,u}(w_{i,h}) + \int_{\Gamma} (\beta_{uRR} \alpha_{uRR} \mathcal{I}_{i,j} u_{j,h}^k \mathcal{I}_{i,j} w_{j,h}), \quad (3.22)$$

$$f_{i,v}^{RR}(w_{i,h}) = f_{i,v}(w_{i,h}) + \int_{\Gamma} (\beta_{vRR} \alpha_{vRR} \mathcal{I}_{i,j} v_{j,h}^k \mathcal{I}_{i,j} w_{j,h}). \quad (3.23)$$

Consequently, the algebraic formulation of the new iterative method used is formulated similarly as in (3.18), with time-dependent block matrix that need to be reassembled at each time-step. The right-hand sides depend on the previous solution found for the neighbouring cells and their contributions need to be interpolated by means of a interpolation matrix as in Robin-Robin classic method. We here explicit the whole iterative method for a two cells composed system.

Starting from initial guess given by the previous time-step solution $\begin{bmatrix} \mathbf{U}_2^0 \\ \mathbf{V}_2^0 \end{bmatrix} = \begin{bmatrix} \mathbf{U}_2^n \\ \mathbf{V}_2^n \end{bmatrix}$, solve problem for $i = 1$ to find $\begin{bmatrix} \mathbf{U}_1^{k+1} \\ \mathbf{V}_1^{k+1} \end{bmatrix}$:

$$\begin{bmatrix} A_u^1 & B_u^1 + C_u^1(\mathbf{U}_1^n) \\ B_v^1 & A_v^1 + C_v^1(\mathbf{U}_1^n) \end{bmatrix} \begin{bmatrix} \mathbf{U}_1^{k+1} \\ \mathbf{V}_1^{k+1} \end{bmatrix} = \begin{bmatrix} F_u^1(\mathbf{U}_2^k) \\ F_v^1(\mathbf{V}_2^k) \end{bmatrix}$$

and then solve problem for $i = 2$ to find $\begin{bmatrix} \mathbf{U}_2^{k+1} \\ \mathbf{V}_2^{k+1} \end{bmatrix}$:

$$\begin{bmatrix} A_u^2 & B_u^2 + C_u^2(\mathbf{U}_2^n) \\ B_v^2 & A_v^2 + C_v^2(\mathbf{U}_2^n) \end{bmatrix} \begin{bmatrix} \mathbf{U}_2^{k+1} \\ \mathbf{V}_2^{k+1} \end{bmatrix} = \begin{bmatrix} F_u^2(\mathbf{U}_1^k) \\ F_v^2(\mathbf{V}_1^k) \end{bmatrix}$$

for $k \geq 0$ up to convergence.

Iterations end when the normalized residual of consecutive computed solutions is smaller than a proper tolerance or when a maximum number of iterations is performed and we update the new solution as:

$$\begin{bmatrix} \mathbf{U}_1^{n+1} \\ \mathbf{V}_1^{n+1} \end{bmatrix} = \begin{bmatrix} \mathbf{U}_1^{k+1} \\ \mathbf{V}_1^{k+1} \end{bmatrix}, \quad \begin{bmatrix} \mathbf{U}_2^{n+1} \\ \mathbf{V}_2^{n+1} \end{bmatrix} = \begin{bmatrix} \mathbf{U}_2^{k+1} \\ \mathbf{V}_2^{k+1} \end{bmatrix}$$

Matrices and vectors used are defined in the following way:

$$\begin{aligned} [A_u^i]_{j,l} &= a_{i,u}^{RR}(\phi_l, \phi_j), & [A_v^i]_{j,l} &= a_{i,v}^{RR}(\phi_l, \phi_j) \\ [B_u^i]_{j,l} &= b_{i,u}(\phi_l, \phi_j), & [B_v^i]_{j,l} &= b_{i,v}(\phi_l, \phi_j) \\ [C_u^i]_{j,l} &= c_{i,u}(\phi_l, \phi_j), & [C_v^i]_{j,l} &= c_{i,v}(\phi_l, \phi_j) \\ [F_u^i]_j &= f_{i,u}^{RR}(\phi_j), & [F_v^i]_j &= f_{i,v}^{RR}(\phi_j), \end{aligned} \tag{3.24}$$

being $\{\phi_l\}_{l=1}^{N_h}$ the functional basis of $V_{i,h}$ finite dimensional space defined on each cell Ω_i with $i = 1, 2$.

A sketch of the procedure to be adopted to deal with a generic N cells pluricellular system using Robin-Robin modified algorithm is schematically given in Algorithm 3.1; r_i are different coefficients characterizing initial state of concentrations, necessary for having flux between communicating cells. For physical reasons, we choose same initial guesses in the direction of the auxin gradient.

We have implemented a solver for a system of four cells.

As expressed in (3.20), the iterative procedure is formulated such that the pluricellular domain is solved sequentially, in the sense that the boundary conditions characterizing sub-domain i , depending on sub-domain solutions of $j \in \mathcal{N}_i$, are computed using the newly updated solutions. In view of a parallel implementation, the method can be reformulated such that the new boundary conditions are a function of the previous iteration solution.

In case we are solving a two cells system, when solving the boundary value problem in

Algorithm 3.1 Pluricellular system solver procedure: RR

Given $N \geq 1$ cells, r_i

```

1: Initialization:  $\forall i = 1, \dots, N$ 
2:  $[U_{0i}, V_{0i}] \leftarrow [r_i u_0, r_i v_0]$ 
3:  $[U_{iprec}, V_{iprec}] \leftarrow [U_{0i}, V_{0i}]$ 
4: while  $t < T_{max}$  do
5:   assemble matrix for  $\forall i = 1, \dots, N$ 
6:   for  $iter < N_{iter}$  do
7:      $\forall i = 1, \dots, N$ 
8:     compute BC contribute from  $j \in \mathcal{N}_i$ 
9:     interpolate on  $i$ 
10:    update rhs
11:    solve  $\Omega_i$  problem (3.2)
12:    update residual, check tolerance, update  $iter$ 
13:     $[U_{iprec}, V_{iprec}] \leftarrow [U_i, V_i]$ 
14:   end for
15:    $[U_{0i}, V_{0i}] \leftarrow [U_i, V_i]$ 
16: end while

```

Ω_2 at the new iteration $k + 1$, we use data on common interface Γ generated by $[U_1^k, V_1^k]$. Therefore two cells system problem (3.20) is reformulated in a block-Jacobi fashion as:

starting from $(u_2^{k=0}, v_2^{k=0}) = (u_2^n, v_2^n)$, find $(u_1^{k+1}, v_1^{k+1}) \in V_{1,h}$ and $(u_2^{k+1}, v_2^{k+1}) \in V_{2,h}$:

$$\begin{cases} \mathcal{L}^n(u_1^{k+1}, v_1^{k+1}) = \mathbf{f}^n \text{ in } \Omega_1 \\ \tilde{D}_1 \nabla_s u_1^{k+1} \cdot \mathbf{n} = 0 \text{ on } \partial\Omega_1 \setminus \Gamma \\ \tilde{D}_1 \cdot \partial u_1^{k+1} \partial \mathbf{n} = \beta_{uRR} \alpha_{uRR} (u_2^k - u_1^{k+1}) \text{ on } \Gamma \\ \tilde{D}_2 \nabla_s v_1^{k+1} \cdot \mathbf{n} = 0 \text{ on } \partial\Omega_1 \setminus \Gamma \\ \tilde{D}_2 \cdot \partial v_1^{k+1} \partial \mathbf{n} = \beta_{vRR} \alpha_{vRR} (v_2^k - v_1^{k+1}) \text{ on } \Gamma \\ \mathcal{L}^n(u_2^{k+1}, v_2^{k+1}) = \mathbf{f}^n \text{ in } \Omega_2 \\ \tilde{D}_1 \nabla_s u_2^{k+1} \cdot \mathbf{n} = 0 \text{ on } \partial\Omega_2 \setminus \Gamma \\ \tilde{D}_1 \cdot \partial u_2^{k+1} \partial \mathbf{n} = \beta_{uRR} \alpha_{uRR} (u_1^k - u_2^{k+1}) \text{ on } \Gamma \\ \tilde{D}_2 \nabla_s v_2^{k+1} \cdot \mathbf{n} = 0 \text{ on } \partial\Omega_2 \setminus \Gamma \\ \tilde{D}_2 \cdot \partial v_2^{k+1} \partial \mathbf{n} = \beta_{vRR} \alpha_{vRR} (v_1^k - v_2^{k+1}) \text{ on } \Gamma \end{cases} \quad (3.25)$$

for $k \geq 0$ up to convergence.

3.3. Numerical assessment

We here show some of the results obtained applying the iterative procedures in Section 3.2.3. At first we properly tune the parameters β_{uRR} , β_{vRR} and α_{uRR} , α_{vRR} characterizing the channels. Then, we underline the importance of a communication model to suitably simulate pluricellular systems through various results.

All simulations, if not differently stated, are solved under Table 2.1 - Set C of parameters and space dependent auxin distribution in (2.2). For a two cell system, Ω_1 corresponds to the lower cell and Ω_2 to the upper one. For a four cells system, the lower left cell is the first one and the other ones are numbered clockwise.

3.3.1. Stagnant cells reference solution

Since the multi-cellular model is a simplification of the actual physics governing the communication of cells, we provide a reference solution. This has a clear physical meaning of what happens between cells and pattern obtained can be compared with the different choices we did to model the presence of channels. In this way we can tune channel parameters and make considerations on the obtained result.

The reference solution is obtained solving the modified Robin-Robin algorithm, having channels of communication characterized by $\beta_{uRR} = \beta_{vRR} = 0$, which corresponds to no open channels between cells and therefore to a no-flux boundary condition between close cells. The two airtight, stagnant cells together with the time evolution of the concentrations of are visualized in Figure 3.2.

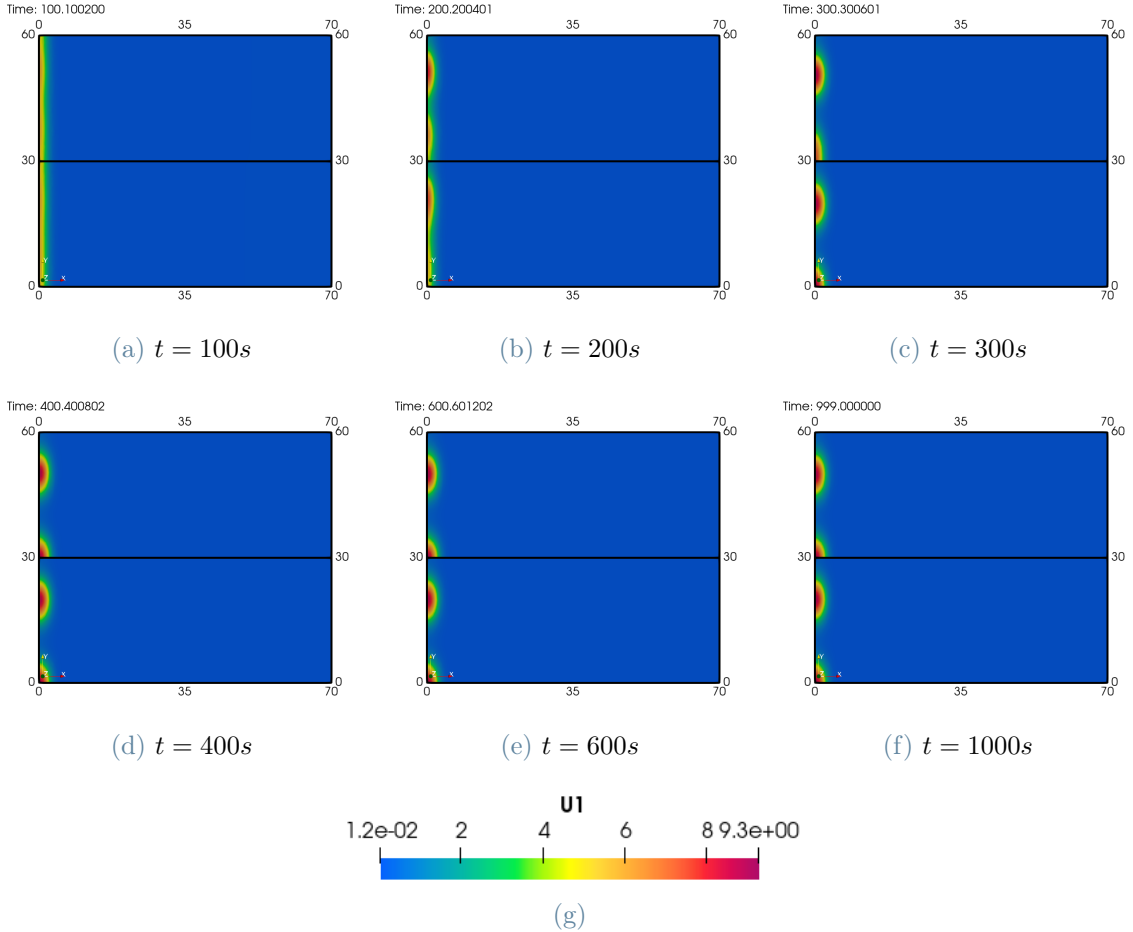


Figure 3.2: Active ROPs u evolution obtained with RR algorithm solver with $\beta_{uRR} = \beta_{vRR} = 0$.

We can observe that if there is no influence and communication between cells and spot formation is driven only by the gradient of auxin (2).

3.3.2. Tuning channels parameters

In this section, we illustrate different simulations in order to tune the parameters β_{uRR} , β_{vRR} and α_{uRR} , α_{vRR} used in (3.2). Setting properly the communication between cells is crucial for correctly simulating spot formation. In order to synthetically represent channels for a 2 cells system we rewrite β_{uRR} , β_{vRR} functions as follows:

$$\begin{aligned}\beta_{uRR} &= \mathbb{1}\left\{\frac{L_x}{2} - a_x - \epsilon_x \leq x \leq \frac{L_x}{2} - a_x\right\} + \mathbb{1}\left\{\frac{L_x}{2} + a_x \leq x \leq \frac{L_x}{2} + a_x + \epsilon_x\right\} \\ \beta_{vRR} &= \mathbb{1}\left\{\frac{L_x}{2} - a_x - \epsilon_x \leq x \leq \frac{L_x}{2} - a_x\right\} + \mathbb{1}\left\{\frac{L_x}{2} + a_x \leq x \leq \frac{L_x}{2} + a_x + \epsilon_x\right\},\end{aligned}\quad (3.26)$$

where $\mathbb{1}\{A\}$ is the characteristic function of a generic set A . We are assuming as reasonable that concentrations of active and inactive ROPs have the same channels of communication. The new introduced parameters have two different meanings:

- a_x is the distance at which two open channels are localized, symmetrically from the middle point of the side Γ .
- ϵ_x is the amplitude of the open channels.

We fixed $\epsilon_x = 1$ and $\alpha_{uRR} = \alpha_{vRR} = 1$ and let a_x vary. We choose as initial state of the concentrations

$$[U_1^0, V_1^0] = 1.5 [u^0, v^0], \quad [U_2^0, V_2^0] = [u^0, v^0]. \quad (3.27)$$

As a consequence, a sensitive difference in the sub-domains is expected and this may lead to non-null flux of ROPs thanks to the new boundary conditions defined in (3.20).

For $a_x = 5$ (Figure 3.3), $a_x = 20$ (Figure 3.4) and $a_x = 30$ (Figure 3.5) we do not observe sensitive difference with respect to the stagnant cells obtained with $\beta_{uRR} = \beta_{vRR} = 0$ in Figure 3.2; apart from the first few seconds, the patterns obtained are similar one to the other. We observe the formation of small spots from the breakup of an interior homoclinic stripe and how they evolve slowly in time to a steady-state two-spot pattern. The main responsible of the breakup of the stripe is assumed to be the auxin gradient, as stated and demonstrated through some analysis and numerical results in [14].

It is important to notice, as in previous works on singular cell system (see e.g.,[14]), that even if the problem is homogeneous along y direction, the system is not able to maintain the stability. The stripe formed is sensitive to a transverse instability since it is located close to the left-hand boundary, where the influence of the auxin gradient is stronger [14].

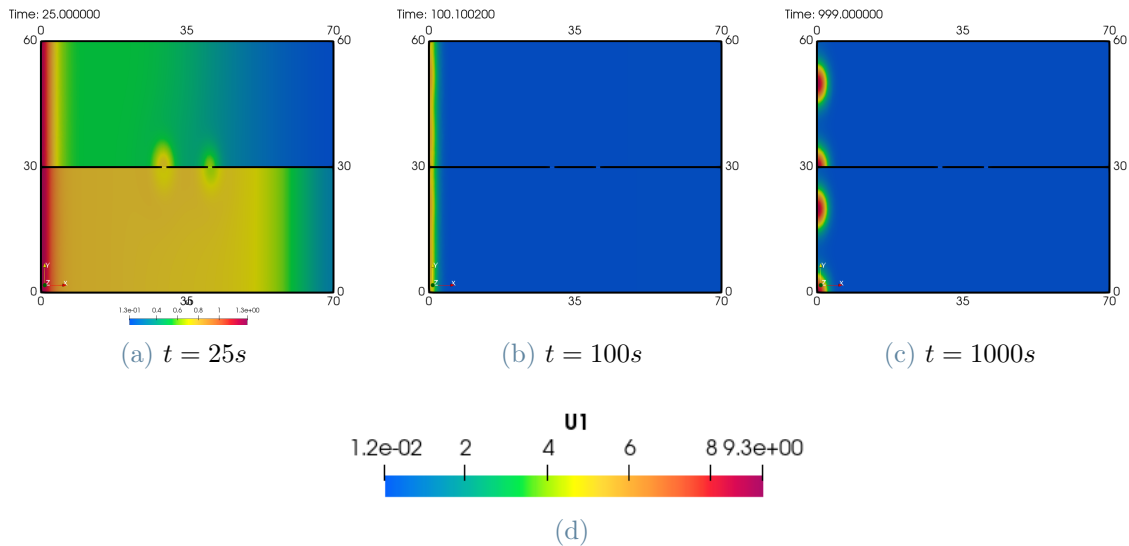


Figure 3.3: Active ROPs u evolution obtained with RR algorithm solver with $a_x = 5$.

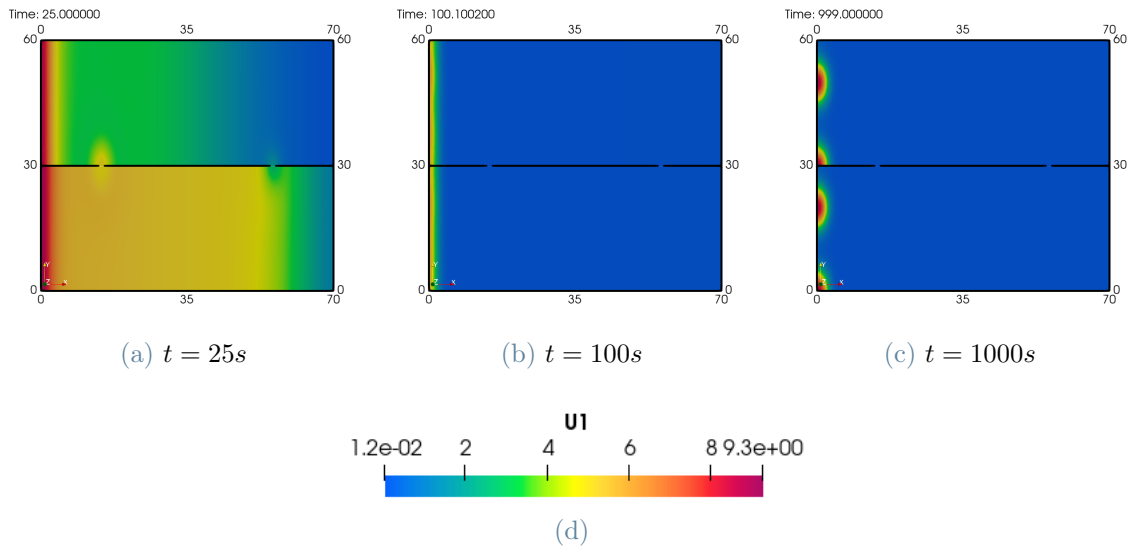


Figure 3.4: Active ROPs u evolution obtained with RR algorithm solver with $a_x = 20$.

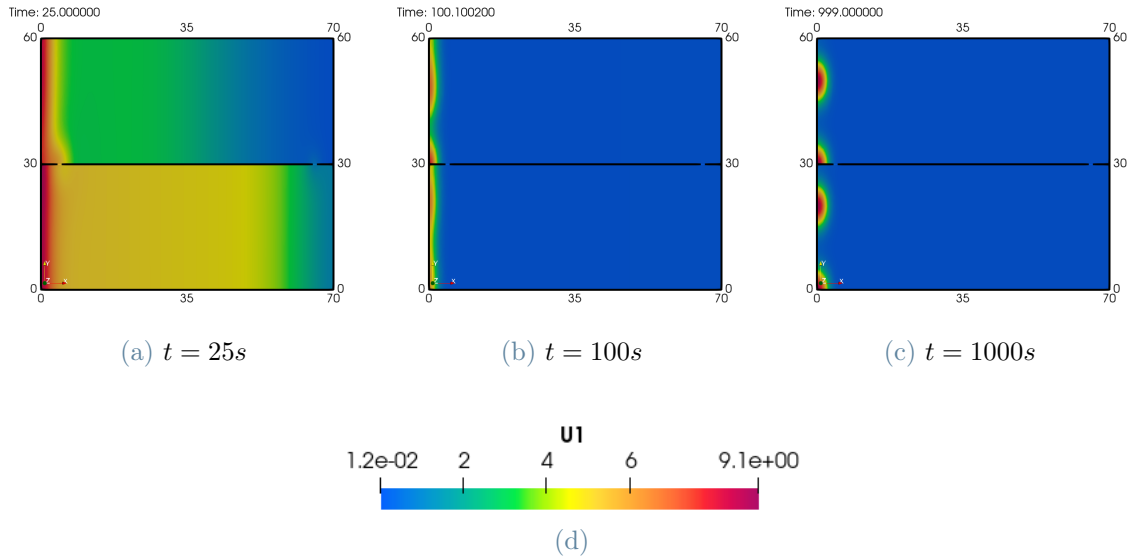


Figure 3.5: Active ROPs u evolution obtained with RR algorithm solver with $a_x = 30$.

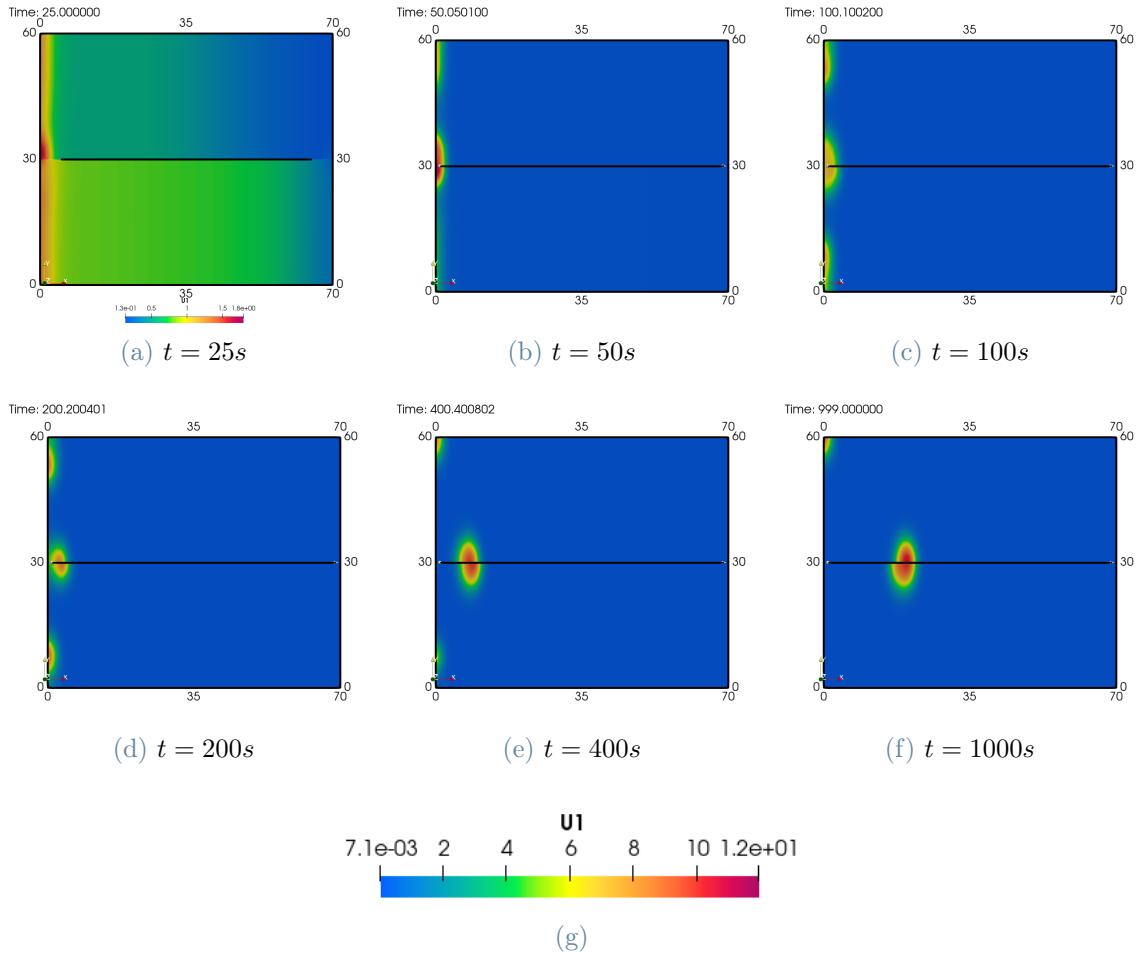


Figure 3.6: Active ROPs u evolution obtained with RR algorithm solver with $a_x = 34$.

Using instead $a_x = 34$, we observe a considerable difference in the evolution of spots (see Figure 3.6). Still a stripe-like state is formed at the boundary, but since the channel is located precisely where the stripe is formed, i.e., where the maximum of auxin is located, the homoclinic stripe collapses very soon and in a different way. The transverse dependence of solutions caused by the break up of the stripe leads to the generation of a flux of ROPs. The relevant flux of ROPs is placed where a channel is open and it let communication between cells to influence their dynamics. The system evolve to the formation of a unique spot moving to the right.

As a second test, we tested the sensitivity of the model with respect to the channel length, i.e., increasing ϵ_x , may cause a relevant change in results. Figure 3.7 shows few frames obtained with conditions:

- $\alpha_{RR} = 1$,
- initial state as in (3.27),
- $\epsilon_x = 5$, $a_x = 5$.

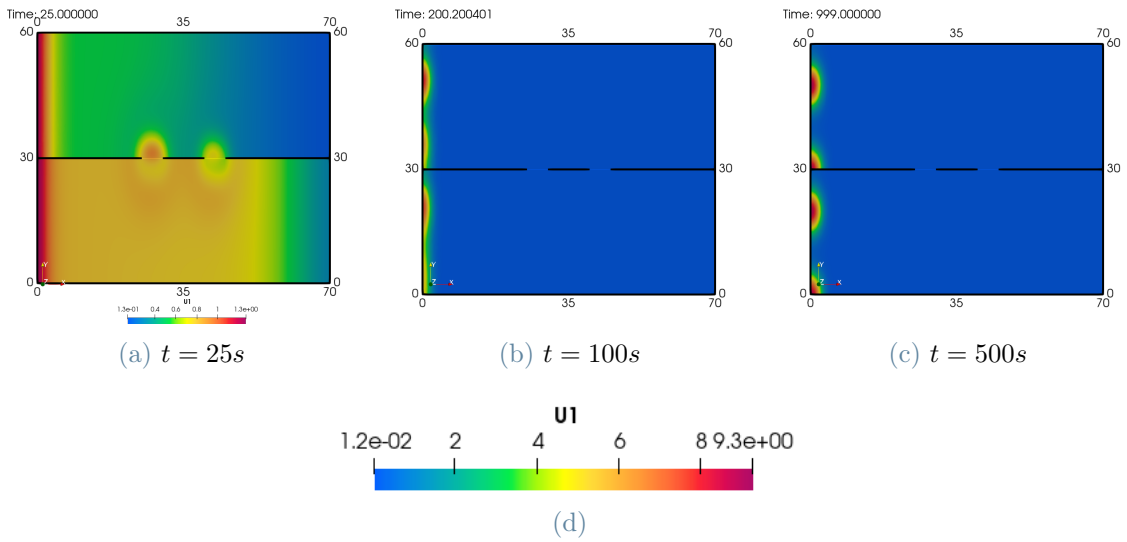


Figure 3.7: Active ROPs u evolution obtained with RR algorithm solver with $a_x = 5$, $\epsilon_x = 5$.

We do not observe relevant changes because channels are located too far from the area where auxin maximum is located and where therefore gradient has a relevant value.

Instead, by setting $\epsilon_x = 5$ and $a_x = 30$, the open channel covers the exact position in which the formation of the instabilities occurs (see Figure 3.8). Thus, we observe a non-

negligible flux of ROPs. Not being isolated, the two cells together form a common spot moving to the right.

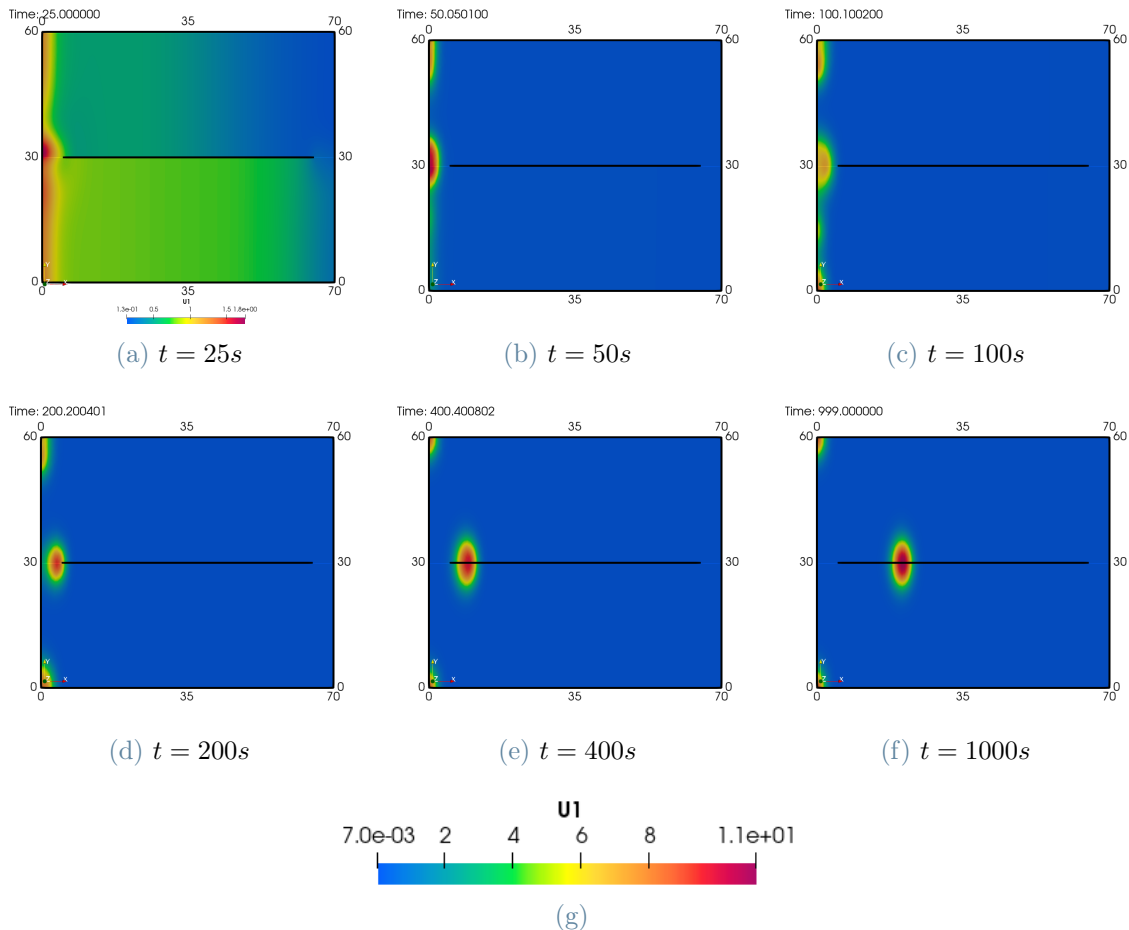


Figure 3.8: Active ROPs u evolution obtained with RR algorithm solver with $a_x = 30$, $\epsilon_x = 5$.

In Section 3.1 we explained that parameter α_{uRR} and α_{vRR} quantify the transport efficiency between cells. We show here how this coefficient is relevant and how different values affect the final solution. This parameter seems to be strictly related to the generation of patches away from the common interface and to guarantee a more similar behaviour between the two cells in location of high concentrations zone of ROPs. A smaller transport efficiency coefficient would cooperate less. Indeed, comparing simulation characterized by $\alpha_{uRR} = \alpha_{vRR} = 1$ found in Figure 3.6 with results in Figure 3.9 where $\alpha_{uRR} = \alpha_{vRR} = 35/2$, we observe a more symmetric spot formation in the second case.

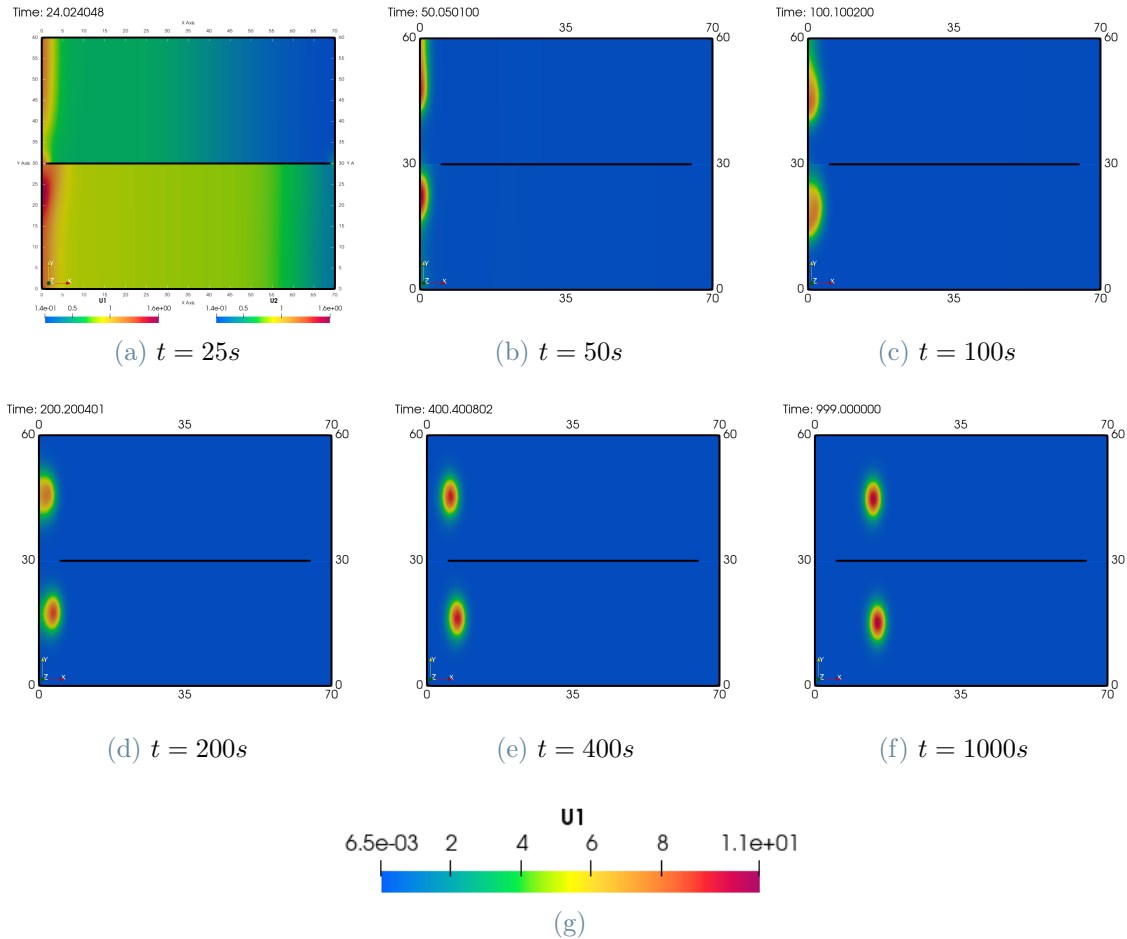


Figure 3.9: Active ROPs u evolution obtained with RR algorithm solver with $a_x = 34$, $\alpha_{RR} = \frac{35}{2}$.

open channels represented by functions (3.26) are a simplified representation of how channels of communications for ROPs are distributed. Indeed from a biological point of view, it is not really known where channels are located and what is the actual amplitude and frequency along the common side Γ . We could assume more realistic and precise channels, defined as follows:

$$\begin{aligned} \beta_{uRR} &= \mathbb{1}\{a_x \leq x \leq a_x + \epsilon_x\} + \mathbb{1}\{2a_x + \epsilon_x \leq x \leq 2a_x + 2\epsilon_x\} \\ &\quad + \mathbb{1}\{3a_x + 2\epsilon_x \leq x \leq 3a_x + 3\epsilon_x\} + \mathbb{1}\{4a_x + 3\epsilon_x \leq x \leq 4a_x + 4\epsilon_x\}. \\ \beta_{vRR} &= \mathbb{1}\{a_x \leq x \leq a_x + \epsilon_x\} + \mathbb{1}\{2a_x + \epsilon_x \leq x \leq 2a_x + 2\epsilon_x\} \\ &\quad + \mathbb{1}\{3a_x + 2\epsilon_x \leq x \leq 3a_x + 3\epsilon_x\} + \mathbb{1}\{4a_x + 3\epsilon_x \leq x \leq 4a_x + 4\epsilon_x\}. \end{aligned} \quad (3.28)$$

In Figure 3.10 we compare the solutions obtained with sparse channels, characterized by

$\epsilon_x = 1, a_x = 5$ and $\alpha_{uRR} = \alpha_{vRR} = 5/2$, against those obtained in Figure 3.8 with two single channels defined as in formula (3.26) with $\epsilon_x = 5, a_x = 30$.

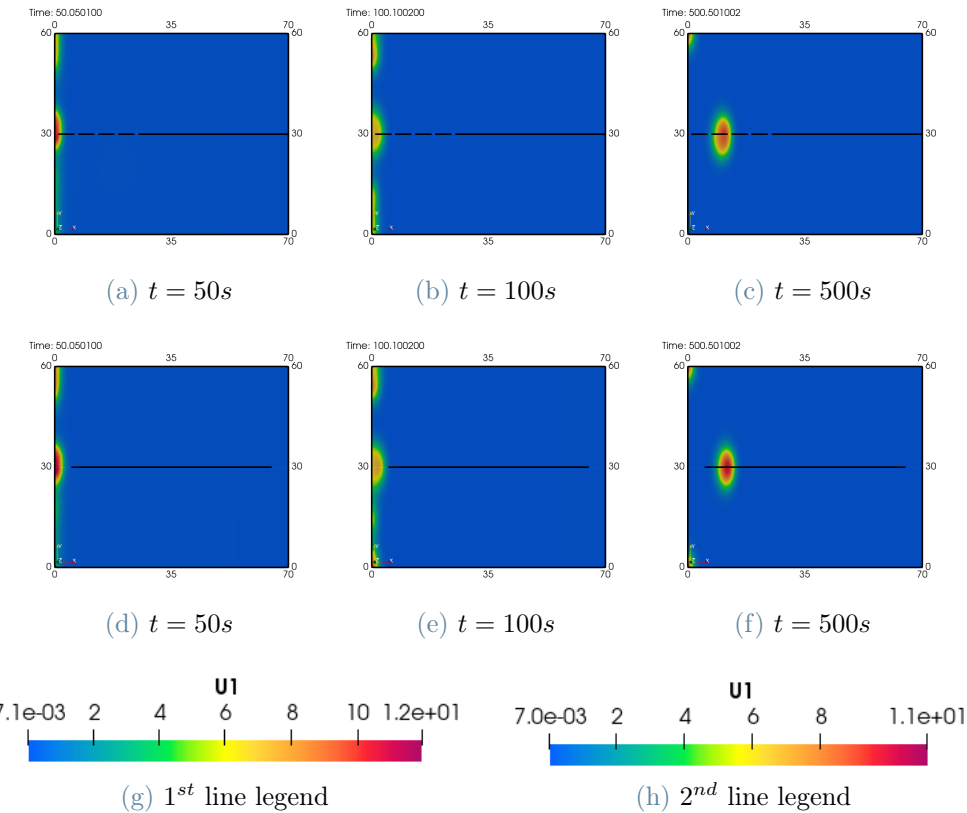


Figure 3.10: Active ROPs u evolution obtained with RR algorithm solver with smaller sparse channels on the top against Figure 3.8 channels on the bottom.

From this similar results we can infer that the simplified version of channels is a good approximation of the communication between cells and it is not necessary to have such precise functions β_{uRR} and β_{vRR} to obtain relevant contributions.

To sum up the considerations made on the proposed results, we point out that the most relevant information for channels definition is their location with respect to auxin distribution, maximum and gradient in particular. The amplitude of open channels ϵ_x seems less relevant in defining the evolution of the system. Finally, increasing α_{uRR} and α_{vRR} leads to a effective communication, thus yieldind symmetric patterning.

3.3.3. Parallelizable versus not-parallelizable mode

At the end of Section 3.2.3 we stated the difference between a parallelizable and a not-parallelizable algorithm. The two procedures differ also in terms of mathematical for-

mulation. We have implemented also the parallelized version of the proposed method. Actually, we observe, under same settings of parameters, considerably different solutions using the two different methods (see in Figure 3.11). In particular, the more relevant the open channels, i.e., the more close to the maximum of auxin, the more the simulations evolve in completely different ways. Indeed, even small numerical differences are propagated and amplified in time because of sensitivity of active dissipative system we deal with.

In Figure 3.11 ROPs system solved with the parallel mode (P) is shown in the first row, under parameters set C for ROPs and $a_x = 30$, $\epsilon_x = 5$, $\alpha_{uRR} = \alpha_{vRR} = 1$ for channels; the same system is solved with not parallel algorithm (NP) and the corresponding results are shown in the second row of Figure 3.11.

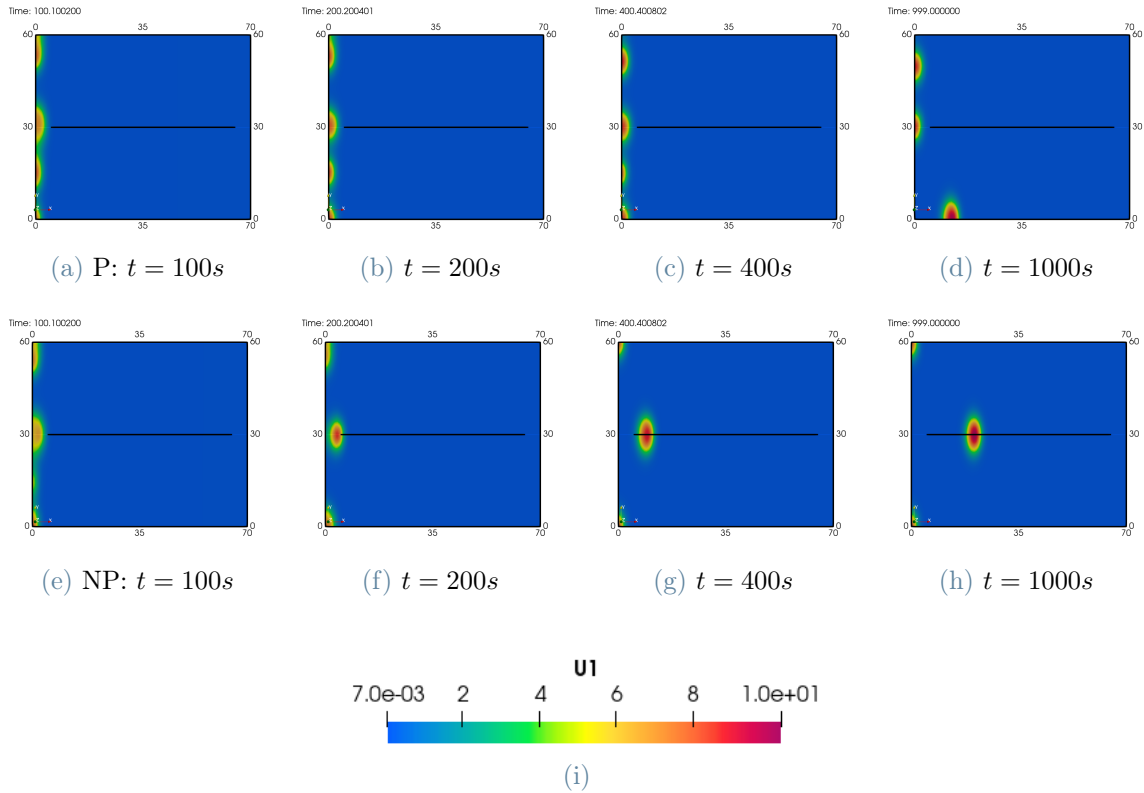


Figure 3.11: Active ROPs u solution with RR algorithm parallelizable against not-parallelizable mode, with relevant channel.

3.3.4. Overall auxin level k_{20}

The break-up instability for active ROPs spot under different values of the overall auxin level k_{20} was studied in other works. We have chosen to focus on the different values of k_{20}

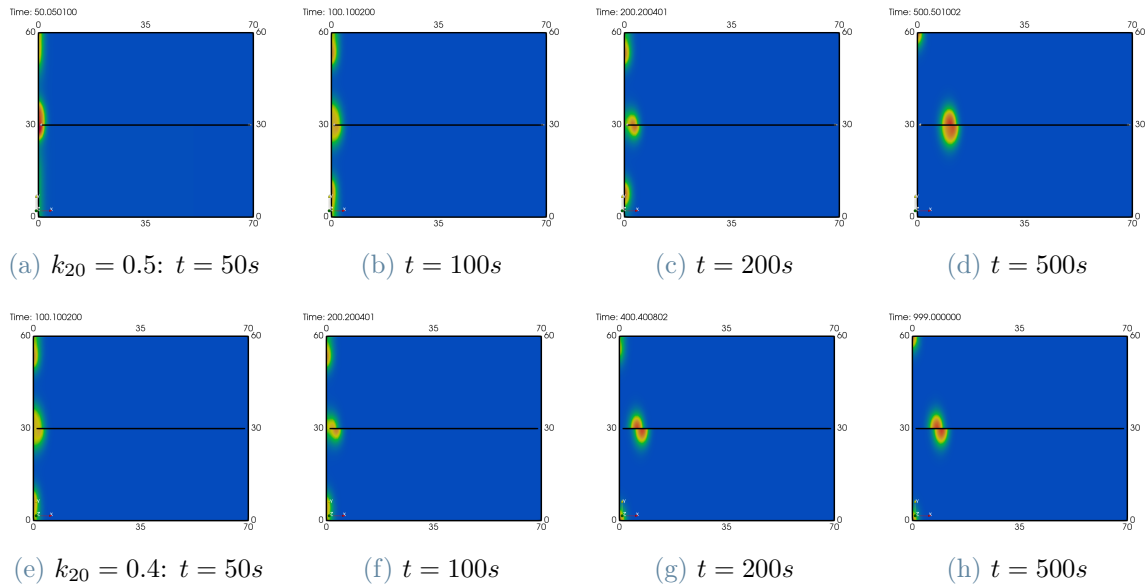


Figure 3.12: Active ROPs u evolution with RR algorithm solver with $k_{20} = 0.5$ (top row) and $k_{20} = 0.4$ (bottom row).

studied in [2, 14]. We prove how this parameter characterizing the system remains relevant to determine spot formation in a two cell system. The overall auxin level determined multiple-spot locations and showed instabilities. As a consequence, in previous works it was studied as a bifurcation parameter. The presented numerical simulations confirms this feature.

In Figure 3.12 we observe that a small change in the auxin level brings a considerable different spot formation. In this simulation we have settled $a_x = 34$ and $\epsilon_x = 1$.

Results shown in Figure 3.13 and 3.14 are obtained setting channels with $a_x = 30$ and $\epsilon_x = 5$; comparing the figures with Figure 3.8, we recognize the influence of auxin in spot formation and evolution. The more interesting feature is shown in Figure 3.14, where one can appreciate the advective power of auxin in transporting active ROPs spot. By considering a bigger value for k_{20} , the influence of the auxin gradient is stronger and this is demonstrated not only in the break-up of the initial stripe into multiple spots (as happened before), but also in the bending of the spot and subsequent breakup into a similar peanut-shaped spot.

Other interesting results are obtained starting from a non-homogeneous initial state, precisely from the spot obtained at final time $t = 1000s$ of Figure 3.6, with same channel setting, and changing k_{20} to 1.3562. This sudden change in the overall auxin level leads to the formation of bending spots and to the subsequent break-up in multiple spots, con-

siderably different from the evolution obtained for $k_{20} = 0.5$. The two evolutions are presented in Figure 3.15.

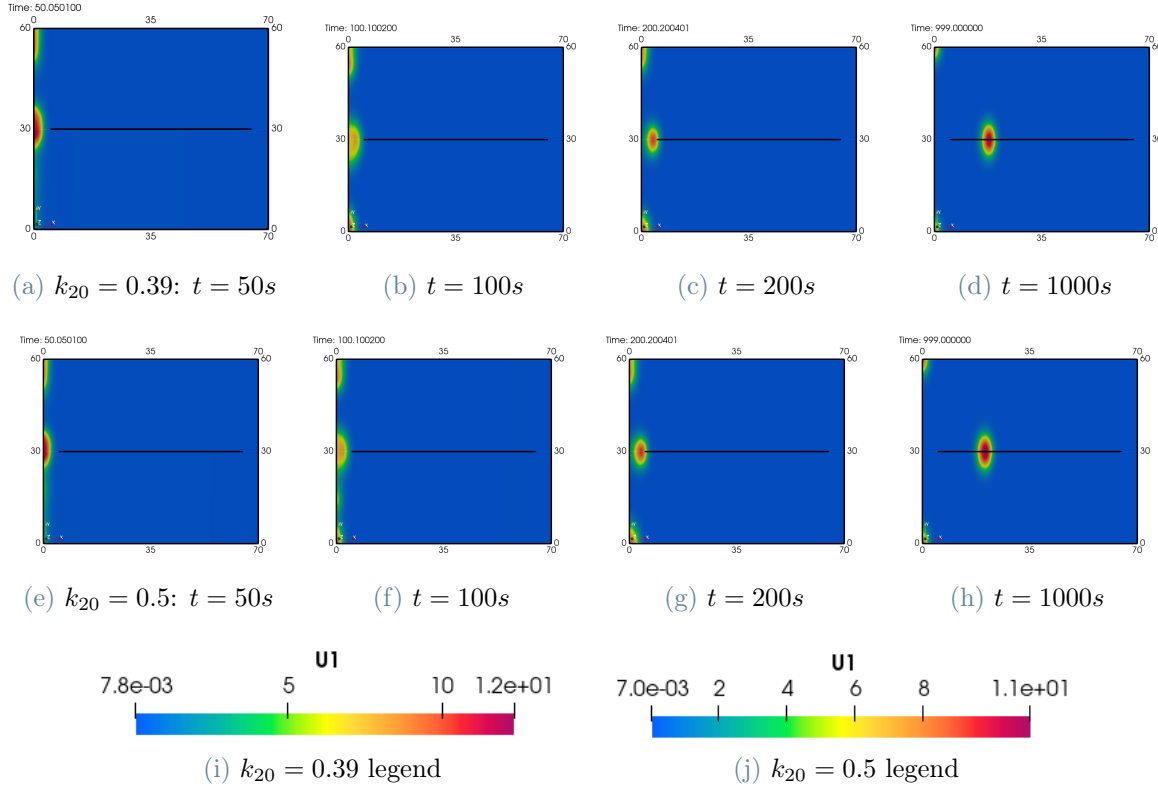


Figure 3.13: Active ROPs u evolution with RR algorithm solver with $k_{20} = 0.39$ (top row) and $k_{20} = 0.5$ (bottom row).

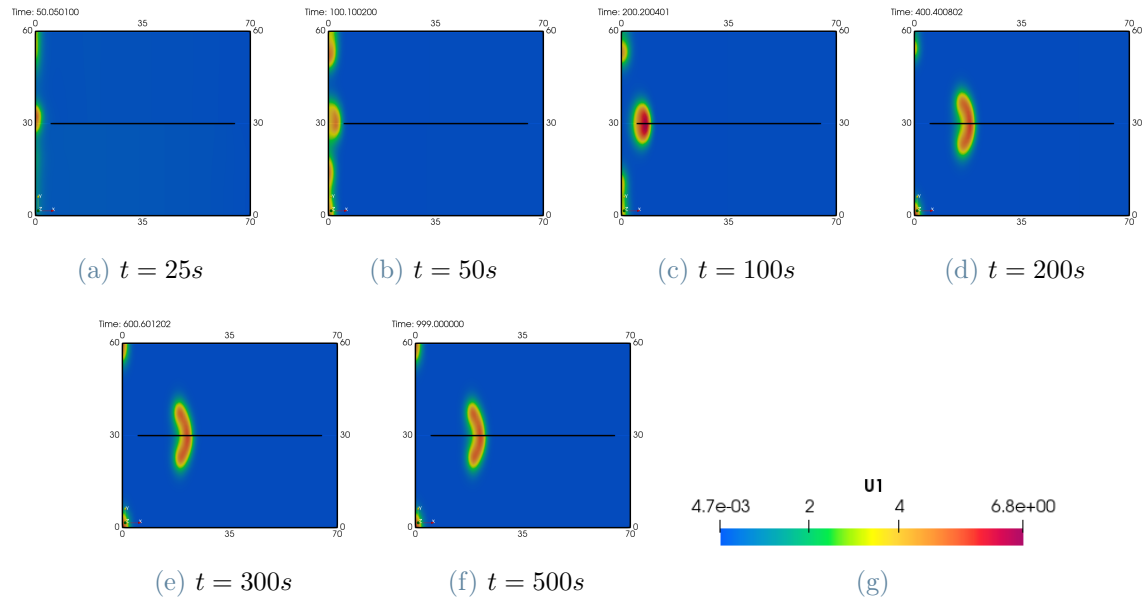


Figure 3.14: Active ROPs u evolution with RR algorithm solver with $k_{20} = 1.3562$.

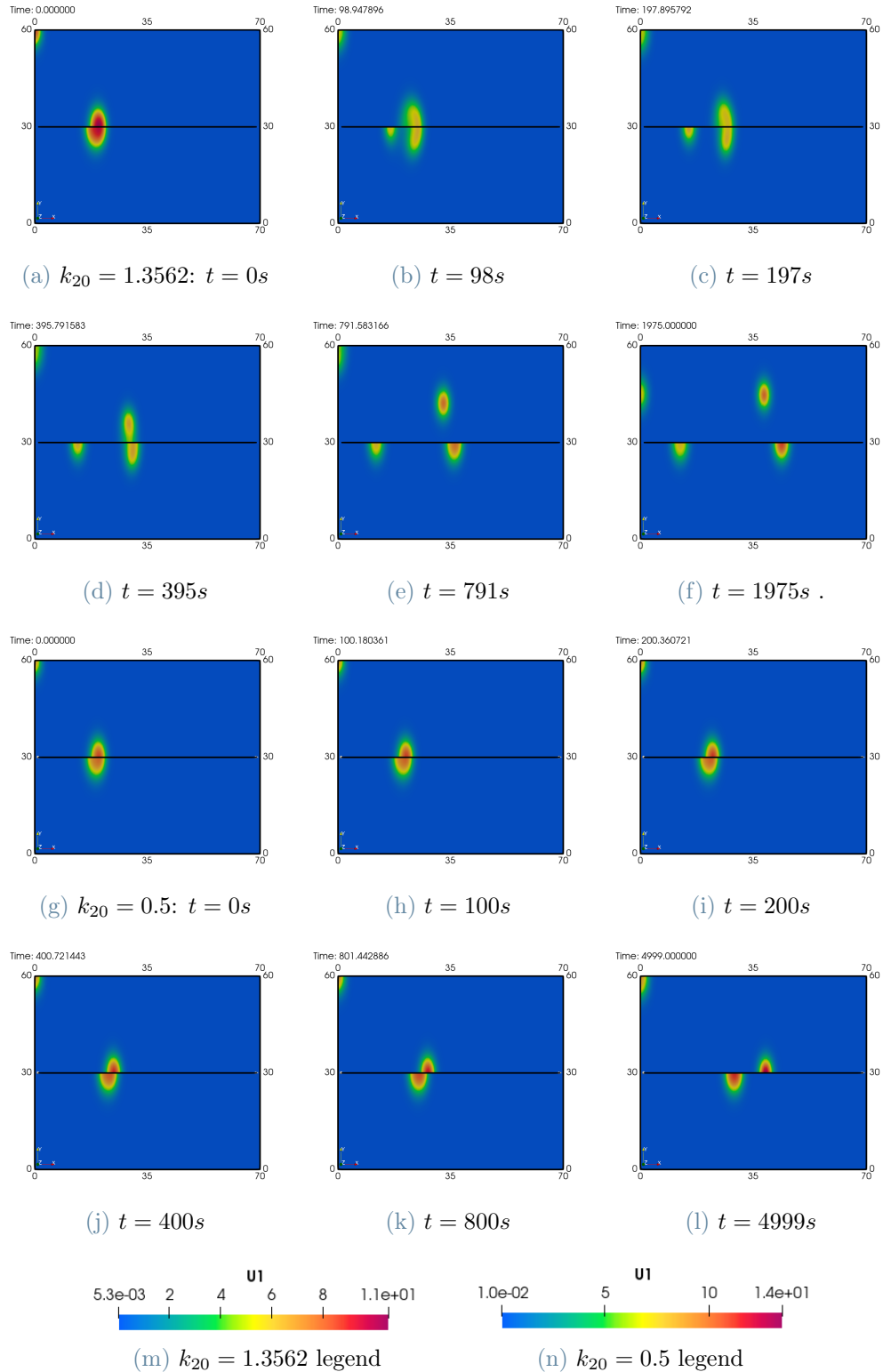


Figure 3.15: Active ROPs u evolution with RR algorithm solver with $k_{20} = 1.3562$ (top rows) and $k_{20} = 0.5$ (bottom rows), different start.

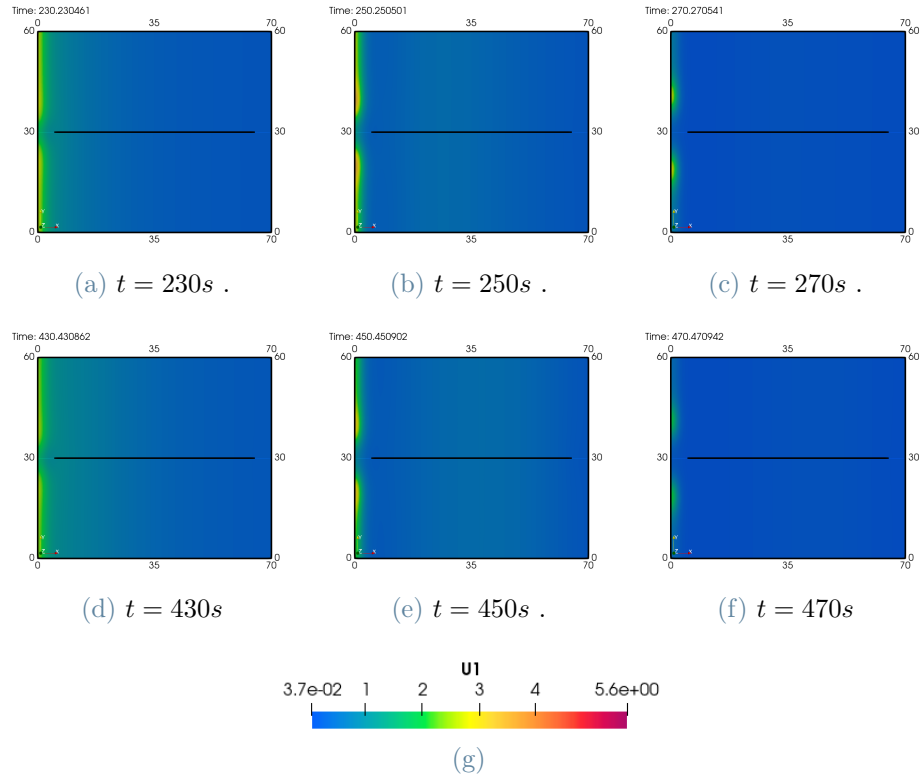


Figure 3.16: Active ROPs u evolution with exponential auxin and sinusoidal time-dependence with period $T_{pa} = 100s$.

3.3.5. Time-dependent auxin distribution

We present some results assuming time dependence for auxin distribution. These simulations can be conceived as intermediate steps before the more realistic results of Chapter 4, where auxin is determined through its transport model. We extract from other works realistic auxin distributions and we test our interpretation on the built pluricellular system.

Periodic auxin

At first we show results for a periodic overall auxin level characterized by a period $T_{pa}[s]$ in the following way:

$$k_{20}\alpha(x, t) = k_{20}e^{-\nu \frac{x}{L_x}} \sin\left(\frac{2\pi t}{T_{pa}}\right) + k_{20}, \quad (3.29)$$

so that auxin distribution $\alpha(x, t)$ takes values from k_{20} to $2k_{20}$.

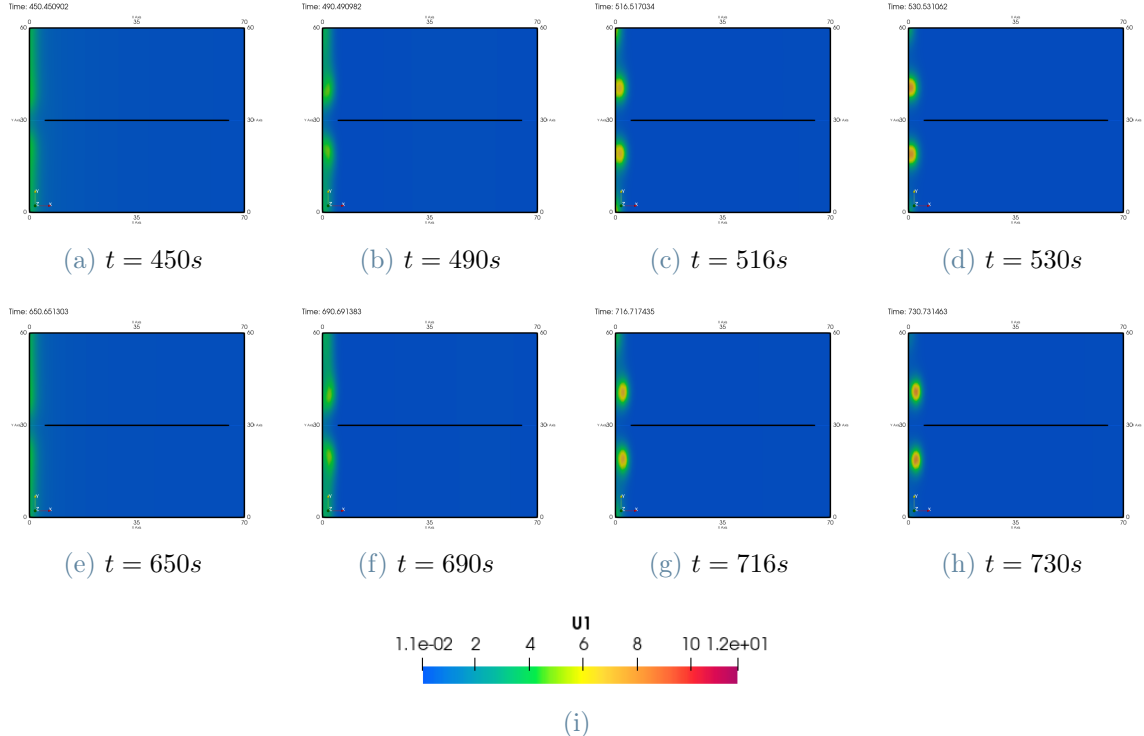


Figure 3.17: Active ROPs u evolution with exponential auxin and sinusoidal time-dependence with period $T_{pa} = 200s$.

A two cell system is initialized with

$$[U_1^0, V_1^0] = 1.5 [u^0, v^0], \quad [U_2^0, V_2^0] = [u^0, v^0],$$

using the same channels settings as for the test case in Figure 3.8.

For the two test cases in Figures 3.16 and 3.17, we select a period $T_{pa} = 100s$ and $T_{pa} = 200s$, respectively. Both the figures show that moving spots have not enough time to form since auxin gradient changes too quickly; still it is interesting to note how spot formation follows a periodicity in stripe generation and subsequent breakup. Indeed we can see in both the figures by comparing the first with the second row that location of active ROPs is periodically the same. For example, the frame at $t = 516s$ in Figure 3.17c is replicated similarly after 200s, i.e., at $t = 716s$, in Figure 3.17g. The feature of periodic "half-spot" formation confirms that auxin gradient is a key factor in determining hotspots. Similar considerations hold for Figure 3.16.

A more interesting test is obtained using $T_{pa} = 40min = 2400s$. The exponential dependence on space of auxin still brings a homoclinic stripe in correspondance to the auxin maximum and open channel.

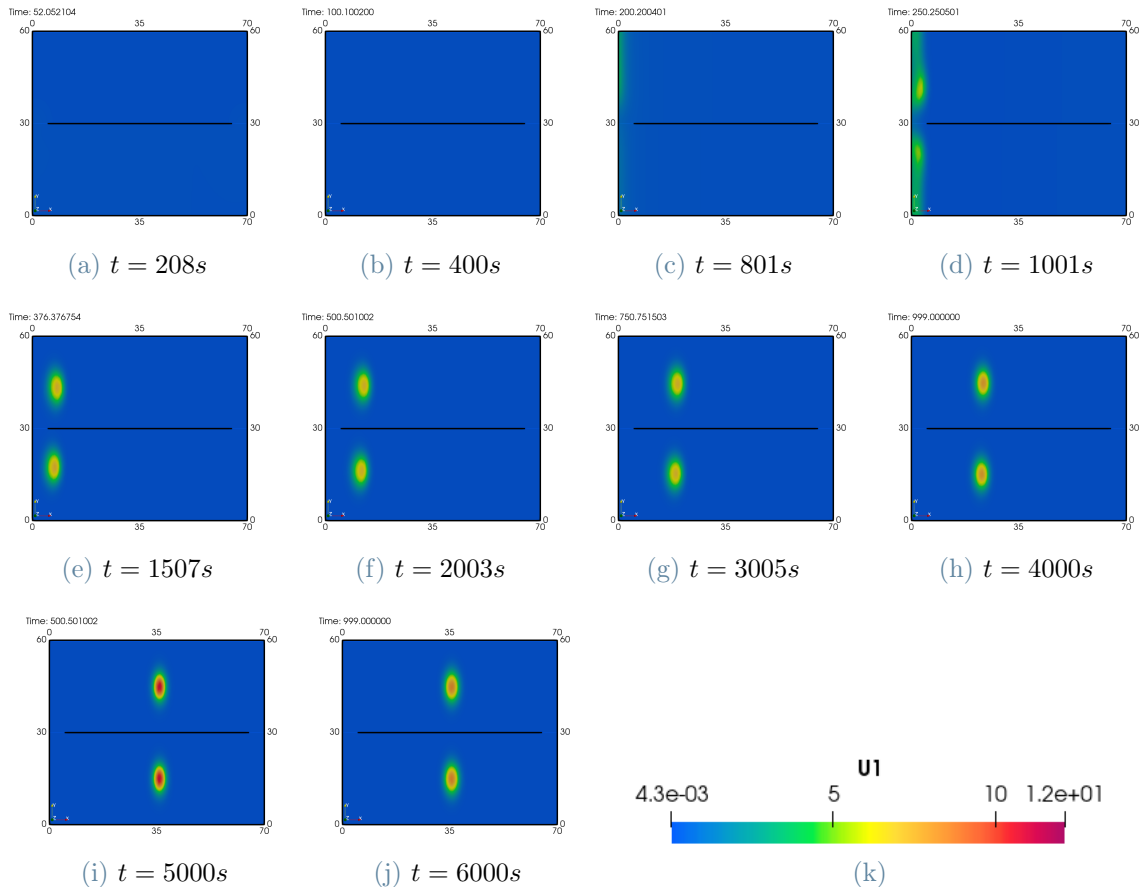


Figure 3.18: Active ROPs u evolution with exponential auxin with sinusoidal time-dependence, $T_{pa} = 40\text{min}$.

There is a first time-scale associated to the usual quick break-up instability and then a second longer time-scale associated with the slowly drifting of the spots where the auxin gradient is smaller. The period is sufficiently higher than the first time-scale and thus patches are able to form. The two spots formed seem to rest in a certain position and their amplitude oscillates with auxin values. The simulation gives us a proof of the biological stability of the pattern formation mechanism.

Auxin with maximum value smooth change

Driven by numerous studies in [14] over dependence of pattern formation on k_{20} parameter and by results in Section 3.3.4, we tested the multi-cellular method with a smooth change in overall auxin level, following the variation law:

$$k_{20}\alpha(x, t) = k_{20} \left[\frac{2}{\pi} \arctan(t - \tilde{T}) + \frac{3}{2} \right] \exp \left(-\nu \frac{x}{L_x} \right).$$

The idea was to start with a small auxin concentration in the cell equal to $k_{20} = 0.5$ and to increase it asymptotically close to the highest value we tested for k_{20} (see Figure 3.14).

Taking auxin exponential distribution with $\nu = 1.5$, a spot driving to the right is formed. Comparing the result in Figure 3.19 with the one in Figure 3.15, the milder change in auxin level brings a different evolution in the breakups of spots. A bigger unique spot is formed in the first 50s similar to Figure 3.12a, the following frame at time $t = 100s$ shows a more bended spot and after $t = \tilde{T} = 200s$ the simulation results start to recall the one in Figure 3.14. After more time steps, the increase in the overall auxin level brings multiple patches from the breakup of the peanut shaped one.

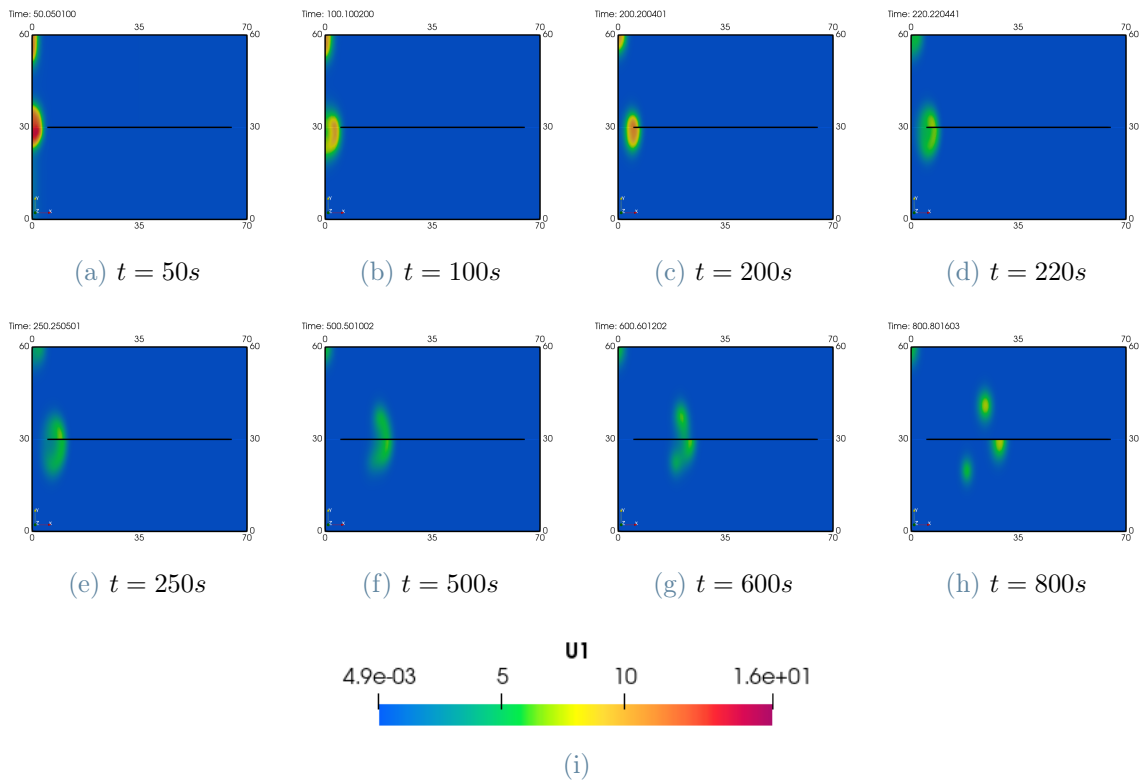


Figure 3.19: Active ROPs u evolution with RR solver with $k_{20}\alpha(x, t) = k_{20} \left[\frac{2}{\pi} \arctan(t - \tilde{T}) + \frac{3}{2} \right] \exp(-\nu \frac{x}{L_x})$, with $\tilde{T} = 200s$.

Auxin with maximum position moving

Other works and some results in the previous section highlight the importance of the location of the maximum and of the gradient of the auxin [14, 31]. Actually the position may change in time, because of other morphogenetic processes involved in root-hair initiation. This lead us to test, as a first approximated attempt, the behaviour of the system under moving maximum position of the auxin gradient. We keep a smooth dependence in space

defining the auxin distribution as follows:

$$k_{20}\alpha(x, t) = k_{20}\exp\left(-\nu\frac{x - x_0(t)}{L_x}\right)\mathbb{1}(x \geq x_0(t)) + k_{20}\exp\left(\nu\frac{x - x_0}{L_x}\right)\mathbb{1}(x \leq x_0(t)),$$

$x_0(t)$ being time-dependant.

We simulate the system up to $T_{max} = 4000s$, with auxin maximum position moving from the left to the right and representing itself again at the left boundary every interval of $1000s$. In particular maximum coordinate is defined as follows:

$$x_0(t) = \frac{L_x}{\tilde{T}}(t\%\tilde{T}).$$

In order to give a better idea, the gradient of auxin that crosses the cell system for the first interval of $1000s$ is presented in Figure 3.20.

The appearance of maximum auxin, probably influenced also by the open channels, increases the spot formation in the system and confirms the relevance in the location with respect to space and time of the auxin gradient. The hotspots interact with one another and alternate different behaviours, unifying in one single and then dividing in smaller spots.

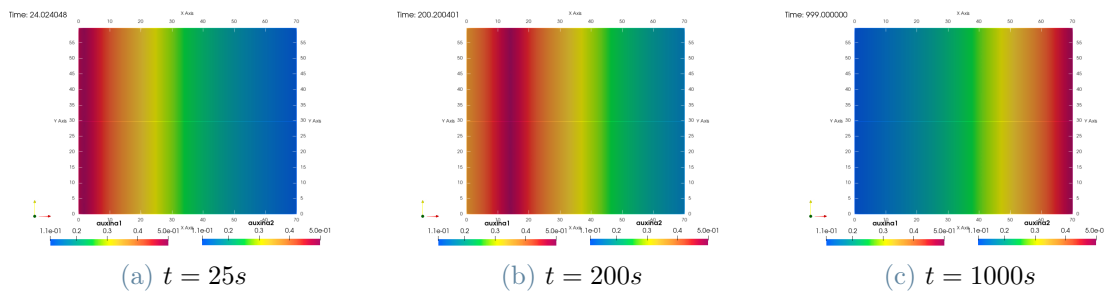


Figure 3.20: Evolution of the auxin distribution with maximum time-dependent position $x_0(t) = \frac{L_x}{\tilde{T}}(t\%\tilde{T})$.

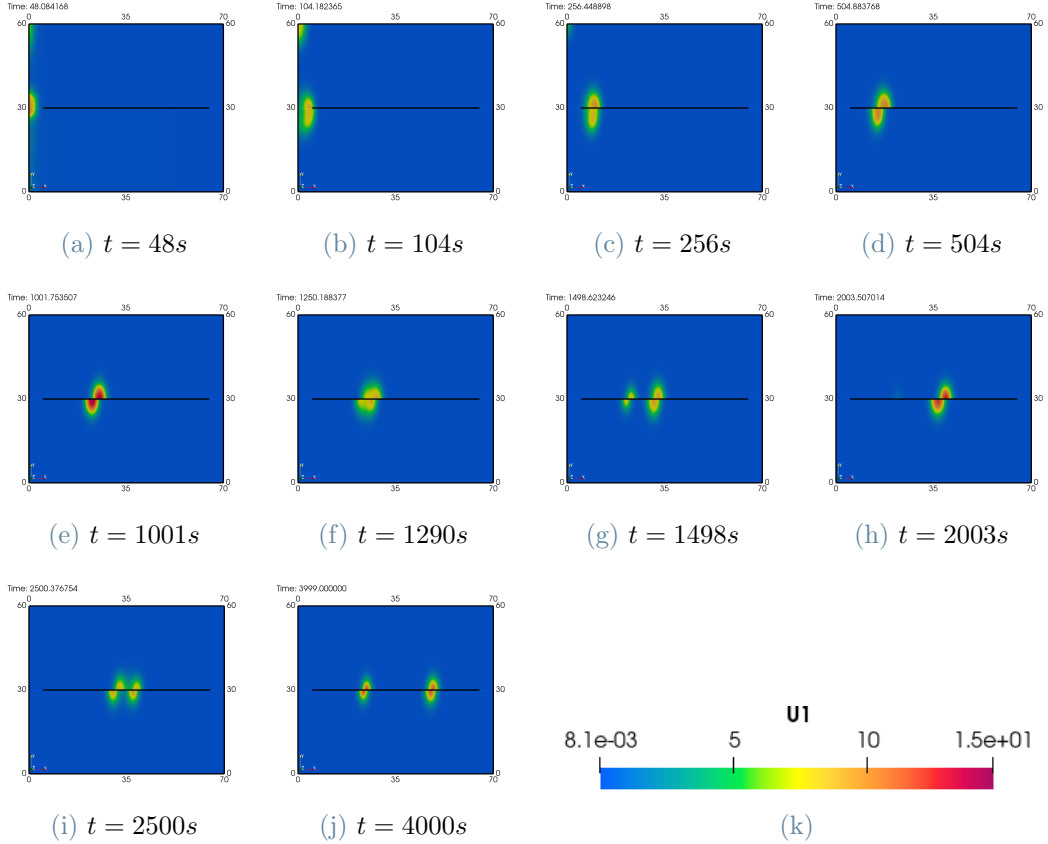


Figure 3.21: Active ROPs u evolution with exponential auxin with maximum position time-dependent $x_0(t) = \frac{L_x}{T}(t\% \tilde{T})$.

3.3.6. Four cell system

Finally, we implement a solver for a more complex multi-cellular system, in order to investigate the influence of a model of communication between cells both longitudinally and transversally. The new functions identifying open channels for inter-cellular communication are defined as follows:

$$\begin{aligned} \beta_{u/vRR} = & \mathbb{1}\left\{\frac{L_x}{2} - a_x - \epsilon_x \leq x \leq \frac{L_x}{2} - a_x\right\} + \mathbb{1}\left\{\frac{L_x}{2} + a_x \leq x \leq \frac{L_x}{2} + a_x + \epsilon_x\right\} \\ & + \mathbb{1}\left\{\frac{3L_x}{2} - a_x - \epsilon_x \leq x \leq \frac{3L_x}{2} - a_x\right\} + \mathbb{1}\left\{\frac{3L_x}{2} + a_x \leq x \leq \frac{3L_x}{2} + a_x + \epsilon_x\right\} \\ & + \mathbb{1}\left\{\frac{L_y}{2} - a_y - \epsilon_y \leq y \leq \frac{L_y}{2} - a_y\right\} + \mathbb{1}\left\{\frac{3L_y}{2} - a_y - \epsilon_y \leq y \leq \frac{3L_y}{2} - a_y\right\} \\ & + \mathbb{1}\left\{\frac{L_y}{2} + a_y \leq y \leq \frac{L_y}{2} + a_y + \epsilon_y\right\} + \mathbb{1}\left\{\frac{3L_y}{2} + a_y \leq y \leq \frac{3L_y}{2} + a_y + \epsilon_y\right\}, \end{aligned} \quad (3.30)$$

with a_y and ϵ_y having an analogous meaning for vertical borders as for a_x and ϵ_x for horizontal borders, respectively.

In Figure 3.22 the reference solution corresponding to a full no-flux boundary condition on all borders is presented. It was obtained setting the initial state to:

$$\begin{aligned} [U_1^0, V_1^0] &= [U_2^0, V_2^0] = 1.5 [u^0, v^0] \\ [U_3^0, V_3^0] &= [U_4^0, V_4^0] = [u^0, v^0], \end{aligned} \quad (3.31)$$

while the auxin distribution is defined as in (2.2) under Table 2.1 - Set C of parameters.

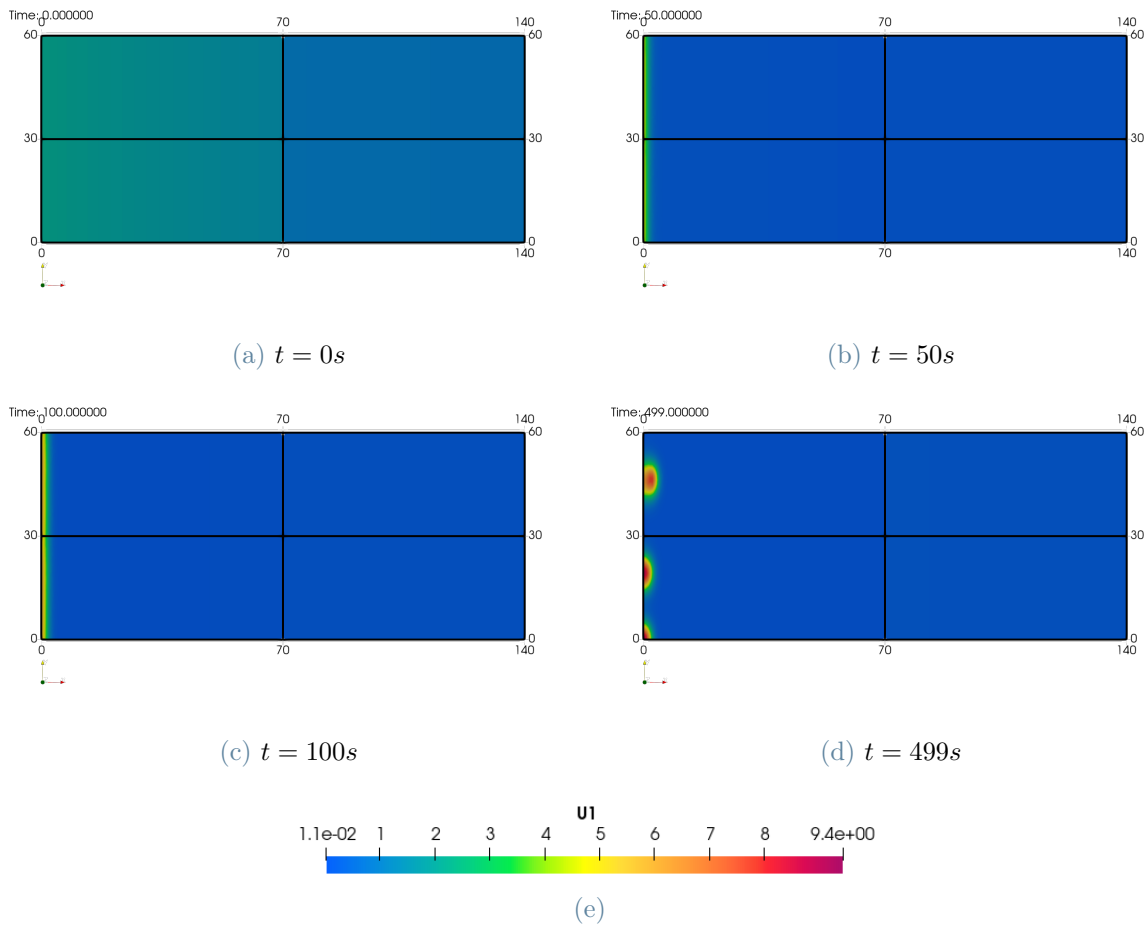


Figure 3.22: Active ROPs u evolution with RR algorithm solver on 4 cells system with $\beta_{RR} = 0$.

We replicate the no-flux reference solution with a different auxin distribution in order to have a possible comparison for other attempts with open transverse channels located where we have the maximum value for the auxin. We therefore set the auxin distribution as follows:

$$k_{20}\alpha(x) = k_{20}\exp\left(-\nu\frac{x-x_0}{L_x}\right)\mathbb{1}(x \geq x_0) + k_{20}\exp\left(\nu\frac{x-x_0}{L_x}\right)\mathbb{1}(x \leq x_0),$$

being $x_0 = L_x = 70\mu m$.

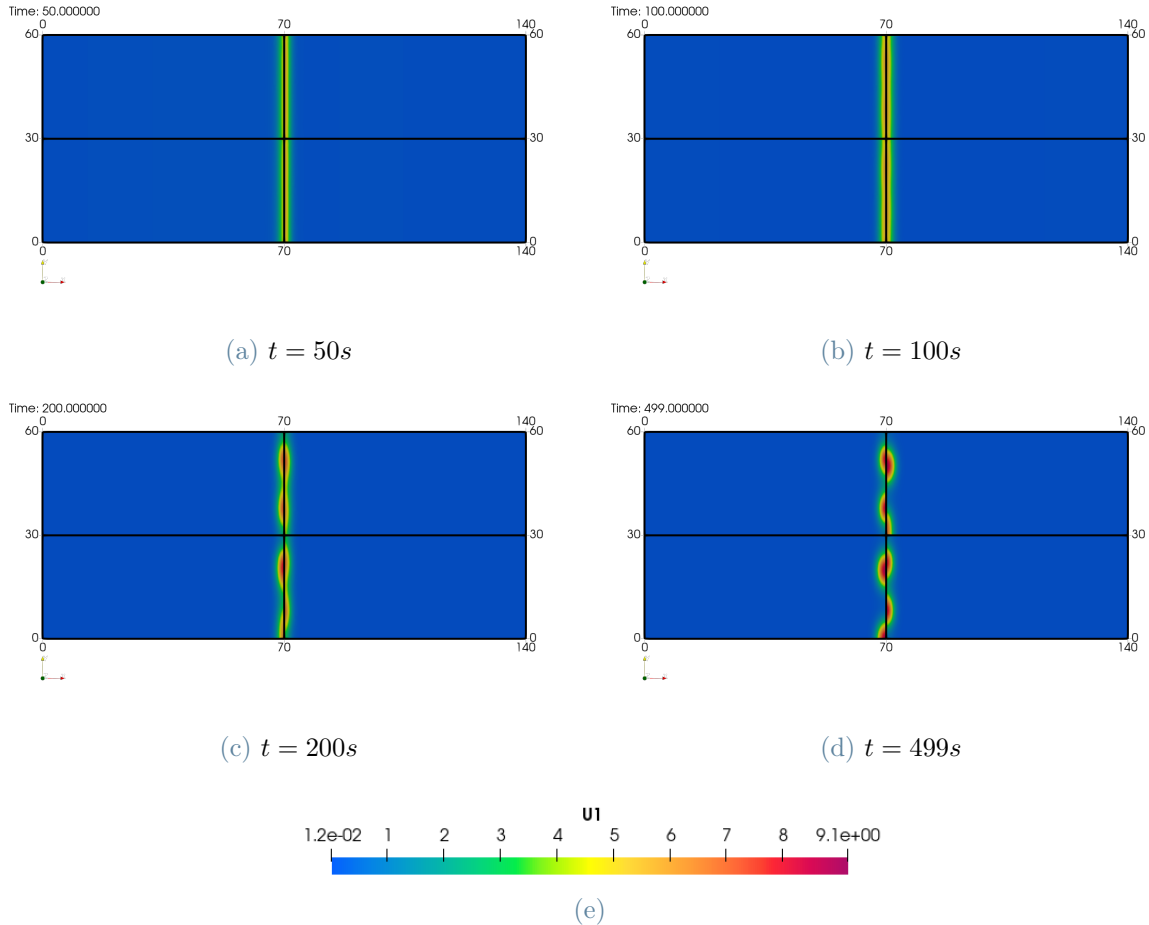


Figure 3.23: Active ROPs u evolution with RR algorithm solver on 4 cells system with α maximum in $x = 70\mu m$ and no-flux boundary condition: $\beta_{uRR} = \beta_{vRR} = 0$.

Figure 3.23 confirms the influence of auxin gradient in the location of the front formed and in the subsequent break-up instability of the stripe into spots.

In Figure 3.24 results obtained with channels characterized by parameters $\epsilon_x = 5, a_x = 30, \epsilon_y = 1$ and $a_y = 10$ are presented, without difference in the initialization of variables:

$$\begin{aligned} U_1^0 &= U_2^0 = U_3^0 = U_4^0 = u^0 \\ V_1^0 &= V_2^0 = V_3^0 = V_4^0 = v^0. \end{aligned}$$

We focus on this simulation in order to underline one feature of this RD system. The whole setting is symmetric with respect to the y axis, therefore the solution obtained should still be valid reflecting it. The solution here is not symmetric as expected because the slightly

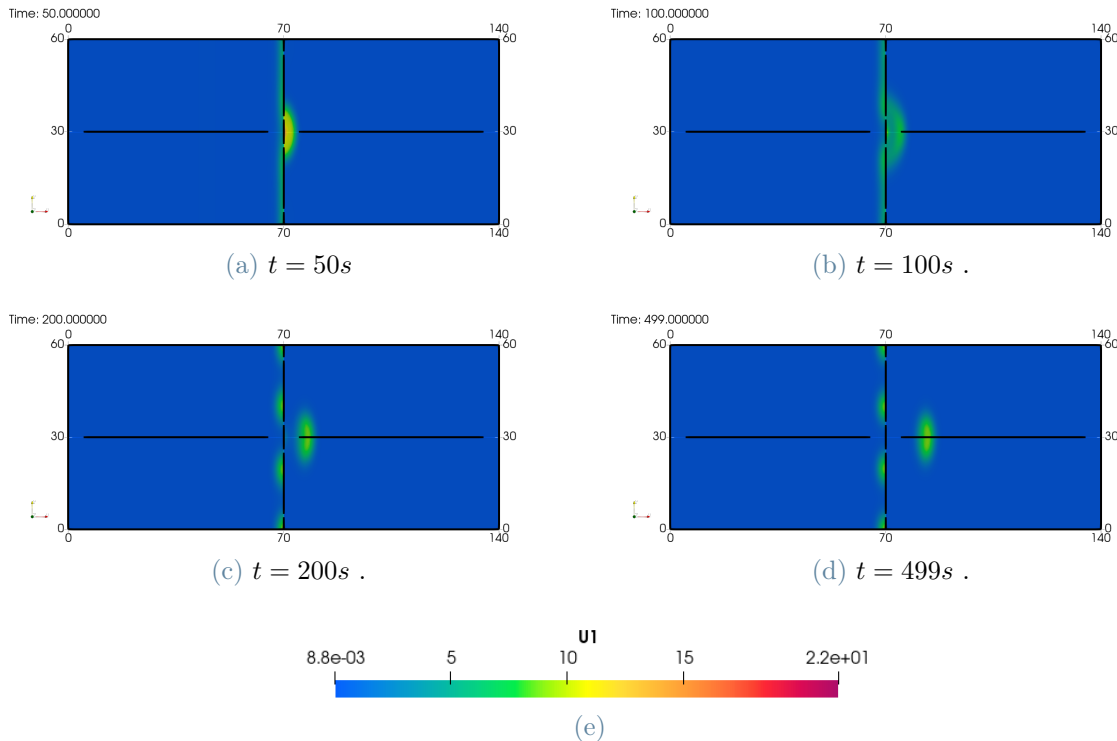


Figure 3.24: Active ROPs u evolution with RR algorithm solver on 4 cells system with α maximum in $x = 70\mu m$ and same initial state.

imperfection, in evolution is propagated and leads to different patterns between the right and left side of the four cells.

A completely different result is obtained with the difference in the initial concentrations of ROPs, as in (3.31); the discrepancy generates flux between neighboring cells in the direction of the auxin gradient. Results in Figure 3.25, obtained with opened channels and initial different concentrations, show a more symmetric and unified pattern formation, which is more feasible with respect to the one obtained when neglecting cells communications presented in Figure 3.23. Even if the system is homogeneous with respect to line $y = 30$ at the beginning, the spot formed at the end does not maintain this symmetry. A possible reason is the gradient in y direction because of open channels; it makes the upper and lower part evolve differently.

We then set the system with auxin maximum located at the right border, as follows:

$$k_{20}\alpha(x) = k_{20} \exp\left(\nu \frac{x - x_0}{L_r}\right) \mathbb{1}(x \leq x_0) \quad , \text{with } x_0 = 2L_x,$$

and we keep the initialization as in (3.31). Figure 3.26 shows that active ROPs are formed

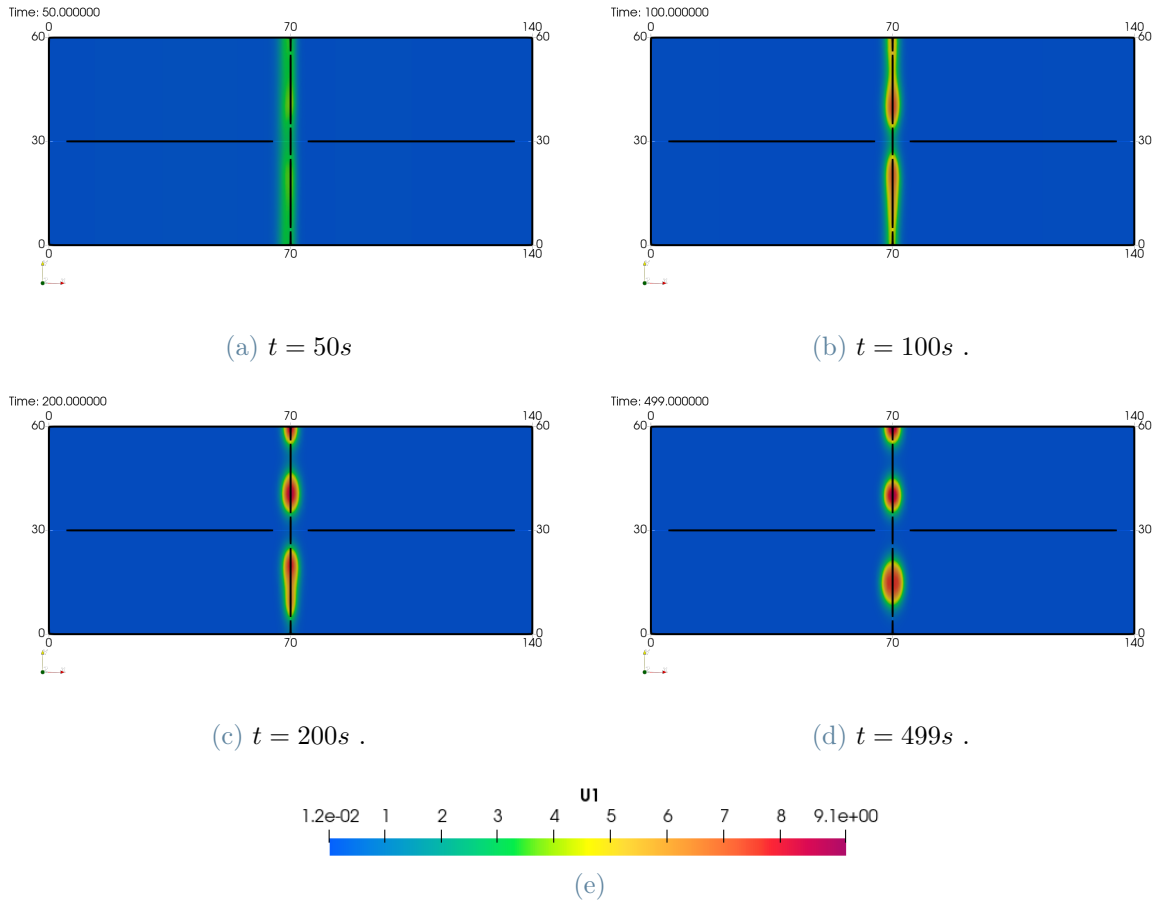


Figure 3.25: Active ROPs u evolution with RR algorithm solver on 4 cells system with α maximum in $x = 70\mu m$ and different initial state.

both because of gradient of auxin and because of fluxes between neighboring cells. Indeed, on one hand we again observe patches at the extreme right side where auxin maximum is located. On the other hand, at the transverse interface, auxin level is low and one should not expect spontaneous spot formation. Still, the difference at the beginning generates a gradient of ROPs along the x direction that cooperates with auxin and induces new hotspots at the interface of the cells.

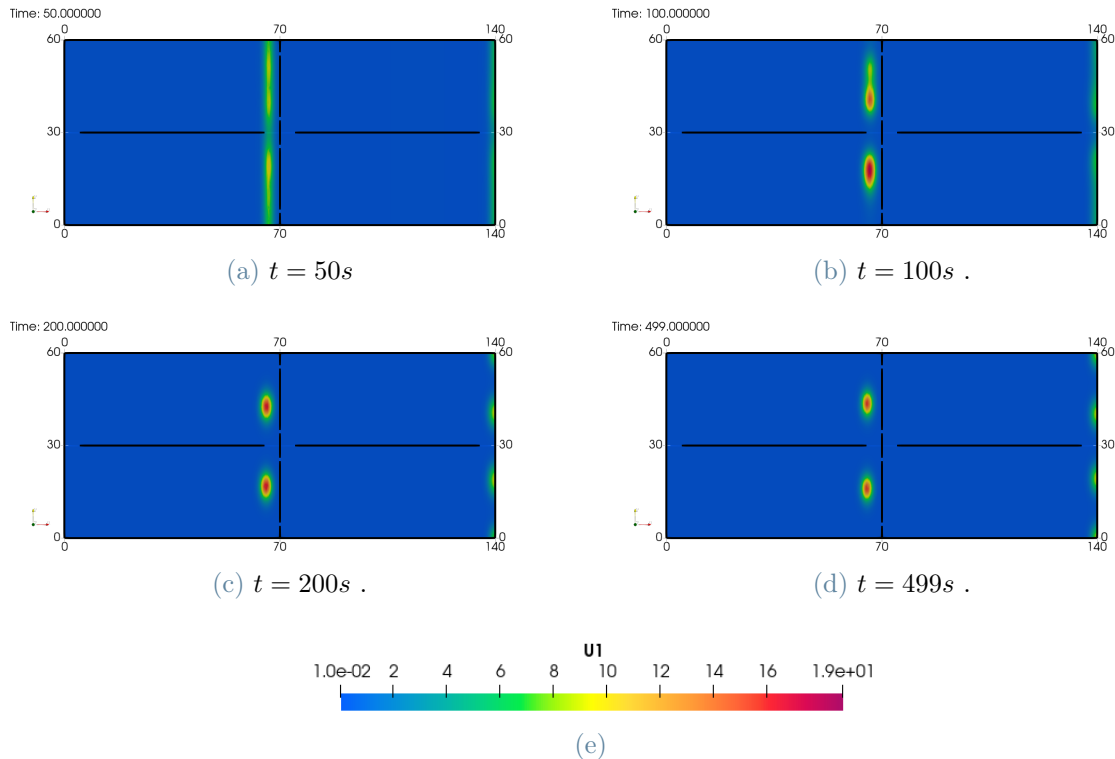


Figure 3.26: Active ROPs u evolution with RR algorithm solver on 4 cells system with α maximum in $x = 140\mu\text{m}$ and different initial state.

This is a first result that sustains the idea that a self-generated spot formation of ROPs may be induced not only by a gradient of auxin, but also by a gradient of ROPs itself.

Auxin with moving maximum position

We finally present for the multi-cellular system composed by four cells the results obtained by setting the system with initial state as defined in (3.31) and under the following auxin distribution:

$$k_{20}\alpha(x, t) = k_{20}\exp\left(-\nu \frac{x - x_0}{L_x}\right)\mathbb{1}(x \geq x_0) + k_{20}\exp\left(\nu \frac{x - x_0}{L_x}\right)\mathbb{1}(x \leq x_0),$$

with maximum position $x_0(t) = \frac{2L_x}{T_{max}}t$. The idea behind this attempts is similar to the ones presented before with a two cells system. Auxin distribution may change in time because of other biological processes. Other works stated the relevance of maximum location [31]. Here we impose an auxin gradient that crosses the system, with maximum moving from the extreme left side towards the right side.

In order to appreciate the dynamics observed, the simulation has to be compared with

results under fixed auxin distribution, having maximum at $x = 70\mu m$ or at the right side, presented in Figures 3.25 and 3.26 respectively.

Firstly, in Figure 3.27 auxin gradient influence on pattern formation is confirmed: it defines where stripes or patches locate and the velocity spots travel. A second stripe and subsequent spots emerge from homogeneous null concentration, after auxin maximum reaches the interface, probably thanks to the influence of open channels. The interplay between multi-cellular structural communication modelled and auxin distribution brings an instability of the system and patches are formed at the boundaries and transported through the system.

This result confirms the need to consider properly cell communication together with intra-cellular dynamic, in order to devise a complete model for root-hair initiation in a multi-cellular system.

We present in Tables 3.1 and 3.2 a scheme of the results in order to give to the reader an overview of the motivations and main conclusions of each test.

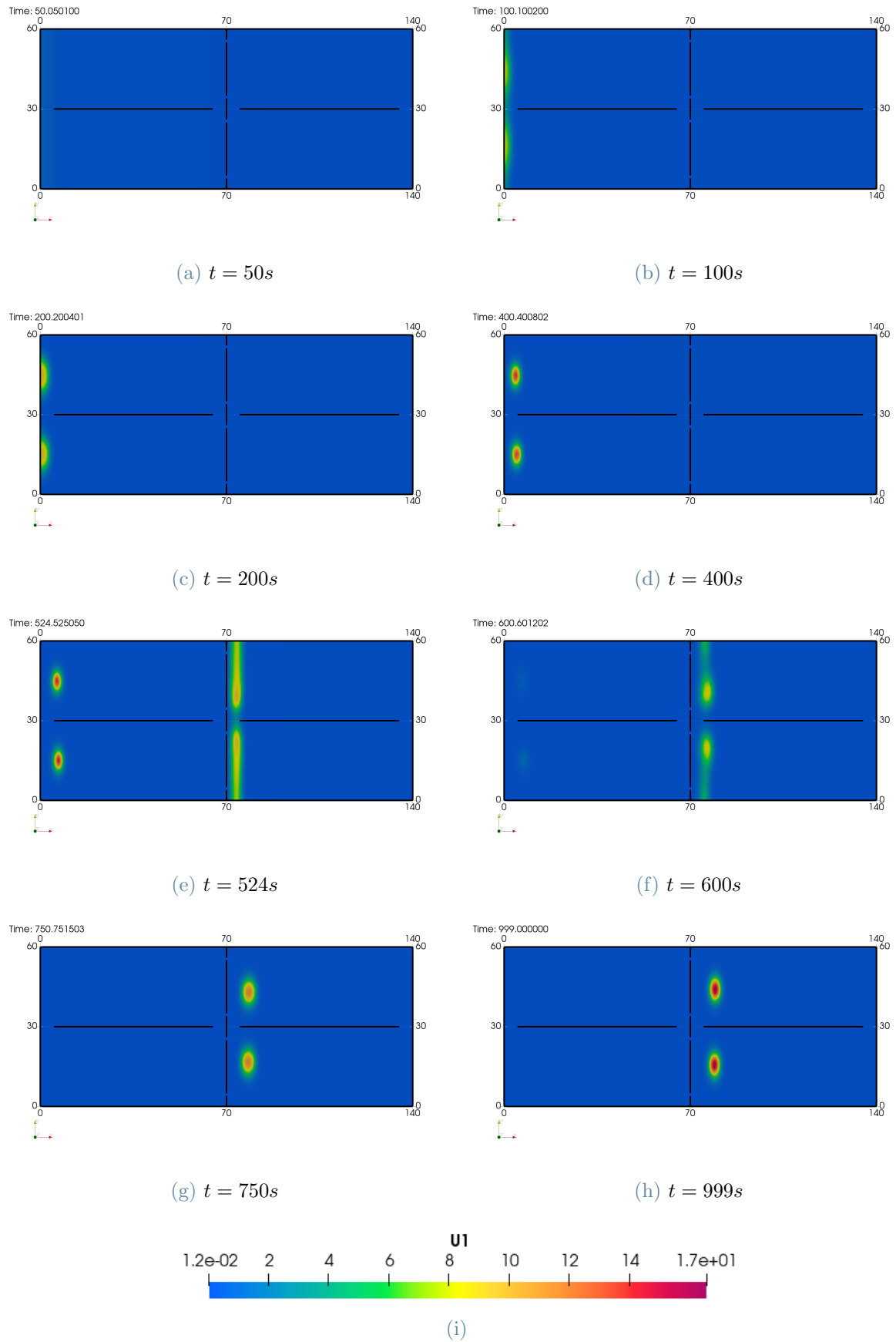


Figure 3.27: Active ROPs u evolution with RR algorithm solver on 4 cells system with auxin maximum moving to the right.

Table summarizing presented results

Experiment	Motivations	Main conclusions	Figures
E1	Simulate no-flux behaviour	Stagnant cells	3.2
E2 - vary a_x	Tuning channels parameters	Importance of channel location w.r.t auxin gradient	3.3 - 3.4 -3.5 - 3.6
E3 - vary ϵ_x	Tuning channels parameters	Amplitude of channels is less relevant	3.7 - 3.8
E4 - increase $\alpha_{u,vRR}$	Tuning channels parameters	Symmetry increase	3.9
E5	Test detailed sparse channels	Check good approximation of simple channels	3.10
E6	Test P mode vs NP mode	Considerable difference with relevant channels	3.11
E7 - k_{20}	Observe dependence of system on k_{20}	Increase of multiple spots and auxin advection power at borders	3.12 - 3.13 - 3.14 - 3.15
E8 auxin time-dep	Simulate periodic auxin: $T_{pa} = 100s, 200s$	Too small period	3.16 - 3.17
E9 auxin time-dep	Simulate periodic auxin: $T_{pa} = 40min$	Realistic driving spot	3.18
E10 auxin time-dep	Simulate soften change in k_{20}	Show a similar bending and breaking spots	3.19
E11 auxin time-dep	Simulate moving auxin maximum position periodically	Multiple spots periodically break	3.21

Table 3.1

Table summarizing presented results

Experiment	Motivations	Main conclusions	Figures
E12 4cells	Simulate no-flux with right maximum auxin	Stable spots form from break stripe	3.22
E13 4cells	Simulate no-flux with middle maximum auxin	Spot location depend on maximum location; no communication brings irregular spots	3.23
E14 4cells	Middle maximum auxin with open channels	Initial state gradient influence spot; symmetry issues	3.24 - 3.25
E15 4cells	Right auxin maximum with open channels	Both ROP flux and auxin gradient cooperate in spot formation	3.26
E16 4cells	Moving maximum auxin	Gradient of auxin and of ROPs influence spot appearance	3.27

Table 3.2

4 | Auxin-PIN dynamic system contribution to pattern formation

As stated in the introduction, previous results on root-hair initiation [2, 13, 14] discussed the importance of auxin gradient in determining pattern formation. The main assumption consists in assuming a certain, fixed in time, auxin distribution. Similarly, the results we proposed in Section 3.3 imply a-priori a hormone auxin concentration.

Auxin hormone actually is governed by a differential problem and various studies regarding auxin evolution in space and time are available in the literature [1, 15, 32]. Concentration-based and flux-based models are used to describe auxin trasport and PIN distribution on cell membrane.

The possibility to couple spatially-extended cellular models for ROPs pattern formation with concentration or flux-based models for auxin dynamics has not been examined yet, as far as we know.

In this chapter we develop a semi-implicit method to solve a particular model chosen for auxin dynamics, taken from [15], and show on a two cells system how active ROPs spot formation can be affected by this dynamics. The overall results confirm the importance for ROPs dynamics when modelling communication between cells.

4.1. Physical model

Taking into account a pluricellular system of N cells, the root-hair cells are projected onto a 2D rectangular domain as done in Section 3.1. We define for each cell Ω_i the set of neighboring cells \mathcal{N}_i . Auxin-PIN dynamics is meaningful only when considering a pluricellular system, since auxin model under study in [15] considers the transport and diffusion of auxin driven by a difference in auxin and PIN from one cell to the others. In order to describe the dynamics of auxin transport, the following variables are defined:

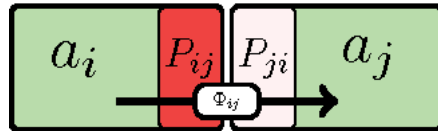


Figure 4.1: Two neighboring cells with concentrations of auxin, carriers proteins and flux from i to j ; figure taken from [15].

- $a_i [\text{mol m}^{-3}]$, the auxin concentration in cell Ω_i ;
- $\tilde{P}_{ij} [\text{mol m}^{-2}]$, the concentration of transporter proteins PIN facilitating transport from cell Ω_i to cell Ω_j .

Another important variable in the flux-based model is Φ_{ij} . It represents the flux of auxin from cell Ω_i to cell Ω_j , supposed to induce the insertion of PIN proteins \tilde{P}_{ij} . The flux is modelled through the combination of two contributions: the free diffusion towards neighboring cells $j \in \mathcal{N}_i$, and the active transport by the transporter (PIN) proteins. Variation of auxin a_i in cell Ω_i is therefore influenced by fluxes from neighboring cells together with a local production term and a decay term.

On the other hand, PIN variation is due to insertion and removal of PIN \tilde{P}_{ij} and to insertion induced by flux Φ_{ij} inside cell Ω_i .

To sum up, the dynamics of auxin and carriers proteins PIN in each cell Ω_i with $i \in \{1, \dots, N\}$ can be written as the following system of coupled ordinary differential equations:

$$\begin{cases} \frac{da_i}{dt} &= \frac{1}{V_i} \sum_{j=1}^N A_{ij} \Phi_{ij} + k - \delta a_i \\ \frac{d\tilde{P}_{ij}}{dt} &= h(\Phi_{ij}) + \rho_0 - \mu \tilde{P}_{ij}, \end{cases} \quad (4.1)$$

where coefficient $k[\text{mol m}^{-3} s^{-1}]$ is the constant rate auxin is produced, $\delta[s^{-1}]$ is the decay rate, $\rho_0[\text{mol m}^{-2} s^{-1}]$ is the insertion rate of PIN and $\mu[s^{-1}]$ the corresponding removal rate; V_i is the volume characterizing cell Ω_i and $A_{ij}[\text{m}^{-2}]$ is the exchange surface area between cell Ω_i and Ω_j . If cell Ω_i and Ω_j are not neighbours, $A_{ij}=0$ and $A_{ij} = A_{ji}$ holds for all cells. On the contrary, it is not necessarily true that \tilde{P}_{ij} and \tilde{P}_{ji} are equal [1, 15].

Flux from cell Ω_i to cell Ω_j is modeled as follows:

$$\Phi_{ij} = \left(T \tilde{P}_{ij} + \tilde{D}_a \right) a_i - \left(T \tilde{P}_{ji} + \tilde{D}_a \right) a_j, \quad (4.2)$$

being $\tilde{D}_a[\text{ms}^{-1}]$ the auxin diffusion coefficient and $T[\text{m}^{-3} \text{mol}^{-1} \text{s}^{-1}]$ the auxin transport efficiency coefficient.

Sets of parameters

Variable	Measure Unit	Value			
k	$mol \cdot m^{-3} s^{-1}$	F4	F5	F6	F7
δ	s^{-1}	0.1	10	0.5	0.5
D_a	$m \cdot s^{-1}$	1.0	1	0.5	0.5
μ	s^{-1}	1.0	0.1	0.3	7.0
ρ		{2; 2.3; 2.7 }		1.0	1.5
				2.8	

Table 4.1: Table with the four sets of parameters used in auxin-PIN model, taken from [15].

The intensity of PIN insertion due to the feedback of the auxin flux is described by a continuous, increasing function $h : \mathbb{R} \rightarrow \mathbb{R}_+$. Since the active trasport is directional, when more auxin comes in than goes out, no additional PIN is inserted. This modelling consideration in terms of function h implies that:

$$h(\Phi_{ij}) = 0 \text{ whenever } \Phi_{ij} \leq 0 \text{ and } h(\Phi_{ij}) > 0 \text{ for } \Phi_{ij} > 0. \quad (4.3)$$

The original system of equations can be rescaled and simplified. In particular, under the assumptions of cells having same volume $V = V_i$ and exchange surface areas $A = A_{ij}$, rescaling properly the diffusion coefficient D_a and variables P_{ij} , a new system is obtained. Thus, the final system of equations we work on is:

$$\begin{cases} \frac{da_i}{dt} &= \sum_{j \in \mathcal{N}_i} \Phi_{ji} + k - \delta a_i \\ \frac{dP_{ij}}{dt} &= h(\Phi_{ij}) - \mu P_{ij}, \end{cases} \quad (4.4)$$

where flux from cell Ω_i to cell Ω_j is redefined as follows:

$$\Phi_{ij} = (P_{ij} + D_a) a_i - (P_{ji} + D_a) a_j, \quad (4.5)$$

being P_{ij} and D_a dimentionally different from the original quantities \tilde{P}_{ij} and \tilde{D}_a .

Different sets of parameters, taken from [15], necessary for a complete simulation of the system (4.4) are collected in Table 4.1 .

Another important feature for characterizing auxin transport model is the definition of a

function to describe the feedback of the auxin flux into PIN insertion h . Typical choices of h found in literature are:

$$\begin{aligned} h(\Phi) &= \rho \frac{\Phi^n}{\theta^n + \Phi^n}, && \text{with } \theta \text{ saturating coefficient} \\ h(\Phi) &= \rho \Phi^n, && \text{without saturating coefficient,} \end{aligned} \quad (4.6)$$

ρ being a scaling coefficient.

The function $h(x) = \frac{x^5}{5^5+x^5} \mathbb{1}\{x > 0\}$ has been chosen for parameters sets F4 and F5 in Table 4.1 while $h(x) = \rho x \mathbb{1}\{x > 0\}$ has been adopted for sets F6 and F7.

In this chapter, we propose a new coupling between auxin-PIN transport problem and ROPs RD system. In particular, we recover the overall auxin level k_{20} of each cell Ω_i from the dynamic system (4.4) and then evaluate ROPs active and inactive concentrations solving the RD system in a pluricellular system. More precisely, we solve in sequence the auxin-PIN problem, we find auxin mean concentration $a_i \forall i \in \{1, \dots, N\}$, we assemble ROPs system replacing k_{20} parameters with different a_i computed one for each cell. In general, as in [15], we assume a homogeneous auxin locally in the cell (therefore ν is set equal to 0 in (2.2)). We are not considering exponential space distribution, but an auxin gradient only generated by difference in the mean concentration of auxin, from one cell to the neighbours.

4.2. Numerical discretization

In this section we employ a semi-implicit method to solve the auxin-PIN transport model. For simplicity, we focus the analysis on a two-cells system and therefore rewrite (4.4) for $N = 2$:

$$\begin{cases} \frac{da_1(t)}{dt} = \Phi_{21}(t) + k - \delta a_1(t) \\ \frac{da_2(t)}{dt} = \Phi_{12}(t) + k - \delta a_2(t) \\ \frac{dP_{12}(t)}{dt} = h(\Phi_{12}(t)) - \mu P_{12}(t) \\ \frac{dP_{21}(t)}{dt} = h(\Phi_{21}(t)) - \mu P_{21}(t). \end{cases} \quad (4.7)$$

We divide the time interval $[0, T_{max}]$ into N_{max} sub-intervals such that $t^n = n\Delta t$ with $\Delta t = T_{max}/N_{max}$. We define a_i^n and P_{ij}^n as approximations of the solutions evaluated at time t^n :

$$a_i(t^n) \simeq a_i^n, \quad P_{ij}(t^n) \simeq P_{ij}^n. \quad (4.8)$$

For the time derivative, we apply the implicit Euler method as follows:

$$\begin{cases} \frac{a_1^{n+1} - a_1^n}{\Delta t} = \Phi_{21}^{n+1} + k - \delta a_1^{n+1} \\ \frac{a_2^{n+1} - a_2^n}{\Delta t} = \Phi_{12}^{n+1} + k - \delta a_2^{n+1} \\ \frac{P_{12}^{n+1} - P_{12}^n}{\Delta t} = h(\Phi_{12}^{n+1}) - \mu P_{12}^{n+1} \\ \frac{P_{21}^{n+1} - P_{21}^n}{\Delta t} = h(\Phi_{21}^{n+1}) - \mu P_{21}^{n+1}. \end{cases} \quad (4.9)$$

We explicit the flux in the auxin equations:

$$\begin{cases} \frac{a_1^{n+1} - a_1^n}{\Delta t} = (P_{21}^{n+1} + D_a) a_2^{n+1} - (P_{12}^{n+1} + D_a) a_1^{n+1} + k - \delta a_1^{n+1} \\ \frac{a_2^{n+1} - a_2^n}{\Delta t} = (P_{12}^{n+1} + D_a) a_1^{n+1} - (P_{21}^{n+1} + D_a) a_2^{n+1} + k - \delta a_2^{n+1} \\ \frac{P_{12}^{n+1} - P_{12}^n}{\Delta t} = h(\Phi_{12}^{n+1}) - \mu P_{12}^{n+1} \\ \frac{P_{21}^{n+1} - P_{21}^n}{\Delta t} = h(\Phi_{21}^{n+1}) - \mu P_{21}^{n+1}. \end{cases} \quad (4.10)$$

The system is highly non-linear because of the definition of the fluxes of auxin Φ_{12} and Φ_{21} and due to the non-linear function h . Therefore, we decide to use a semi-implicit method in order to linearize the system. Since we are more interested in auxin concentration rather than the PIN concentration, we keep implicit a_1 and a_2 , while discretize explicitly P_{12} and P_{21} in the first two equations. Regarding PIN equations, function h depends on the sign of the argument and contributes coming from auxin and PIN concentrations cannot linearized as before. Therefore we decide to treat explicitly the flux input inside h function.

The semi-implicit counterpart of (4.10) is thus given by:

$$\begin{cases} \frac{a_1^{n+1} - a_1^n}{\Delta t} = (P_{21}^n + D_a) a_2^{n+1} - (P_{12}^n + D_a) a_1^{n+1} + k - \delta a_1^{n+1} \\ \frac{a_2^{n+1} - a_2^n}{\Delta t} = (P_{12}^n + D_a) a_1^{n+1} - (P_{21}^n + D_a) a_2^{n+1} + k - \delta a_2^{n+1} \\ \frac{P_{12}^{n+1} - P_{12}^n}{\Delta t} = h(\Phi_{12}^n) - \mu P_{12}^{n+1} \\ \frac{P_{21}^{n+1} - P_{21}^n}{\Delta t} = h(\Phi_{21}^n) - \mu P_{21}^{n+1}. \end{cases} \quad (4.11)$$

This linearized system can be rewritten in algebraic form as follows:

$$A\mathbf{X} = \mathbf{b}, \quad (4.12)$$

where

$$\mathbf{X} = \begin{bmatrix} a_1^{n+1} \\ a_2^{n+1} \\ P_{12}^{n+1} \\ P_{21}^{n+1} \end{bmatrix}, \quad \mathbf{b} = \begin{bmatrix} \frac{1}{\Delta t} a_1^n + k \\ \frac{1}{\Delta t} a_2^{n+1} + k \\ \frac{1}{\Delta t} P_{12}^n + h(\Phi_{12}^n) \\ P_{21}^{n+1} + h(\Phi_{21}^n) \end{bmatrix}, \quad (4.13)$$

$$A = \begin{bmatrix} \frac{1}{\Delta t} + P_{12}^n + D_a + \delta & -P_{21}^n - D_a & 0 & 0 \\ -P_{12}^n - D_a & \frac{1}{\Delta t} + P_{21}^n + D_a + \delta & 0 & 0 \\ 0 & 0 & \frac{1}{\Delta t} + \mu & 0 \\ 0 & 0 & 0 & \frac{1}{\Delta t} + \mu \end{bmatrix}.$$

The semi-implicit method partially decouples the dynamics between auxin and PIN concentrations. In particular, at each time-step we solve a linear system to find the vector of auxin concentrations $\mathbf{a} = [a_1^{n+1}, a_2^{n+1}]$, whereas each PIN concentration P_{12}^{n+1} , P_{21}^{n+1} is computed with a simple division. We define the auxin system matrix A_a and right hand side vector \mathbf{b}_a as

$$A_a = \begin{bmatrix} \frac{1}{\Delta t} + P_{12}^n + D_a + \delta & -P_{21}^n - D_a \\ -P_{12}^n - D_a & \frac{1}{\Delta t} + P_{21}^n + D_a + \delta \end{bmatrix}, \quad \mathbf{b}_a = \begin{bmatrix} \frac{1}{\Delta t} a_1^n + k \\ \frac{1}{\Delta t} a_2^{n+1} + k \end{bmatrix}; \quad (4.14)$$

then the linear system for auxin concentrations is formulated as follows:

$$A_a \mathbf{a} = \mathbf{b}_a. \quad (4.15)$$

Then, for updating PIN P_{ij} concentration for a generic i, j we only compute it as follows:

$$P_{ij}^{n+1} = \left(\frac{1}{\Delta t} + \mu \right)^{-1} \left[\frac{1}{\Delta t} P_{ij}^n + h(\Phi_{ij}^n) \right]. \quad (4.16)$$

To sum up, given an initial state of the system, $\mathbf{a}^0 = [a_1^0, a_2^0]$, P_{12}^0 and P_{21}^0 , usually selected randomly from 0 and 1, for $n = 0, \dots, N_{max} - 1$ we find $\mathbf{a}^{n+1} = [a_1^{n+1}, a_2^{n+1}]$ solving the linear system (4.15) and we update P_{12}^{n+1} and P_{21}^{n+1} values with formula (4.16).

After solving the auxin-PIN model applying the semi-implicit method, we replace values of local overall auxin level k_{20} in each cell with the auxin concentration a_i^{n+1} and solve

the ROPs system. The complete procedure to solve the auxin-PIN model together with RD involving ROPs proteins is presented synthetically in Algorithm 4.1.

Algorithm 4.1 Pluricellular system solver procedure: RR coupled with auxin-PIN dynamics

Given $N \geq 1$ cells, k_i

```

1: Initialization:  $\forall i = 1, \dots, N$ 
2: [ai] randomly init
3: [PINi] randomly init
4:  $[\mathbf{U}_{0i}, \mathbf{V}_{0i}] \leftarrow [k_i u_0, k_i v_0]$ 
5:  $[\mathbf{U}_{iprec}, \mathbf{V}_{iprec}] \leftarrow [\mathbf{U}_{0i}, \mathbf{V}_{0i}]$ 
6: while  $t < T_{max}$  do
7:   update ai and PINi matrices and vectors
8:   solve auxin-PIN problem (4.15) - (4.16)
9:   update  $k_{20}$ 
10:  assemble matrix for  $\forall i = 1, \dots, N$ 
11:  for  $iter < N_{iter}$  do
12:     $\forall i = 1, \dots, N$ 
13:    compute BC contribute from  $j \in \mathcal{N}_i$ 
14:    interpolate on  $i$ 
15:    update rhs
16:    solve  $\Omega_i$  problem (3.2)
17:    update residual, check tolerance, update iter
18:     $[\mathbf{U}_{iprec}, \mathbf{V}_{iprec}] \leftarrow [\mathbf{U}_i, \mathbf{V}_i]$ 
19:  end for
20:   $[\mathbf{U}_{0i}, \mathbf{V}_{0i}] \leftarrow [\mathbf{U}_i, \mathbf{V}_i]$ 
21: end while

```

4.3. Numerical Results

In this section we present some of the results obtained by resorting to Algorithm 4.1 in order to couple auxin-PIN transport model and ROPs multi-cellular system. In the majority of works about auxin dynamics, auxin distribution has been modelled within a strand of cells. Thus, the multi-cellular systems to solve is composed by two cells attached along the short side, as the scheme in Figure 4.1 illustrates. In particular, Ω_1 corresponds to the left cell and Ω_2 to the right one.

In the first subsection we present an intermediate result, applying the RR solver on a

strand of two cells without considering auxin-PIN dynamics. Then, we test Algorithm 4.1 under different sets of parameters and we validate the multi-cellular model changing channel characterization.

4.3.1. ROPs system in a strand of two cells

We test the array of two cells under exponential auxin distribution as in equation (2.2) and choosing as initial state:

$$[U_1^0, V_1^0] = 1.5 [u^0, v^0], \quad [U_2^0, V_2^0] = [u^0, v^0]. \quad (4.17)$$

The two cells have channel functions defined as follows:

$$\begin{aligned} \beta_{uRR} &= \mathbb{1}\left\{\frac{L_y}{2} - a_y - \epsilon_y \leq y \leq \frac{L_y}{2} - a_y\right\} + \mathbb{1}\left\{\frac{L_y}{2} + a_y \leq y \leq \frac{L_y}{2} + a_y + \epsilon_y\right\} \\ \beta_{vRR} &= \mathbb{1}\left\{\frac{L_y}{2} - a_y - \epsilon_y \leq y \leq \frac{L_y}{2} - a_y\right\} + \mathbb{1}\left\{\frac{L_y}{2} + a_y \leq y \leq \frac{L_y}{2} + a_y + \epsilon_y\right\}. \end{aligned} \quad (4.18)$$

In the majority of tests, we set $a_y = 5$ and $\epsilon_y = 5$.

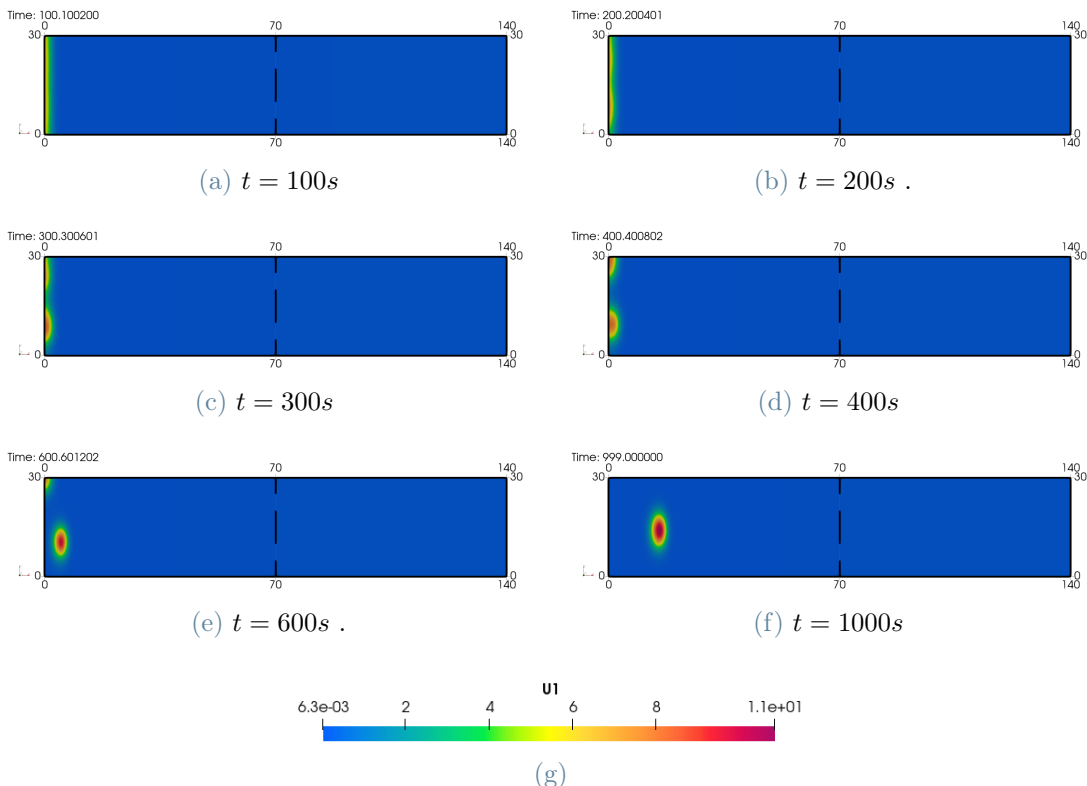


Figure 4.2: Active ROPs u evolution with RR algorithm solver on 2 cells system with $a_y = 5, \epsilon_y = 5$.

Figure 4.2 shows results obtained still taking auxin distribution defined a priori and not considering the dynamic system with PIN carriers. This simulation shows a behaviour similar to the results in Section 3.3. A front is formed at the border where auxin maximum is located and it breaks into spots, subsequent travelling towards minimum of auxin. It confirms that auxin gradient guarantees pattern formation.

4.3.2. Coupled ROPs model with auxin-PIN dynamics

We present some relevant results of the multi-cellular system for ROP pattern formation under chemical dynamics between auxin and PIN. In particular, we aim at observing the generation and evolution of active spots of ROPs in the system, under different types of auxin dynamics.

Sets of parameters F4 and F5 in Table 4.1, depending on the number of cells in the strand, leads to alternating sources and sinks of auxin. Sinks are cells with high auxin and incoming flux, whereas sources are groups of cells with low auxin and outgoing flux.

Auxin-PIN system under the F4 set of parameters converges after few seconds to a homogeneous auxin distribution, with $a_1 = a_2 = 1$. Therefore the system is characterized by no gradient of auxin (see Figure 4.3). We observe a considerable spot formation in Figure 4.4. Firstly a homoclinic stripe is formed at the right of the common interface, then it breaks into multiple spots. After some seconds, another stripe is formed in the left cell and simultaneously the spots formed in the right part start travelling towards the exterior. A plausible responsible for this self-generated pattern is the gradient of ROPs generated by the initial difference in initial states and the open channels, as it happens in Figure 3.26.

Auxin-PIN system under the set F5 of parameters shows a different behaviour. As can be seen in Figure 4.5, auxin concentration in the first and second cell converges to the same low value $a_1 = a_2 = 0.1$ and, as for the F4 set of parameters, there is no auxin gradient characterizing the system after few time steps.

Differently from Figure 4.4, the numerical output in Figure 4.6 is characterized by active ROPs concentration converging to a null homogeneous state. The possible reason is that the overall auxin level is too low to sustain spot formation. The gradient of ROPs generated by open channels may not be enough and it still need a sufficient high, even if constant, concentration of auxin to form hotspots, coherently with Figure 4.4.

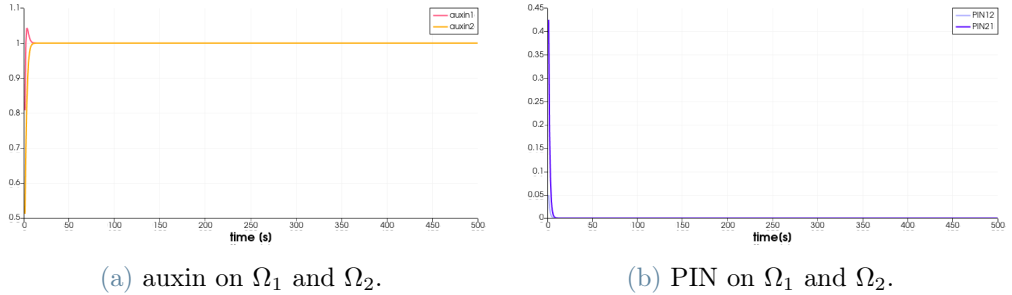


Figure 4.3: auxin-PIN dynamics on 2 cells system with the F4 parameters set.

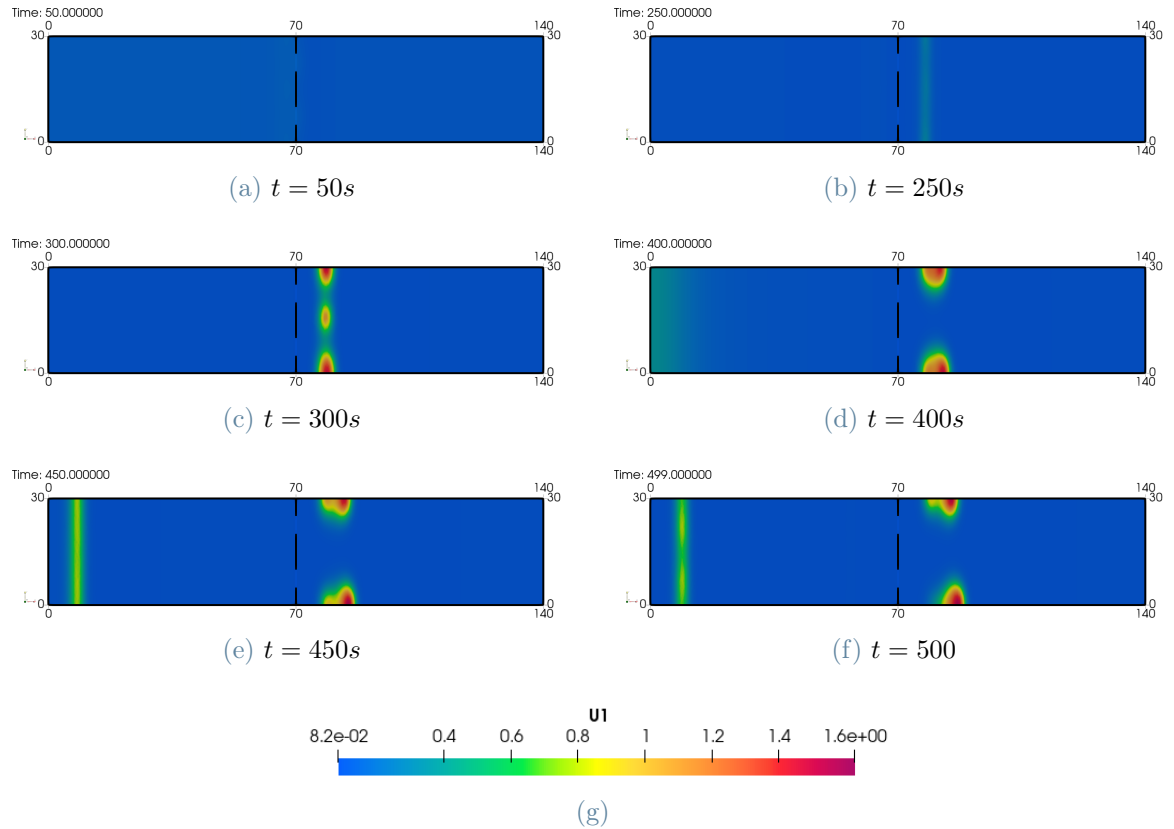


Figure 4.4: Active ROPs u evolution with RR algorithm solver on 2 cells system coupled with auxin-PIN dynamics, with the F4 parameters set.

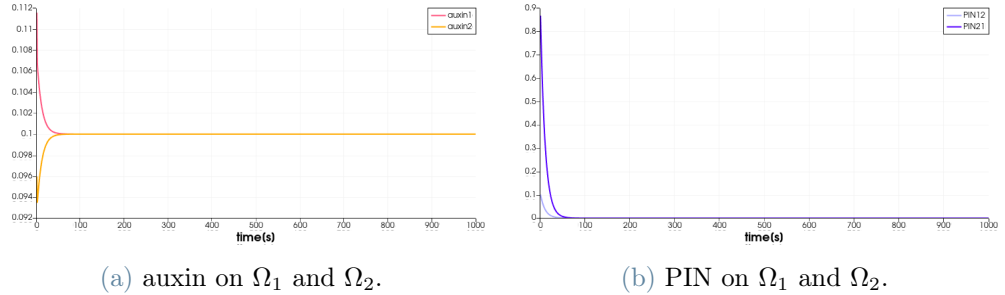
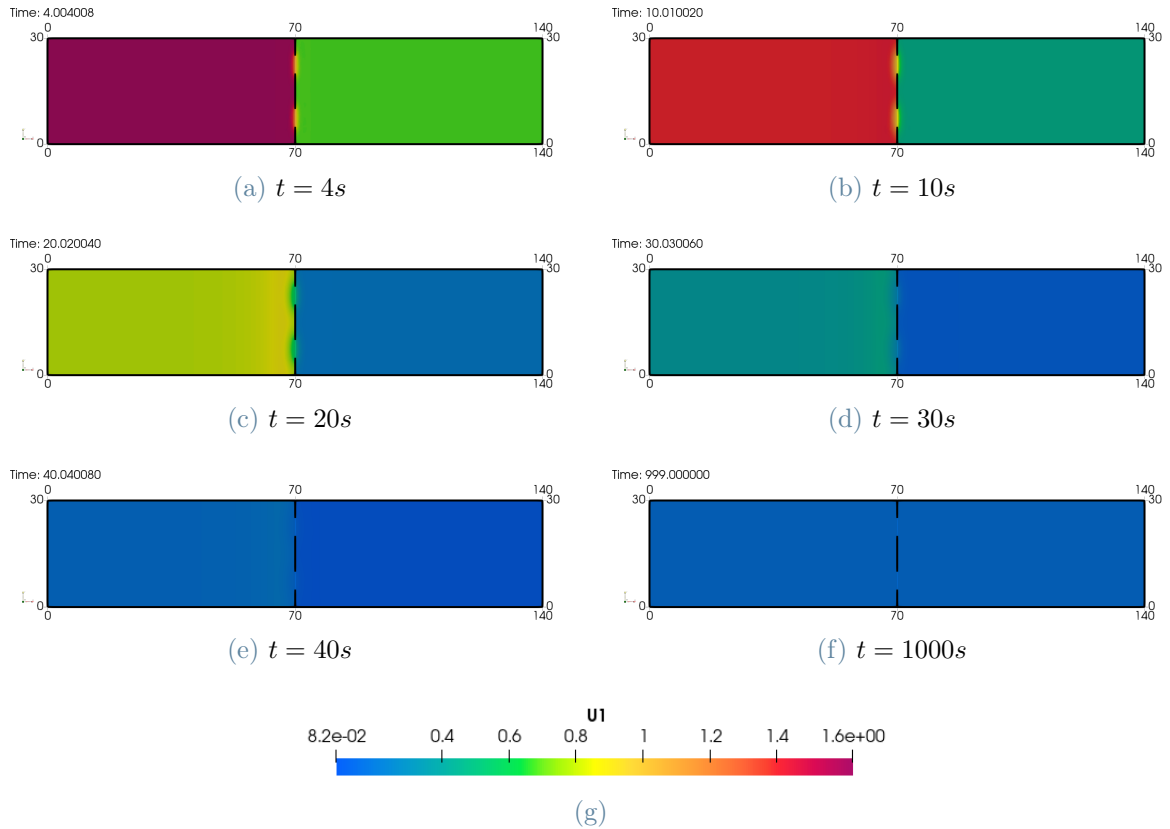


Figure 4.5: auxin-PIN dynamics on 2 cells system with the F5 parameters set.

Figure 4.6: Active ROPs u evolution with RR algorithm solver on 2 cells system coupled with auxin-PIN dynamics, with the F5 parameters set.

We then set the system to solve auxin-PIN dynamics under the set F6 of parameters, which is characterized by a not smooth function h . As reported in [15], under these conditions the system shows oscillating values of auxin concentration in each cell.

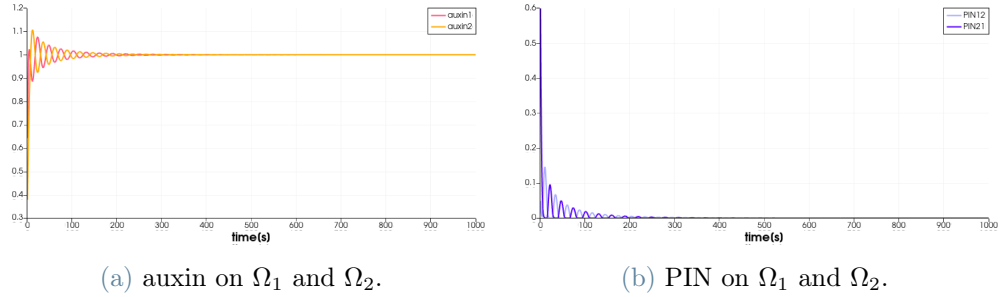


Figure 4.7: auxin-PIN dynamics on 2 cells system with the F6 $\rho = 2$ parameters set.

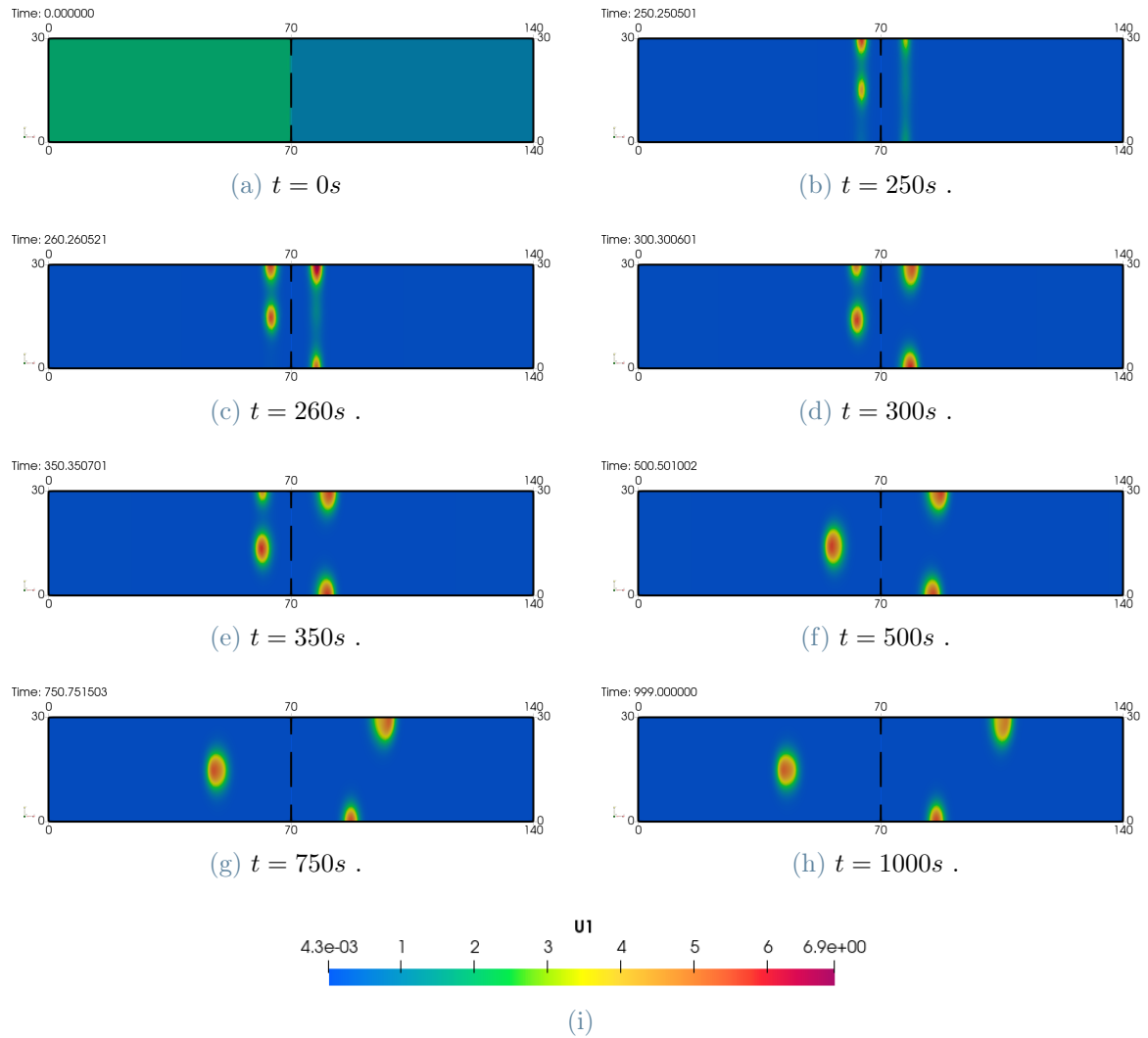


Figure 4.8: Active ROPs u evolution with RR algorithm solver on 2 cells system coupled with auxin-PIN dynamics, with the F6 $\rho = 2$ parameters set.

In Figure 4.7, we can show results for $\rho = 2$: auxin values in the first and second cell

oscillate around a common mean value, alternating with different values up to a steady state with $a_1 = a_2 = 1$. The continuous changing in auxin levels between the two cells at the beginning and the subsequent convergence to a sufficient high value lead to an interesting pattern formation.

As Figure 4.8 shows, two stripes arise close to the interface, one inside each cell, which then break into multiple spots, then slowly travel away from the common interface. Since the pattern formation takes place near the boundary dividing the two cells, the possible responsible of patches are either the gradient of auxin induced by the jump in concentrations or the gradient of ROPs generated by openend channels. Moreover, the jump in auxin levels at each time step generates a too soft gradient in auxin distribution in the two cells system, because the oscillations are rapid and have small amplitude.

Using parameter $\rho = 2.3$, the oscillations of auxin concentration become periodic, as illustrated in Figure 4.9, and the overall auxin levels in each cell range around 1 taking values approximately in the interval $[0.8; 1.2]$.

This high frequency oscillations in auxin dynamics are not replicated by the ROPs system, which is instead characterized by a slower evolution and inertia in changing conformation. We can clearly recognize from the simulation frames in Figure 4.10 that active ROPs flow from the left cell to the right one through the open channels and then two symmetric spots are formed one in each cell moving towards the exterior.

A similar behaviour can be observed in Figure 4.12 for a system under the F6 set of parameter with $\rho = 2.7$. Oscillations in Figure 4.11 have a higher frequency and amplitude than the ones obtained with $\rho = 2$ or $\rho = 2.3$ (compare Figure 4.11 with Figures 4.7 and 4.9). The local auxin concentrations change in a slightly bigger range, approximately taking values in $[0.6; 1.4]$ around 1. Since we do not observe sensible difference in pattern location we assume that the main responsible for it is again the ROPs gradient between channels.

We present other simulations, in order to validate the idea that in the new multi-cellular system the responsible for ROPs pattern formation can be also the channels of communication and not only the imposed auxin gradient.

We test if ROPs system is sensitive to high frequency auxin concentrations as those in Figure 4.9, in order to verify if auxin gradient generated is detected by ROPs patterning. We modify algorithm in 4.1. The ROPs system is solved updating k_{20} parameter with auxin concentrations found with auxin-PIN system only up to $t = 500s$. After this time, we set a constant value for the overall auxin level such that it is equal to the mean value

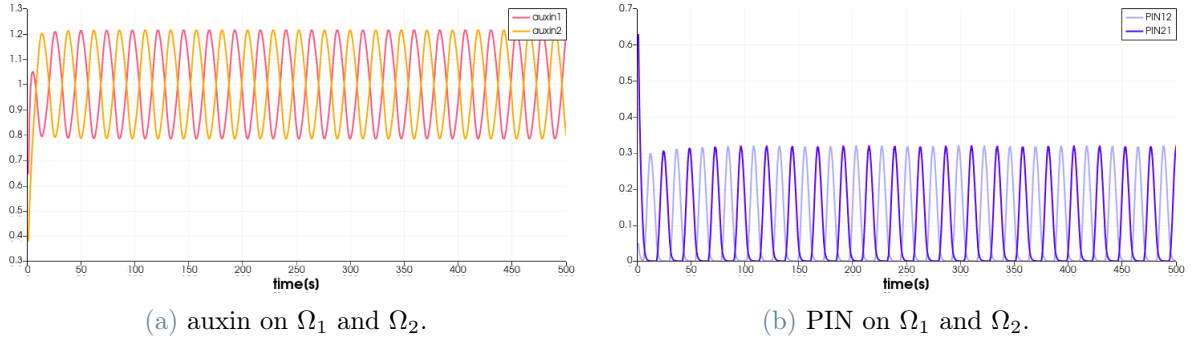


Figure 4.9: auxin-PIN dynamics on 2 cells system with the F6 $\rho = 2.3$ parameters set.

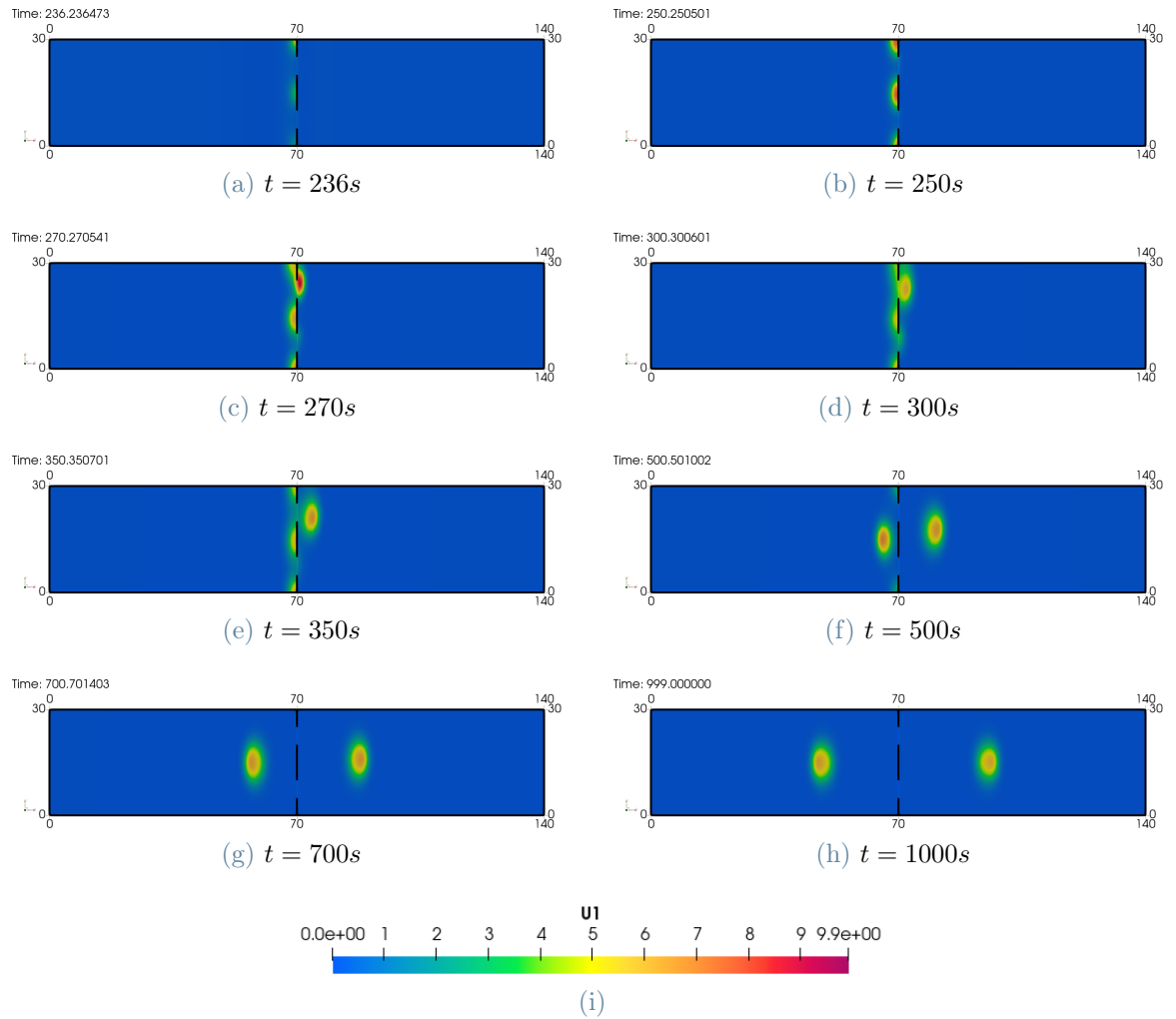


Figure 4.10: Active ROPs u evolution with RR algorithm solver on 2 cells system coupled with auxin-PIN dynamics, with the F6 $\rho = 2.3$ parameters set.

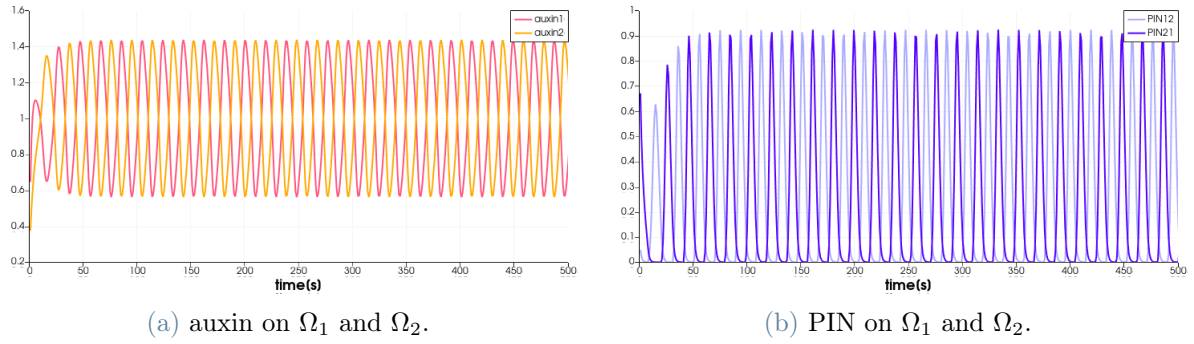


Figure 4.11: auxin-PIN dynamics on 2 cells system with the F6 $\rho = 2.7$ parameters set.

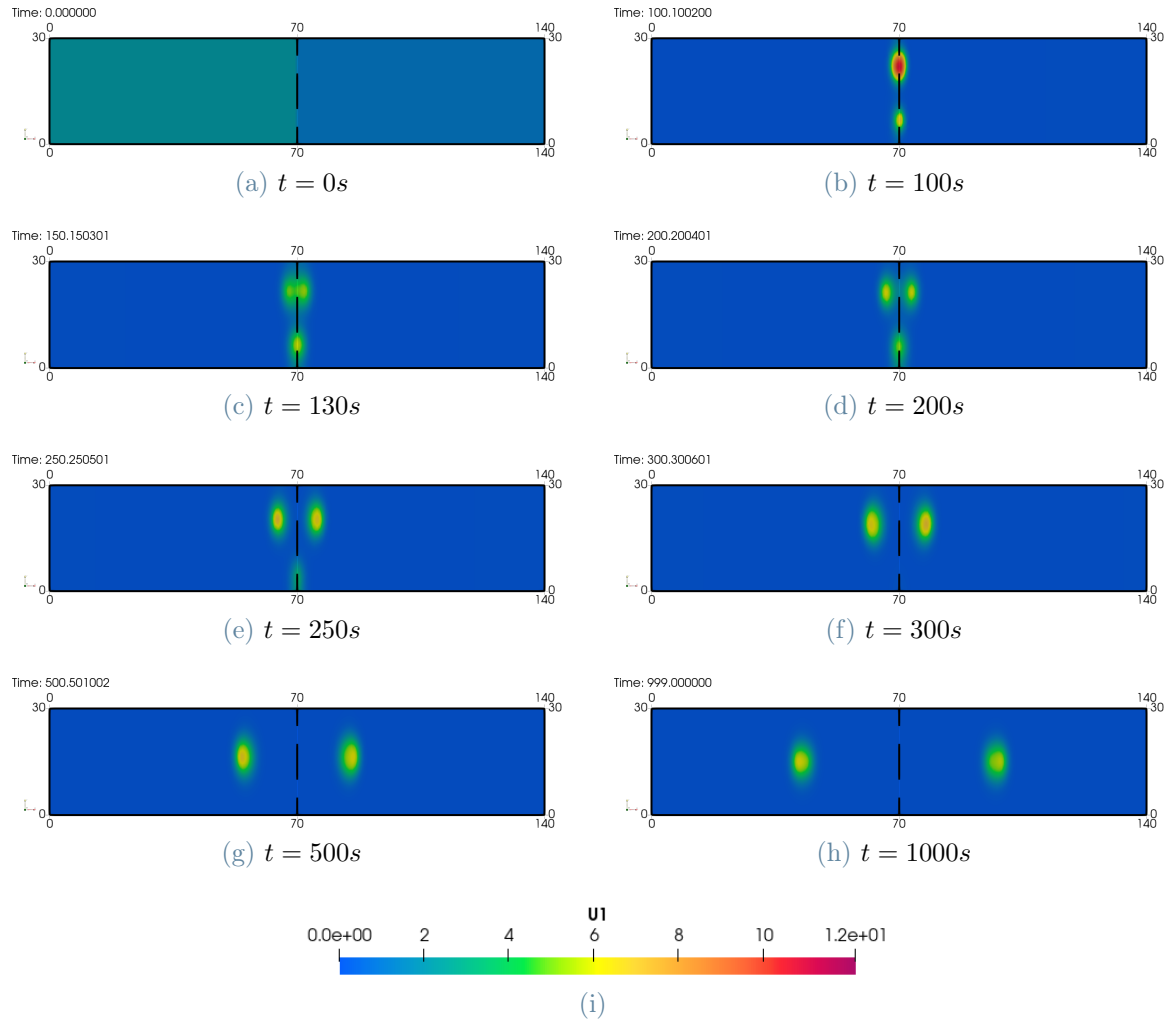


Figure 4.12: Active ROPs u evolution with RR algorithm solver on 2 cells system coupled with auxin-PIN dynamics, with the F6 $\rho = 2.7$ parameters set.

auxin concentrations oscillate around. To sum up, k_{20} is chosen as follows:

$$k_{20} = a_i \quad \forall i = 1, 2 \quad \text{if } t < 500s$$

$$k_{20} = \bar{a}_1 = \bar{a}_2 = 1 \quad \text{if } t > 500s.$$

In Figure 4.13 the results of this test are shown. We do not observe a sensible difference with respect to the frames in Figure 4.10. As a consequence, we can assume that auxin concentrations in the two cells oscillate too rapidly to be considered as a gradient responsible for hotspots generation.

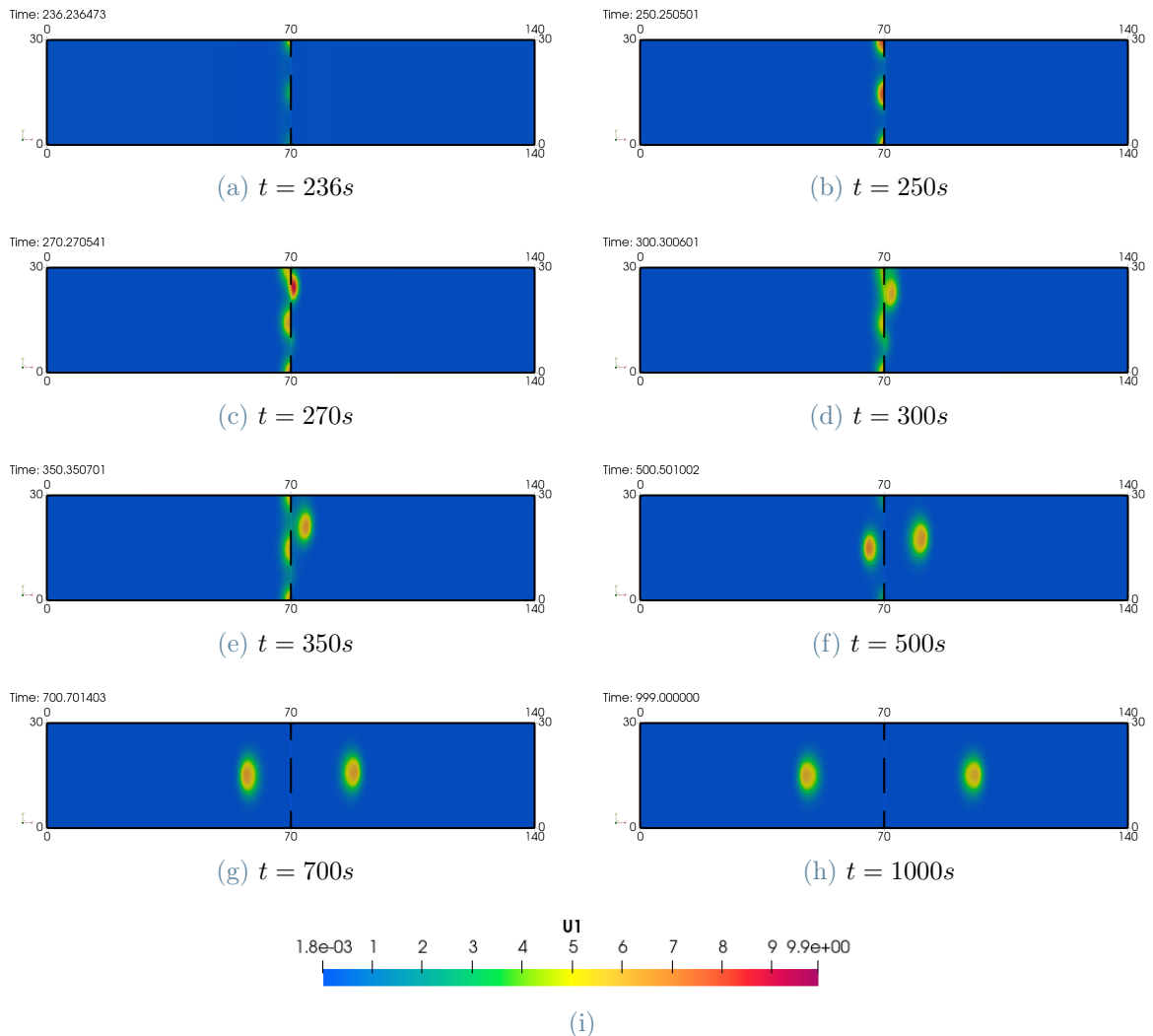


Figure 4.13: Active ROPs u evolution with RR algorithm solver on 2 cells system coupled with auxin-PIN dynamics, with the F6 $\rho = 2.3$ parameters set up to $t = 500s$, then auxin constant.

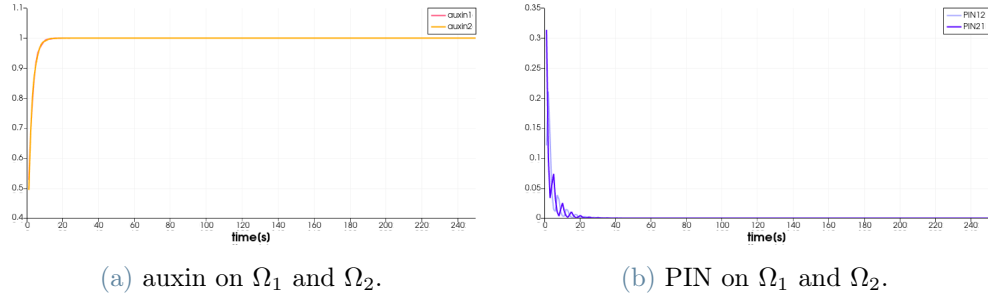


Figure 4.14: auxin-PIN dynamics on 2 cells system with the F7 $\rho = 2.8$ parameters set.

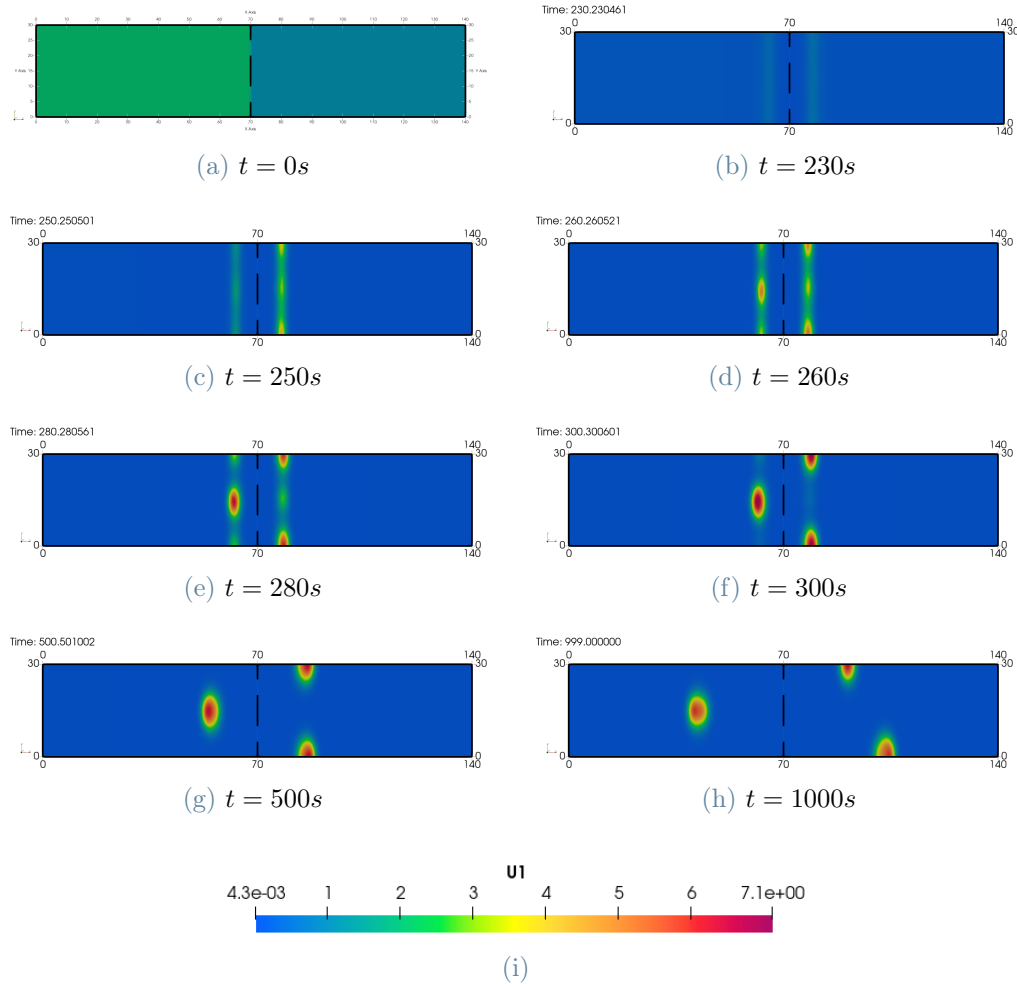


Figure 4.15: Active ROPs u evolution with RR algorithm solver on 2 cells system coupled with auxin-PIN dynamics, with the F7 $\rho = 2.8$ parameters set.

For the F6 set of parameters, ROPs system behaves as if auxin dynamics and therefore auxin gradient is absent. Too frequent changes in auxin are not registered by ROPs slow

evolution because the time-scale characterizing pattern formation of ROPs belongs to a different order than auxin frequency. The results using the F6 parameters set prove that ROPs spots can be self-generated by ROPs' flux through cells under sufficient high values of auxin.

The auxin-PIN transport dynamics under set the F7 of parameters shows almost no oscillations in the values of auxin concentrations from the beginning (see Figure 4.14a).

Results in Figure 4.15 represent another example substantiating that patches can be generated as a consequence of the structural coupling, modelled through common membrane between cells with open channels, consistently with [2, 13]. As in Figures 4.4 and 4.6, the system is characterized by no auxin gradient because auxin concentrations in the two cells soon converge to the same values. The spots therefore are self-generated by the considered multi-cellular model.

Auxin with exponential distribution

Auxin distribution is now taken space-dependent similarly as done in Section 3.3. The overall auxin level k_{20} is set equal to the auxin concentration computed with auxin-PIN system and then inside ROPs system auxin distribution is still taken exponential as follows:

$$\alpha(x) = k_{20} \exp\left(-\nu \frac{x}{L_x}\right), \text{ with } \nu = 1.5.$$

We present in Figure 4.16 results obtained under the set F6 of parameters and $\rho = 2.3$.

Numerical illustrations in Figure 4.16 visualize a double location of active ROPs because of the double source of gradient in auxin distribution. Indeed, on the left side of cell 1 we recognize the influence of the exponential distribution: a homoclinic stripe is formed, then it breaks into two spots that after a longer time unify in an unique one moving towards the right. Focusing instead on the interface, spots are formed and we observe a different evolution of patches with respect to the ones in Figure 4.10 is observed. There, the jump in k_{20} occurs and the difference in auxin concentration between cells is increased by the exponential distribution. Moreover, channels are open and ROPs flux cooperates in the pattern formation.

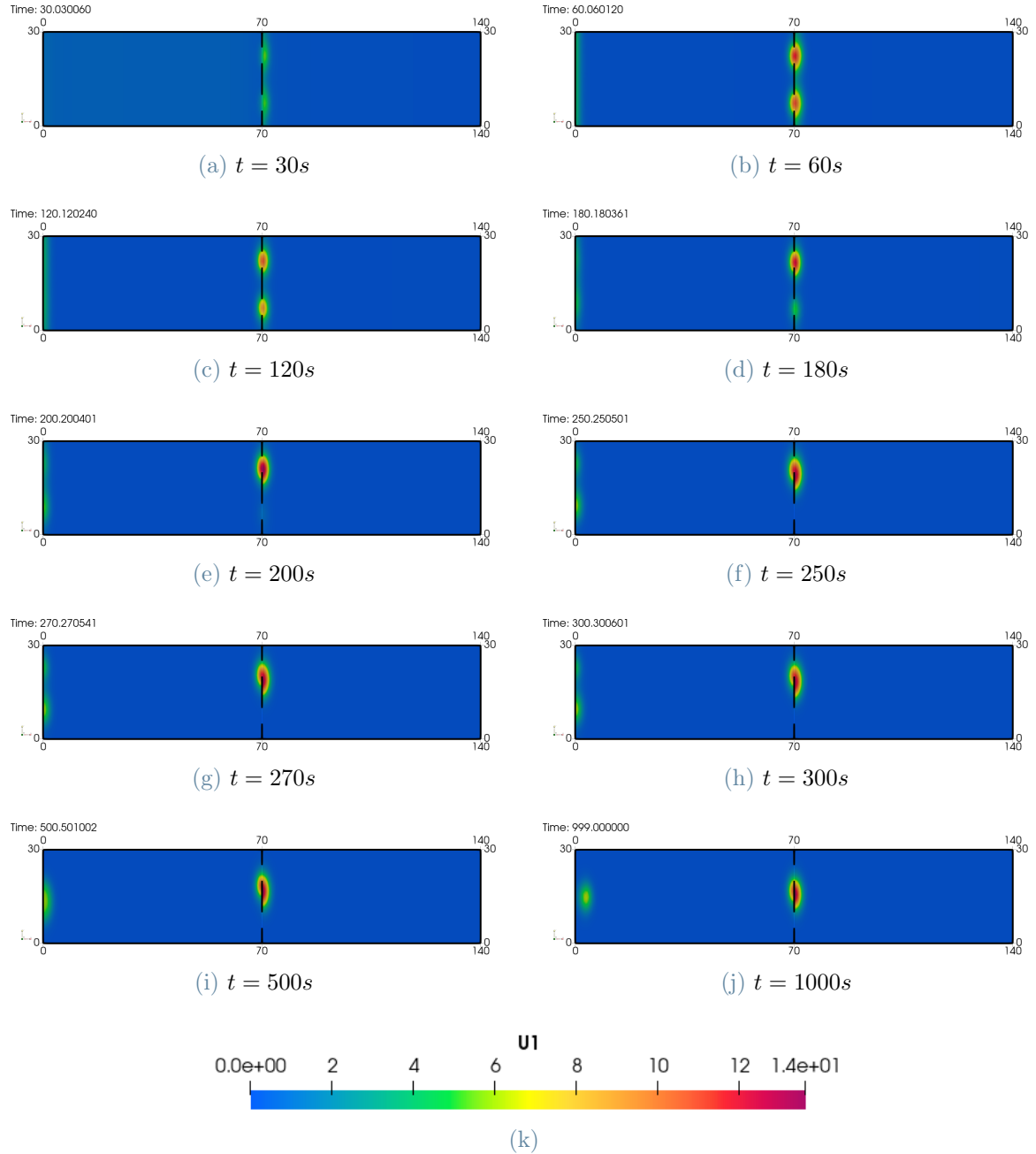


Figure 4.16: Active ROPs u evolution with RR algorithm solver on 2 cells system coupled with auxin-PIN dynamics, with the F6 $\rho = 2.3$ parameters set and exponential auxin distribution.

Change channel characterization

We here present an interesting result sustaining the modelling assumptions made on channels functions. We set the system under the set F6 of parameters and $\rho = 2$, using a bigger transport efficiency coefficient $\alpha_{u,vRR} = 5$. In Figure 4.17 different frames of the numerical

simulation obtained are shown.

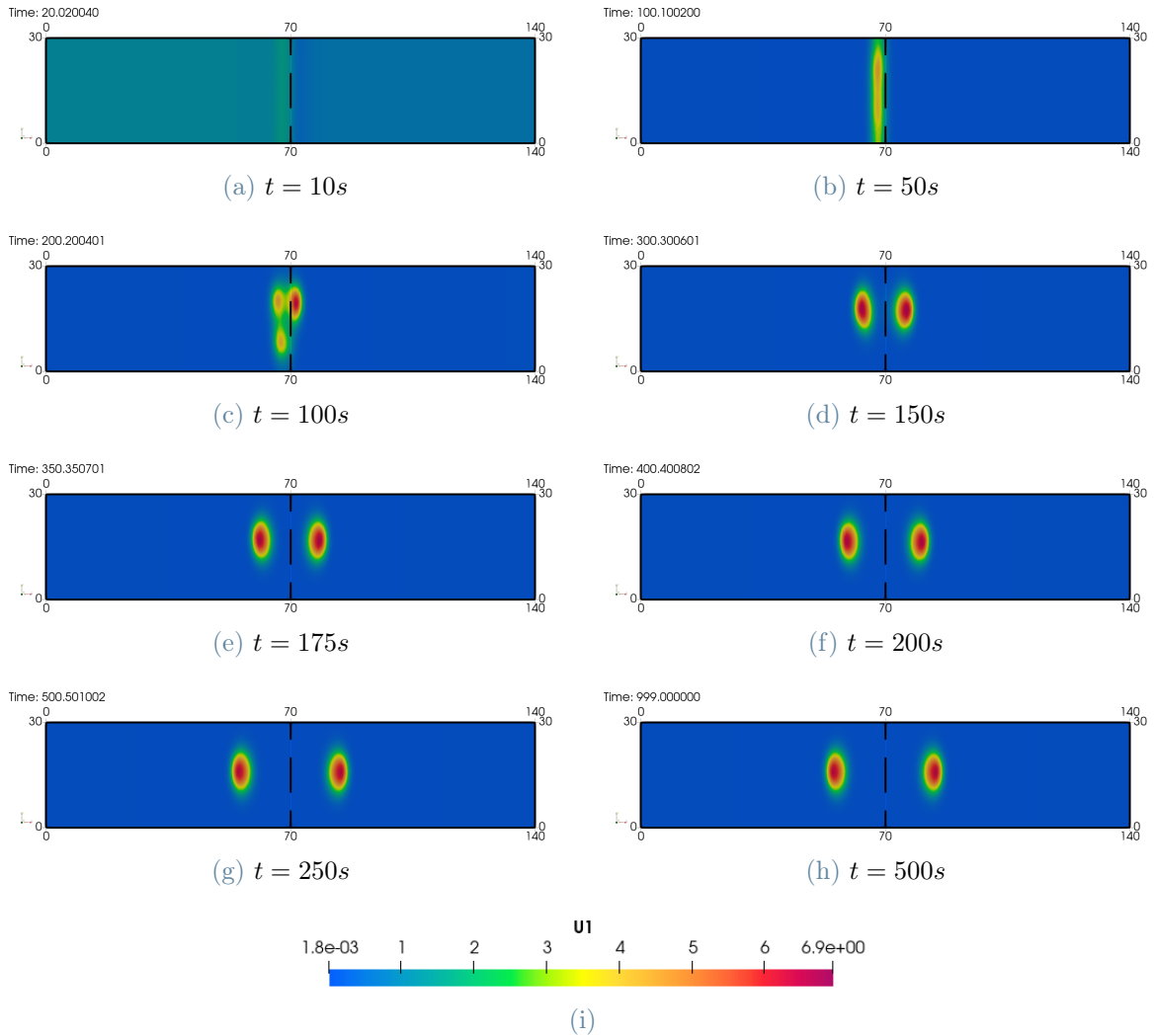


Figure 4.17: Active ROPs u evolution with RR algorithm solver on 2 cells system coupled with auxin-PIN dynamics, with the F6 $\rho = 2$ parameters set and $\alpha_{u,vRR} = 5$.

The increase in the transport efficiency yields a unique thicker stripe, in contrast to the two stripes in Figure 4.8 obtained for $\alpha_{u,vRR} = 1$, and more symmetric spots with respect to the common interface.

The result we finally show is obtained with no open communication channels, i.e., setting functions $\beta_{uRR} = \beta_{vRR} = 0$.

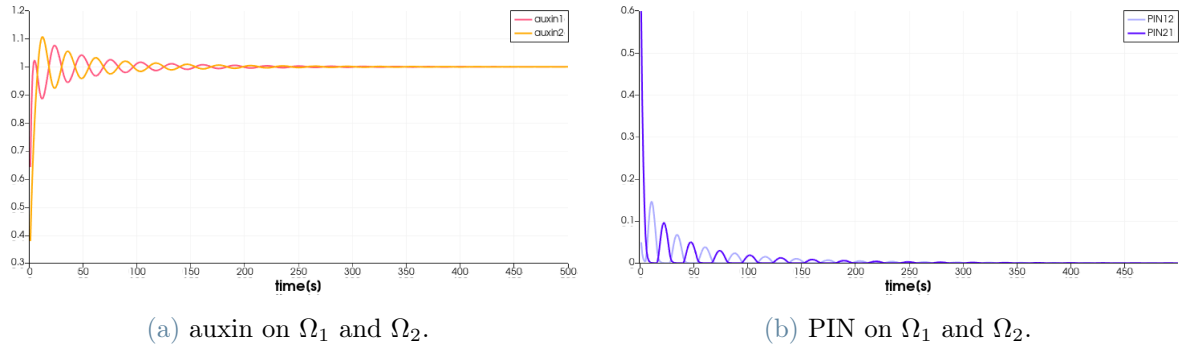


Figure 4.18: auxin-PIN dynamics on 2 cells system with the F7 $\rho = 2$ parameters set and $\beta_{uRR} = \beta_{vRR} = 0$.

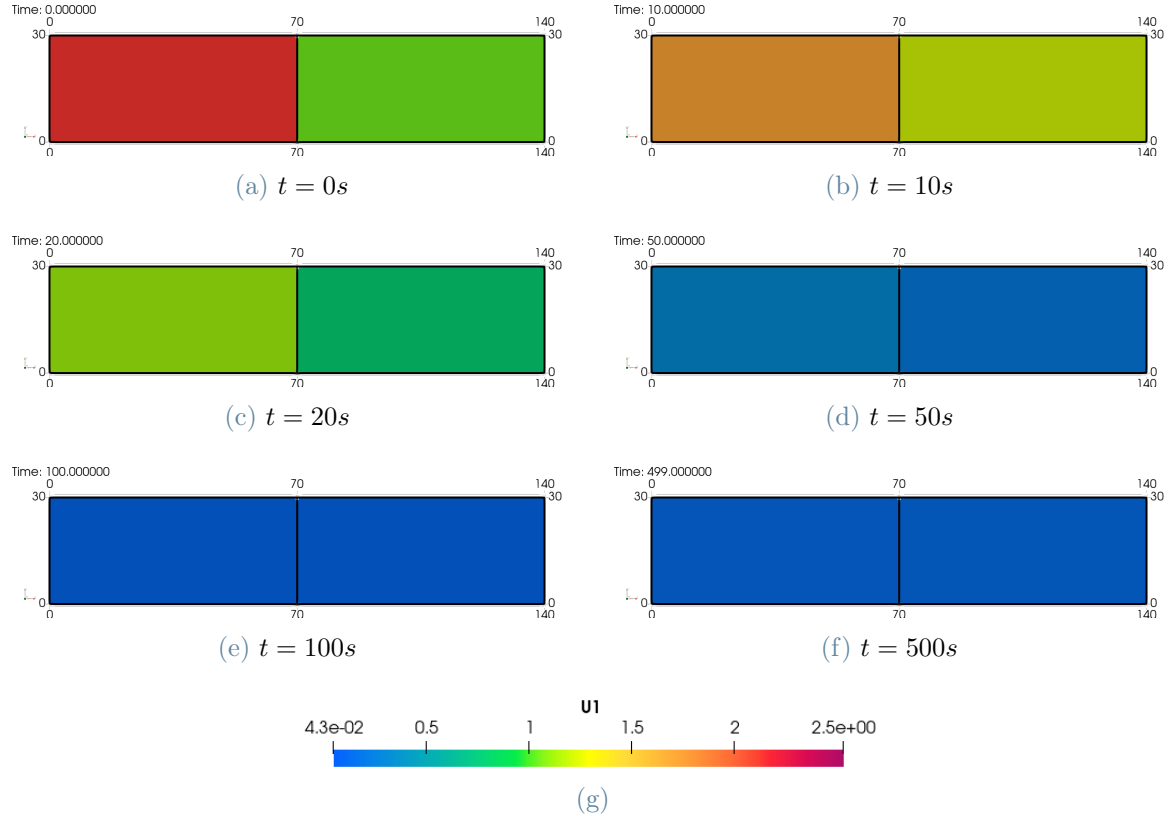


Figure 4.19: Active ROPs u evolution with RR algorithm solver on 2 cells system coupled with auxin-PIN dynamics, with the F6 $\rho = 2$ parameters set and no communicating channels ($\beta_{uRR} = \beta_{vRR} = 0$).

Though under initially oscillating values of auxin concentration and then constant high auxin level as shown in Figure 4.18, no pattern in active ROPs is formed. Jumps of auxin levels generates a gradient in the distribution in the two cell system, but locally inside each

cell auxin is still constant and no-flux boundary conditions between the cells correspond to solve the two cells separately, as if they do not belong to the same multi-cellular system.

The comparison between the pattern in Figure 4.19 and the ones obtained with open channels in Figure 4.8 is one of the most interesting result of the multi-cellular system coupled with auxin-PIN dynamics. Indeed, it confirms that responsible for spot generation can be not only auxin distribution but also the strucutral communication between cells. Setting no-flux boundary condition between cells, the system evolves to a null homogeneus active ROPs distribution. Therefore, this test validate that the main responsible for pattern formation in simulation presented in Figure 4.8 is the modelled open channels between cells.

Oscillations of auxin concentrations in a row of cells are not a bad approximation of the organization of root tissues [15] and the plot in Figure 4.18 present a physically reasonable behaviour of auxin distribution in a multi-cellular system. A null homogeneous active ROPs concentration as in Figure 4.19 is not what is expected from a physical intra-cellular model of ROPs dynamics under sufficiently high values of auxin. As a consequence, in order to have a complete, reliable spatially-extended model for root-hair initiation, it is necessary to consider structural communication between cells. The first attempt of communication modelling developed in this thesis is an interesting and valuable approach because of similarities between pattern observed in previously presented results and those in other works [13].

We present in Table 4.2 a scheme of the results in order to give to the reader an overview of the motivations and main conclusions of each test presented in Chapter 4.

Table summarizing presented results

Experiment	Motivations	Main conclusions	Figures
E1	Simulate auxin-PIN transport with different set of parameters	Confirm reliability of the semi-implicit method	4.3 - 4.5 - 4.7 - 4.9 - 4.11 - 4.14
E2	Simulate ROPs system with 2 cells array	Confirm gradient and channels influence	4.2
E3 - ROPs & auxin-PIN	Simulated different parameters sets F4, F5 and F7	Responsible for spot fomation is the structural multi-cellular modeling	4.4 - 4.6 - 4.15
E4 - ROPs & auxin-PIN	Simulated parameters set F6 under different ρ	Too rapid oscillations do not generate an auxin gradient relevant for spot fomation	4.8 - 4.10 - 4.12 - 4.13
E5 - ROPs & auxin-PIN	Simulated parameters set F6 da capire se mettere	Too rapid oscillations do not generate an auxin gradient relevant for spot fomation	4.8 -
E6 - ROPs & auxin-PIN	Consider exponential distribution of auxin inside the cells	Double gradient influence in spot formation	4.16
E7 - ROPs & auxin-PIN	Simulate with bigger coefficient α_{RR}	Channel influence on spot appearence	4.17
E8 - ROPs & auxin-PIN	Simulate oscillating auxin with closed channels for ROP	No spot formation confirm importance of communication model	4.19

Table 4.2

5 | Codes instructions

5.1. Running codes instructions - 1cell system

We here give a brief explanation on how to run proper test and simulations with codes provided inside the repository at link <https://github.com/danieleavitable/root-simulator>. Regarding singular cell pattern formation there are implemented two main codes:

- `1cell_stationaryTest.edp`: contains steps for solving the steady state system through Newton's method described in section 2.2.1.
- `1cell_semi_implicit.edp`: contains the semi-implicit solver for the full time-dependent problem described in section 2.2.2.
- `Analysis_Semi_implicitDT.edp`: contains main code to estimate the order of convergence of our semi-implicit method used in 2.3.3.

The first one relies on the separated function `G.edp` computing G function defined in (2.10) and function `Jac` computing the corresponding Jacobian matrix defined in (2.16). The second one include instead a separated piece of code `step_semi_implicit.edp` in which are defined `varf`, corresponding type in FreeFem++ for bilinear form, matrices and `func int step` in order to solve the singular cell system.

To properly run both codes, one need to write the string identifying under which set of parameters one want to solve the system; three main sets of parameters are defined in `PRM.edp` file and each possible group of parameters correspond to the division found in table 2.1. The choice of parameter set is done as follows:

```
11 // Parameters:  
12 string prm = "Set B"; // "Set A", "Set B", "Set C"  
13 include "PRM.edp";
```

Listing 5.1: Choice of set of parameters

In addition, also the mesh has to be settled correctly according to the choice of problem to solve, commenting the not used definition of variable `Th`:

```
16 // Mesh
```

```

17 mesh Th = square(Nx, Ny, [x, y]); // "Set A", "Set B"
18 // mesh Th = square(Nx, Ny, [Lx * x, Ly * y]); // "Set C"

```

Listing 5.2: 1cell_stationaryTest.edp or 1cell_semi_implicit.edp: choice of mesh

In case "Set A" and "Set B" mesh refinement is characterized by $N_x = N_y = 60$, whereas in case "Set C" by $N_x = 100$ and $N_y = 30$.

Finally one need to properly change \tilde{c}_1 and \tilde{c}_2 according to formulas in (2.8) and (2.7):

```

16 // "Set A", "Set B"
17 func tildec1 = alpha;
18 func tildec2 = - gamma*alpha;
19 // "Set C"
20 // func tildec1 = alpha;
21 // func tildec2 = - alpha;

```

Listing 5.3: PRM.edp: setting of \tilde{c}_1 and \tilde{c}_2

Another important choice for running properly the two solvers is the initialization of the system: in the first case it is the initial guess for the equilibrium to find, in the second case it corresponds to the initial solution at time $t = 0s$ of the ROPs dynamics. Under each result shown is specified which is the initial state from which the solver start; in general one could chose between loading previous solutions setting `ld` parameter equal to 1 or alternatively set custom defined (u^0, v^0) :

```

8 int ld = 0; // 1: load prev. sol. as initial state
9 // 0: use custom initial state

```

Listing 5.4: choice for initialization

```

1 /// Initialization:
2 if (ld) {
3     ifstream fU(path + "U" + tload + ".txt");
4     ifstream fV(path + "V" + tload + ".txt");
5
6     fU >> U[];
7     fV >> V[];
8
9     plot(U, fill = 1, value = 1, cmm = "Loaded Active ROPS"/*, wait = 1*/
10        ;
11     plot(V, fill = 1, value = 1, cmm = "Loaded Inactive ROPS"/*, wait = 1
12        */);
13     U[] += pert[];
14     V[] += pert[];
15 }
16 else
17 {
18     U = u0;
19     V = v0;
20     U[] += pert[];

```

```

19 V[] += pert[];
20 // srand( seed );
21 // // ranreal 1 generates a random number in [0,1]
22 // for( int ii = 0; ii < Xh.ndof; ii++ )
23 // {
24 //     U[] [ii] += randreal1() / 3e5;
25 //     V[] [ii] += randreal1() / 3e5;
26 // }
27 }
```

Inside `run.sh` bash file, one need to specify the main to run with `FreeFem++` changing properly `EXEC` variable. Executing this file, the script creates a new folder in `results` directory named with the current date and time, it runs the specified main and saves all the output in `output.txt`. This file together with code files in `.edp` format and solutions files in `.ps`, `.vtk`, `.txt` format are moved inside the directory named with the current date and time, in the corresponding directories `code`, `U` and `V`.

5.2. Running codes instructions - 2 and 4 cells systems

In order to simulate the previously formulated algorithm for a pluricellular system has been written three main codes:

- `2cell_RR.edp`: this main code solves a two cells system with a classic Robin-Robin iterative algorithm, as formulated in sec. 3.2.2.
- `2cell_RRmod.edp`: this main code solves a two cells system with the modified Robin-Robin algorithm described in sec. 3.2.3.
- `4cell_RRmod.edp`: this main code solves a four cells system with the modified Robin-Robin algorithm.

For pluricellular systems solver the setting rules for parameters described in sec. (5.1) are still true, excepting those regarding mesh initialization. Indeed, depending on the system to solve, the mesh is properly defined. For example, in a two cells pluricellular system can be defined two possible type of mesh:

```

24 // 1st type of mesh
25 border o1(t=Ly*2, 0){x=0; y=t; label=outside;};
26 border o2(t=0, Lx){x=t; y=0; label=outside;};
27 border o3(t=0, 2*Ly){x=Lx; y=t; label=outside;};
28 border o4(t=0, Lx){x=Lx-t; y=2*Ly; label=outside;};
29 border i1(t=0, Lx){x=Lx - t; y=Ly; label=inside;};
30 mesh TH = buildmesh(o1(2*Ny) + o2(Nx) + o3(2*Ny) + o4(Nx) + i1(Nx));
```

```

32 reg(0) = TH(Lx/2, Ly - 2).region;
33 reg(1) = TH(Lx/2, Ly + 2).region;
34
35 for(int i = 0; i < N; i++) Th[i] = trunc(TH, region==reg(i));
36
37 // 2nd type of mesh
38 border o1(t=Ly, 0){x=0; y=t; label=outside;};
39 border o2(t=0, 2 * Lx){x=t; y=0; label=outside;};
40 border o3(t=0, Ly){x=2*Lx; y=t; label=outside;};
41 border o4(t=0, 2*Lx){x=2*Lx-t; y=Ly; label=outside;};
42 border i1(t=0, Ly){x=Lx; y=Ly-t; label=inside;};
43 mesh TH = buildmesh(o1(Ny) + o2(2*Nx) + o3(Ny) + o4(2*Nx) + i1(Ny));
44
45 reg(0) = TH(Lx - 2, Ly/2).region;
46 reg(1) = TH(Lx + 2, Ly/2).region;
47
48 for(int i = 0; i < N; i++) Th[i] = trunc(TH, region==reg(i));

```

Listing 5.5: 2cell_RRmod.edp: choice of mesh

Bilinear forms characterizing the mathematical formulation are collected in `varf_2cell.edp` and `varf_ncell.edp` files. Inside `varf` `duidn` for 2 cells system and `duidnj` for 4 cells system one can pass from original Robin-Robin contribute, to not-parallelizable or parallelizable contribute for Robin-Robin modified commenting the right lines specified. (vd. commenti a lato)

Matrices and vectors reassembling procedures for each sub-domain are defined in `assemble_RR`. Here is necessary to comment the alternatives of `if-else` cycle not used for the pluricellular system under study.

Last important file included in the main for model definition is `channelPRM.edp`, where parameters $\alpha_{u/vRR}$ and $\beta_{u/vRR}$ used in our new model to represents communication channels between cells have to be properly settled, together with convergence criterion parameters for the algorithm used:

- `toll` represents the tolerance of the normalized residual desired.
- `Niter` represents the maximum number of iterations allowed in case tolerance is not reached.

6 | Conclusions and future developments

In this thesis we developed a multi-cellular model accounting for a spatially-extended intra-cellular system for ROPs pattern formation. In the proposed framework, we solved ROPs pattern formation in a system composed by multiple cells, together with a transport model for hormone auxin. The RD model explains the auxin-mediated action of ROPs in an *Arabidopsis* root hair cell leading to formation of the localized patches of activated ROPs.

Our simulations support conclusions reached in other works regarding ROPs dynamics under a-priori defined auxin distribution [2, 13, 14]. We have analyzed various scenarios such that a stripe-like patch forms where auxin concentration is higher. Then, instability of stripe into spot-like states occurs and multiple spots align with auxin gradient or travel towards auxin minimum. Several results confirm that, for a transversally independent gradient, lateral stripes become unstable states.

Successively as a new contribution, we extended the intra-cellular dynamics for root-hair initiation model to a multi-cellular system, developing a new model taking into account communication between cells. In order to do so, we have defined a boundary value problem which assumes new boundary conditions between neighboring cells. Subsequently, we develop an iterative procedure to solve it. We take as reference scheme a Robin-Robin domain decomposition method. We impose fluxes of ROPs between neighboring cells, depending on the difference of the ROPs concentrations, through localised open channels. Such connections are tuned in order to visualize considerably different results with respect to a configuration characterized by stagnant cells. In addition, we aim at preserving all previous analyses over important parameters characterizing the system. We numerically assessed the robustness of the proposed model in cooperating with auxin distribution in influencing ROPs pattern formation.

Having defined a reliable multi-cellular model, we have taken into account also auxin concentration dynamics. Hormone auxin is regulated by carriers PIN following a non-

linear ODEs system. We implement a semi-implicit method to solve such as a system on a two cells setting. The simulations we carried out show oscillating values of auxin concentration for specific sets of parameters, as expected from previous studies. A further confirmation of the robustness of pattern formation according to the proposed new multi-cellular model, when considering channel communication between cells, is given in Chapter 4. It is shown that even if the system is under steady homogeneous auxin concentrations, the model robustly forms hotspots when considering open channels under a sufficiently high overall auxin level.

The results show two ways spots of active ROPs can be generated. The first factor is the auxin gradient, which still guarantees and influence stripe to spot evolution. The second factor is the structural coupling between cells. Even if not characterized by variation in space but with a sufficiently high value of the auxin concentrations, the multi-cellular model leads the system to multiple spots.

In conclusion, this thesis provides a first attempt in modeling communication between root-hair cells in pattern formation. Future developments include to study the structural model or to deeply analyze channels characterization. Moreover, the iterative procedure implemented could be applied to a multi-cellular system composed by more than four cells and eventually try to increase the computational performance through parallel computing. Another possible road to follow is to approach the problem through homogenization techniques. The cited method may increase the efficiency in solving the model, particularly when the number of cells involved becomes large. Finally, one could assume other auxin transport models, less simplified or accounting for spatial dependence inside the cells.

Bibliography

- [1] K. Alim and E. Frey. Quantitative predictions on auxin-induced polar distribution of pin proteins during vein formation in leaves. *The European physical journal E*, March 2010.
- [2] D. Avitabile, V. F. Breña-Medina, and M. J. Ward. Spot dynamics in a reaction-diffusion model of plant root hair initiation. *SIAM Journal on Applied Mathematics*, 78(1):291–319, 2018.
- [3] S. Badia, F. Nobile, and C. Vergara. Fluid–structure partitioned procedures based on robin transmission conditions. *Journal of Computational Physics*, 227(14):7027–7051, 2008.
- [4] L. R. Band, J. A. Fozard, C. Godin, O. E. Jensen, T. Pridmore, M. J. Bennett, and J. R. King. Multiscale systems analysis of root growth and development: Modeling beyond the network and cellular scales. *The Plant Cell*, 24(10):3892–3906, 10 2012. ISSN 1040-4651. doi: 10.1105/tpc.112.101550. URL <https://doi.org/10.1105/tpc.112.101550>.
- [5] P. Benfey and B. Scheres. Root development. *Curr Biol*, 10:R813–5, Nov 2000. doi: 10.1016/s0960-9822(00)00814-9.
- [6] I. Blilou, J. Xu, M. Wildwater, V. Willemse, I. Paponov, J. Friml, R. Heidstra, M. Aida, K. Palme, and B. Scheres. The pin auxin efflux facilitator network controls growth and patterning in arabidopsis roots. *Nature*, 433(7021):39–44, 2005. ISSN 1476-4687. doi: 10.1038/nature03184.
- [7] V. Breña-Medina, A. R. Champneys, C. Grierson, and M. J. Ward. Mathematical modeling of plant root hair initiation: Dynamics of localized patches. *SIAM Journal on Applied Dynamical Systems*, 13(1):210–248, 2014.
- [8] X. R. Bustelo, V. Sauzeau, and I. M. Berenjeno. Gtp-binding proteins of the rho/rac family: regulation, effectors and functions in vivo. *Bioessays*, 29(4):356–370, 2007.
- [9] J. Chaiwanon and Z.-Y. Wang. Spatiotemporal brassinosteroid signaling and an-

- tagonism with auxin pattern stem cell dynamics in arabidopsis roots. *Current Biology*, 25(8):1031–1042, 2015. ISSN 0960-9822. doi: <https://doi.org/10.1016/j.cub.2015.02.046>. URL <https://www.sciencedirect.com/science/article/pii/S0960982215002158>.
- [10] R. Dello Ioio, F. S. Linhares, E. Scacchi, E. Casamitjana-Martinez, R. Heidstra, P. Costantino, and S. Sabatini. Cytokinins determine arabidopsis root-meristem size by controlling cell differentiation. *Current Biology*, 17(8):678–682, 2007. ISSN 0960-9822. doi: <https://doi.org/10.1016/j.cub.2007.02.047>. URL <https://www.sciencedirect.com/science/article/pii/S0960982207010561>.
- [11] A. Doelman and H. van der Ploeg. Homoclinic stripe patterns. *SIAM Journal on Applied Dynamical Systems*, 1(1):65–104, 2002.
- [12] C. Duckett, C. Grierson, P. Linstead, K. Schneider, E. Lawson, C. Dean, S. Poethig, and K. Roberts. Clonal relationships and cell patterning in the root epidermis of arabidopsis. *Development*, 120(9):2465–2474, 1994.
- [13] V. F. Breña-Medina. *Modelling Initiation of Plant Root Hairs*. PhD thesis, University of Bristol, June 2013.
- [14] V. F. Breña-Medina, D. Avitabile, A. R. Champneys, and M. J. Ward. Stripe to spot transition in a plant root hair initiation model. *SIAM Journal on Applied Mathematics*, 75(3):1090–1119, Jan 2015. ISSN 1095-712X. doi: 10.1137/140964527. URL <http://dx.doi.org/10.1137/140964527>.
- [15] E. Farcot and Y. Yuan. Homogeneous auxin steady states and spontaneous oscillations in flux-based auxin transport models. *SIAM J. Applied Dynamical systems*, 12(3):1330—1353, May 2013.
- [16] L. Gerardo-Giorda, F. Nobile, and C. Vergara. Analysis and optimization of robin–robin partitioned procedures in fluid–structure interaction problems. *SIAM Journal on Numerical Analysis*, 48(6):2091–2116, 2010. doi: 10.1137/09076605X. URL <https://doi.org/10.1137/09076605X>.
- [17] G. Gigante and C. Vergara. On the choice of interface parameters in robin–robin loosely coupled schemes for fluid–structure interaction. *Fluids*, 6(6):213, 2021.
- [18] V. A. Grieneisen, J. Xu, A. F. Marée, P. Hogeweg, and B. Scheres. Auxin transport is sufficient to generate a maximum and gradient guiding root growth. *Nature*, 449(7165):1008–1013, 2007.

- [19] C. Grierson and J. Schiefelbein. *The Arabidopsis Book*. American Society of Plant Biologists, 2002.
- [20] F. Hecht. New development in freefem++. *Journal of Numerical Mathematics*, 20(3-4):251–265, 2012. ISSN 1570-2820. URL <https://freefem.org/>.
- [21] J. Hou, W. Yan, D. Hu, and Z. He. Robin-robin domain decomposition methods for the dual-porosity-conduit system. *Advances in Computational Mathematics*, 47(1):1–33, 2021.
- [22] R. D. Ioio, K. Nakamura, L. Moubayidin, S. Perilli, M. Taniguchi, M. T. Morita, T. Aoyama, P. Costantino, and S. Sabatini. A genetic framework for the control of cell division and differentiation in the root meristem. *Science*, 322(5906):1380–1384, 2008. doi: 10.1126/science.1164147. URL <https://www.science.org/doi/abs/10.1126/science.1164147>.
- [23] A. Jilkine, A. F. Marée, and L. Edelstein-Keshet. Mathematical model for spatial segregation of the rho-family gtpases based on inhibitory crosstalk. *Bulletin of mathematical biology*, 69(6):1943–1978, 2007.
- [24] A. Jones, E. Kramer, K. Knox, R. Swarup, M. Bennett., C. Lazary, H. Leyser, and C. Grierson. Auxin transport through non-hair cells sustains root-hair development. *Nat. Cell. Biol.*, 11(1):78–84, January 2009.
- [25] M. A. Jones, J.-J. Shen, Y. Fu, H. Li, Z. Yang, and C. S. Grierson. The arabidopsis rop2 gtpase is a positive regulator of both root hair initiation and tip growth. *The Plant cell*, 14:763–76, Apr 2002.
- [26] T. Kolokolnikov, W. Sun, M. Ward, and J. Wei. The stability of a stripe for the gierer–meinhardt model and the effect of saturation. *SIAM Journal on Applied Dynamical Systems*, 5(2):313–363, 2006. doi: 10.1137/050635080. URL <https://doi.org/10.1137/050635080>.
- [27] T. Kolokolnikov, M. J. Ward, and J. Wei. Spot self-replication and dynamics for the schnakenburg model in a two-dimensional domain. *Journal of nonlinear science*, 19(1):1–56, 2009.
- [28] P. Krupinski and H. Jönsson. Modeling auxin-regulated development. *Cold Spring Harbor perspectives in biology*, 2(2):a001560, 2010.
- [29] P. Krupinski, B. Bozorg, A. Larsson, S. Pietra, M. Grebe, and H. Jönsson. A model analysis of mechanisms for radial microtubular patterns at root hair initiation sites. *Frontiers in plant science*, 7, October 2016. doi: 10.3389/fpls.2016.01560.

- [30] A. Lander. Pattern, growth, and control. *Cell*, 144(6):955–969, 2011.
- [31] R. D. Mambroa, M. D. Ruvoa, E. Pacificia, E. Salvia, R. Sozzanid, P. N. Benfeye, W. Busch, O. Novakh, K. Ljungh, L. D. Paolab, A. F. M. Maréec, P. Costantinoa, V. A. Grieneisenc, and S. Sabatini. Auxin minimum triggers the developmental switch from cell division to cell differentiation in the arabidopsis root. *Proceedings of the National Academy of Sciences of the United States of America*, June 2017.
- [32] V. V. Mironova, N. A. Omelyanchuk, G. Yosiphon, S. I. Fadeev, N. A. Kolchanov, E. Mjolsness, and V. A. Likhoshvai. A plausible mechanism for auxin patterning along the developing root. *BMC systems biology*, 4(1):1–19, 2010.
- [33] Y. Mori, A. Jilkine, and L. Edelstein-Keshet. Wave-pinning and cell polarity from a bistable reaction-diffusion system. *Biophysical journal*, 94(9):3684–3697, 2008.
- [34] S. Nagawa, T. Xu, and Z. Yang. Rho gtpase in plants: conservation and invention of regulators and effectors. *Small GTPases*, 1(2):78–88, 2010.
- [35] R. Payne and C. Grierson. A theoretical model for rop localisation by auxin in arabidopsis root hair cells. *PLoS ONE*, 4(12):e8337, December 2009. URL <https://doi.org/10.1371/journal.pone.0008337>.
- [36] R. G. Plaza, F. Sanchez-Garduno, P. Padilla, R. A. Barrio, and P. K. Maini. The effect of growth and curvature on pattern formation. *Journal of Dynamics and Differential Equations*, 16(4):1093–1121, 2004.
- [37] A. Quarteroni and A. Valli. *Domain decomposition methods for partial differential equations*. Oxford University Press, 1999.
- [38] A. Quarteroni, R. Sacco, and F. Saleri. *Numerical Mathematics*, volume 37. 01 2007. ISBN 978-1-4757-7394-1. doi: 10.1007/b98885.
- [39] D. Reinhardt, E.-R. Pesce, P. Stieger, T. Mandel, K. Baltensperger, M. Bennett, J. Traas, J. Friml, and C. Kuhlemeier. Regulation of phyllotaxis by polar auxin transport. *Nature*, 426(6964):255–260, 2003.
- [40] R. W. Ridge and A. M. C. Emons. *Root Hairs: cell and molecular biology*. Springer Science & Business Media, 2012.
- [41] S. Rigas, G. Debrosses, K. Haralampidis, F. Vicente-Agullo, K. A. Feldmann, A. Grabov, L. Dolan, and P. Hatzopoulos. Trh1 encodes a potassium transporter required for tip growth in arabidopsis root hairs. *The Plant Cell*, 13(1):139–151, 2001.

- [42] S. Sabatini, D. Beis, H. Wolkenfelt, J. Murfett, T. Guilfoyle, J. Malamy, P. Benfey, O. Leyser, N. Bechtold, P. Weisbeek, et al. An auxin-dependent distal organizer of pattern and polarity in the arabidopsis root. *Cell*, 99(5):463–472, 1999.
- [43] P. Sahlin, B. Söderberg, and H. Jönsson. Regulated transport as a mechanism for pattern generation: capabilities for phyllotaxis and beyond. *Journal of theoretical biology*, 258(1):60–70, 2009.
- [44] M. Sauer, J. Balla, C. Luschnig, J. Wiśniewska, V. Reinöhl, J. Friml, and E. Benková. Canalization of auxin flow by aux/iaa-arf-dependent feedback regulation of pin polarity. *Genes & development*, 20(20):2902–2911, 2006.
- [45] J. Schnakenberg. Simple chemical reaction systems with limit cycle behaviour. *Journal of Theoretical Biology*, 81(3):389–400, 1979. ISSN 0022-5193. doi: [https://doi.org/10.1016/0022-5193\(79\)90042-0](https://doi.org/10.1016/0022-5193(79)90042-0). URL <https://www.sciencedirect.com/science/article/pii/0022519379900420>.
- [46] S. Stoma, M. Lucas, J. Chopard, M. Schaedel, J. Traas, and C. Godin. Flux-based transport enhancement as a plausible unifying mechanism for auxin transport in meristem development. *PLoS computational biology*, 4(10):e1000207, 2008.
- [47] A. M. Turing. The chemical basis of morphogenesis. *Philosophical Transactions of the Royal Society of London. Series B, Biological Sciences*, 237(641):37–72, 1952. doi: [10.1098/rstb.1952.0012](https://doi.org/10.1098/rstb.1952.0012). URL <https://royalsocietypublishing.org/doi/abs/10.1098/rstb.1952.0012>.

List of Figures

1.1	Arabidopsis root scheme	2
1.2	Root-hairs initiation	3
1.3	Scheme taken from [13] of the binding process and cycling between active- and inactive- state of ROPs	5
2.1	Sketch of an idealized 3D RH cell with longitudinal and transversal spatially dependent auxin flow. Figure reproduced from [2].	12
2.2	Equilibrium of homogeneous adimentional system	24
2.3	Validation of theoretical equilibrium - $\tilde{\epsilon} = 10^{-3}$	25
2.4	Validation of theoretical equilibrium - $\tilde{\epsilon} = 10^{-2}$	25
2.5	Equilibrium for Set C	26
2.6	Maximum of active concentration ROPs over time	27
2.7	Single cell at $t = 0s$	31
2.8	Single cell at $t = 3000s$	31
2.9	1cell Active ROPs	32
3.1	Sktetch of a four cells scheme with communicating flows.	34
3.2	2cell RR modified Active ROPs - $\beta_{uRR} = \beta_{vRR} = 0$	48
3.3	Tuning channel prm - $a_x = 5$	50
3.4	Tuning channel prm - $a_x = 20$	50
3.5	Tuning channel prm - $a_x = 30$	51
3.6	Tuning channel prm - $a_x = 34$	51
3.7	Tuning channel prm - $a_x = 5, \epsilon_x = 5$	52
3.8	Tuning channel prm - $a_x = 30, \epsilon_x = 5$	53
3.9	Tuning channel prm - $a_x = 34, \alpha_{RR} = \frac{35}{2}$	54
3.10	Tuning channel prm - Smaller sparse channels	55
3.11	P vs NP mode - relevant channel	56
3.12	Modifying prm overall auxin - $k_{20} = 0.5$ vs $k_{20} = 0.4$	57
3.13	Modifying prm overall auxin - $k_{20} = 0.39$ vs $k_{20} = 0.5$	58
3.14	Modifying prm overall auxin - $k_{20} = 1.3562$	59

3.15 Not homogeneous U0- $k_{20} = 1.3562$ vs $k_{20} = 0.5$	60
3.16 RR with time dependent auxin - period $T_{pa} = 100s$	61
3.17 RR with time dependent auxin - period $T_{pa} = 200s$	62
3.18 RR with time dependent auxin - periodic $T_{pa} = 40min$	63
3.19 Time dependent prm homogeneous auxin - $k_{20} \arctan(x, t)$	64
3.20 Time dependent auxin - moving max	65
3.21 RR with time dependent auxin - moving max	66
3.22 4cell RR Active ROPs - $\beta_{RR} = 0$	67
3.23 4cell RR Active ROPs - mid gradient, no-flux BC	68
3.24 4cell RR Active ROPs - mid gradient, same initial state	69
3.25 4cell RR Active ROPs - mid gradient, different initial state	70
3.26 4cell RR Active ROPs - inverse gradient, different initial state	71
3.27 4cell RR Active ROPs - auxin time-dependent	73
4.1 Two neighboring cells with concentrations of auxin, carriers proteins and flux from i to j ; figure taken from [15].	77
4.2 2cell RR Active ROPs - with $a_y = 5, \epsilon_y = 5$	83
4.3 auxin-PIN - with the F4 set	85
4.4 2cell RR Active ROPs coupled auxin-PIN - with the F5 prm	85
4.5 auxin-PIN - with the F5 prm	86
4.6 2cell RR Active ROPs coupled auxin-PIN - with the F5 set	86
4.7 auxinPIN - with the F6 $\rho = 2$ set	87
4.8 2cell RR Active ROPs coupled auxin-PIN - with the F6 $\rho = 2$ set	87
4.9 auxin-PIN - with the F6 $\rho = 2.3$ set	89
4.10 2cell RR Active ROPs coupled auxin-PIN - with the F6 $\rho = 2.3$ set	89
4.11 auxin-PIN - with the F6 $\rho = 2.7$ set	90
4.12 2cell RR Active ROPs coupled auxin-PIN - with the F6 $\rho = 2.7$ set	90
4.13 2cell RR Active ROPs coupled auxin-PIN - with the F6 $\rho = 2.3$ set up to $t = 500s$	91
4.14 auxin-PIN - with the F7 $\rho = 2.8$ set	92
4.15 2cell RR Active ROPs coupled auxin-PIN - with the F7 $\rho = 2.8$ set	92
4.16 2cell RR Active ROPs coupled auxin-PIN - with the F6 $\rho = 2.3$ set and exponential distribution	94
4.17 2cell RR Active ROPs coupled auxin-PIN - with the F6 $\rho = 2$ set and and $\alpha_{u,vRR} = 5$	95
4.18 auxin-PIN - with the F6 $\rho = 2$ set and $\beta_{uRR} = \beta_{vRR} = 0$	96

4.19 2cell RR Active ROPs coupled auxin-PIN - with the F6 $\rho = 2$ set and and $\beta_{uRR} = \beta_{vRR} = 0$	96
---	----

List of Tables

2.1	Table containing the three sets of parameters used in our model	13
2.2	Errors computed with normalized $L^\infty(\Omega)$ norm of the difference between equilibrium of the system and the converged solution at $t = 200s$	27
2.3	Results of estimated order of convergence with respect to time refinement.	30
3.1	Table summarizing RR results on 2 cells system	74
3.2	Table summarizing RR results on 4 cells system	75
4.1	Table with the four sets of parameters used in auxin-PIN model, taken from [15].	78
4.2	Table summarizing auxin-PIN and RR results on two cells system	98

Acknowledgements

I would like to express my gratitude firstly to my advisor Simona Perotto and co-advisors Daniele Avitabile and Nicola Ferro, for their help and constant support through this thesis. All their advices and interests assist me to work on this new topic.

I would then also want to thank my family, in particular my parents Simonetta and Pierangelo, for all the sacrifices they made to give me the opportunity to start this adventure at Politecnico and for the safe port they have been and still are. I thank my grandfather Giuseppe, for sharing with me his passion in hard working and in searching interests in what I do.

I want to thank all friends met this years in Milan, this experience wouldn't have been the same without you. I want to thank in particular my roommates, for your patient with me, your advices and sharing. I finally want to thank Federico, for staying with me as I am and for growing next to me all these years.